8-2018

Hydrologic Evaluation of Surface and Subsurface Water in Highly Managed Watershed with Limited Observations

Aws Abdulqader Ajaaj
Clemson University, aajaaj@g.clemson.edu

Hydrologic Evaluation of Surface and Subsurface Water in Highly Managed Watershed with Limited Observations

---

A Dissertation
Presented to
the Graduate School of
Clemson University

In Partial Fulfillment
of the Requirements for the Degree
Doctor of Philosophy
Civil Engineering

---

by
Aws Abdulqader Ajaaj
August 2018

Accepted by:
Dr. Ashok. K. Mishra, Committee Chair
Dr. Abdul A. Khan, Committee Co-Chair
Dr. N. Ravichandran
Dr. Charles Privette, III

Abstract

The risk associated with managing water resources (flood or drought) depends on the adequate operation of infrastructure facilities (e.g., dams) with in the river basins. However, one of the major challenges to develop and operate infrastructures to meet stakeholder's goal is to generate accurate hydrologic information (e.g., streamflow) for ungagged (limited data/data scarce) river basins. This process usually requires spatiotemporal hydroclimatic information, such as precipitations, streamflow, and groundwater storage. Hydrological models are useful tools for investigating hydrological processes in data scarce river basins with limited hydrological measurements. The overall objective of this dissertation is to develop a modeling framework to improve surface and groundwater resources management in data scarce river basins, located in different parts of the world.

This dissertation examines the improvements of the estimations, simulation, and evaluation of various spatiotemporal hydroclimate data for a river basin located in a semi-arid climate zone and poorly represented by actual observations. First, a modeling framework is developed and applied to investigate multiple bias removal techniques to improve the use of available gridded precipitation products in poorly gauged river basins; secondly, the study is extended to investigate hydrologic processes and to simulate streamflow for ungagged river basins using different precipitation data sources; and finally an integrated surface and groundwater modeling framework

was developed to evaluate potential surface and groundwater resources in Tigris and Euphrates River Basin.

Dedication

This work is dedicated for my beloved mother and father, Sadiyah Muhammad and Abdulqader Ajaaj, for their kindness, endless love, and support which will be a continues source of inspiration to me.

Acknowledgments

I would like to deeply thank my advisors, Dr. Ashok. K. Mishra and Dr. Abdul A. Khan, who have always given me support and motivation during the years of their mentorship for me as a PhD student. It was a privilege to work under their supervision and I will never forget this learning experience during all this time.

I would also like to thank Dr. N. Ravichandran and Dr. Charles Privette, III for accepting to serve in my committee. I am thankful for them their support, guidance, and providing valuable insights which helped improving my Dissertation.

I would like to acknowledge of my parents, brothers, and sisters for the continues encouragement during hardships. I would like to thank my wife, Hind A. Ali, and my children who have giving me support, love, and ease during this journey of pursuing my dream in getting the PhD degree. Especially, my wife was the one who took care of me and our children during my busy days. I could not accomplish this without her being beside me.

I also want to extent my appreciation for all of my dear friends; especially Anoop, Goutham, and Ali for their help in clearing out many issues about the data and giving suggestions that made the research better. Finally, I am grateful to the staff members of Glenn Department of Civil Engineering for the welcoming atmosphere and the extended help with any type of administrative service they provided.

Table of Contents

List of Tables

List of Figures

Chapter 1

Introduction

1.1 Overview

Urban areas have traditionally developed near rivers and flood plains where the water management is directly linked to community development. With that, risks associated with floods and droughts have become critical and need to be considered for public policy and infrastructure planning. One such example is the water management issues in the Mesopotamia, the largest river system in the Middle East, which has been of a long struggle between the riparian countries, Turkey, Iran, Iraq, and Syria (Jaradat, 2002). Aggressive water management policies have been implemented by countries located in the upstreams to meet the increasing irrigation and population water demands (Altinbilek 2004; Bozkurt and Sen, 2013). The effect of water stress is further compounded by the declining mean annual streamflow. For example, flow observed at Kut station, southern part of the river basin, was reduced by about 50 m^3s^{-1} from 1931-1973 to 1974-2004, given similarity in mean annual precipitation in these two periods (473.34 mm and 472.80 mm, respectively) (Ajaaj et al., 2017). Thus, it can be suggested that the areas located in the downstream of the watershed

are vulnerable to extreme drought under such management plans (Wilson, 2012; Issa et al. 2015).

Given that more people in the southern areas of Mesopotamia (approximately 75%) rely on the ground water, the region has witnessed a loss of large parts of their water storage due to the extensive pumping of the groundwater from the aquifer systems with the lack of precipitation (drier arid areas; Ajaaj et al., 2017). Under such conditions, several studies raised the concerns of severe negative consequences on health, environment, and the ecosystem due to change in water quality and quantity in the freshwater with in the river basin (Altinbilek D., 2004; Al-Ansari and Knutsson, 2011). Currently,there have been severed challenges in the river basin. For instance, low surface flow and groundwater depletion and reduction in water storage and quality (Issa et al. 2015; Wilson, 2012; Venn et al. 2013; Voss et al., 2013); degradation of agricultural lands (Jabbar and Zhou, 2012) and drying of wetlands and marshlands (Jones et al., 2008) southern parts of TERB; alteration of waterways due to low flow caused by rivers damming (Nilsson et al., 2005); and increasing salinization in agricultural lands (Wu et al., 2012).

1.2 Limitations with Observed Hydroclimate Data

The assessment of regional water resource availability for any river basin is quantified by the spatial distributions of hydrologic fluxes, such as rainfall, streamflow, and groundwater variations (Kundzewicz et al. 2007). One major challenge for improving water resources management is lack of long term hydroclimatic information. This is evident due to a marked decline in hydroclimatic gauging stations in many parts of the world during past decades (Song et al. 2014; Rodda 1995a, b; Mishra and Coulibaly 2009). Due to the lack of long term hydroclimatic information,

water resources managers find it difficult to generate historical (i.e., beyond 50 years) water availability and drought information in many parts of Africa, Latin America, and Asia (WMO 1996; Mishra and Coulibaly 2009).

Another factor that affects water management is human activities and changing land cover in urban areas which play an important role in altering local to regional climate. Currently, more than 50% of the global population lives in cities, and it is projected to be 70% by 2050 (UNFPA 2007). The expansion of global urban area was about 60,000 km2 during 19702000 (Seto et al. 2011) and it is projected to increase by 1.7 million km^2 in the less-developed countries during 2000 to 2050 (Angel et al. 2011). Development of urban areas significantly alters the natural land cover. Consequently, it has been suggested that human activities in cities lead to a distinct urban climate (e.g., urban heat island) in comparison to the less built-up areas. These changes are primarily attributed to three drivers including land cover change, greenhouse gas, and aerosols (Niyogi et al. 2009; Rosenzweig et al. 2011; Liuet al. 2014). The climate change can bring additional stresses to the urban environment leading to heat waves, extreme urban flood, and health problems for vulnerable urban populations (Rosenzweig et al. 2011).

1.3 Applications of Remote Sensed Precipitation in Hydrological Modeling

With the advancements in satellite rainfall products, it is now possible to apply/evaluate these products to investigate hydrological processes in poorly gauged basins. Hydrological models are useful tools for evaluating the water resources in watersheds with limited hydrological measurements (Amisigo et al, 2008; Hongxia et

al, 2009; Abbaspour et al, 2015). The precipitation data is considered as one of the most important driving forces for hydrologic models (Beven, 2011; Miao et al., 2015). Moreover, the long-term rainfall data are important for developing metrics (i.e., risk, uncertainty and vulnerability) to evaluate climate change impact assessment by comparing past extreme events.

Several remote sensing (satellite-based) precipitation products have been recently evaluated (validated) against in-situ precipitation for streamflow simulation using hydrological models (Behrangi et al., 2011; Ali et al., 2017). The ongoing efforts for improving remotely sensed measurements have produced many high-resolution (<4 km) and temporal (<3 hours) precipitation products (Sorooshian et al., 2000). Recently there are several studies evaluated the performance of satellite-based precipitation products to predict streamflow in data sparse regions using hydrological models. For example, Thiemig et al., (2013) and Zhu et al., (2016) evaluated the use of satellite precipitation data in the hydrological applications and reported that two satellite-based precipitation products named TRMM and PERSIANN-CDR performed better in comparison to the reanalysis gauged-based data. Many studies have concluded that satellite-based precipitation products could be potentially used for hydrological predictions particularly for ungauged basins (Xue et al., 2013; Jiang et al., 2012).

However, the uncertainty associated with hydrological models, especially when using different model inputs greatly affects the model performance. This may lead to less meaningful and sometimes misleading predictions if such uncertainties are not addressed in the calibration process (Vrugt and Bouten, 2002; Schuol and Abbaspour, 2006; Yang et al., 2007 a, and b). In model calibration, instead of relying on a single model prediction, statistical methods are used to represent uncertainties in hydrological models, where such uncertainties are given a probabilistic range to account for

several sources of errors in the model (Franz et al. 2010).

1.4 Overall Research objectives

The overarching goal of this thesis is to improve water resources assessments in poorly gauged river basins around the world. To demonstrate our proposed methods, we selected Tigris River basin as a case study. Although several studies have evaluated water resource in different parts of the world (Mishra and Coulibaly, 2010; Taesombat and Sriwongsitanon, 2009; Jones et al., 2008), the studies on investigating the combined role of climatic variables, anthropogenic control (e.g., land use change) in an integrated surface and ground water modeling framework is limited. A detailed literature review is available for each research objectives proposed in this thesis. The overall four research objectives are proposed in this thesis:

First objective-Trends in precipitation and air temperature:- To investigates the trends in annual and seasonal monthly precipitation and temperature of mega cities around the globe by applying multiple trend analysis methods. This objective evaluates trends in long-term climatologies by incorporating land use change in urban verses peri-urban areas for mega cities located in various climate zones.

Objective 1.1: To investigate annual and seasonal trends in precipitation and air temperature for urban/peri-urban areas of mega cities.

Objective 1.2: To quantify the decadal change in air temperature and precipitation as well as their possible relationship.

Second objective-Precipitation bias correction:- A modeling framework is proposed and applied to investigate multiple Bias Correction Techniques (BCT's)

to improve the use of available gridded precipitation products in poorly gauged river basins.

Objective 2.1: To test multiple BCT's on monthly precipitation data to select the best method that fits each gauge station in semi-arid climate.

Third objective-Hydrologic evaluation of precipitation data sources:- The study is extended to investigate hydrologic processes and to simulate streamflow for Tigris River Basin, un-gagged river basin, from different precipitation data sources.

Objective 3.1: To evaluate the spatiotemporal heterogeneities of multiple precipitation data sources against actual gauged data.

Objective 3.2: To evaluate the suitability of using precipitation data sources to simulate streamflow in Tigris River Basin given limited hydroclimate information.

Objective 3.2: To investigate the predictive uncertainty in simulating streamflow using three calibration approaches to improve streamflow simulation.

Fourth objective-Surface and groundwater resources assessment:- River basins in semi-arid climates are likely to be vulnerable to extreme water stress conditions under projected climate change scenarios (Huetal.2016; Sun et al. 2014; Di Luca et al. 2015). Therefore, we developed an integrated surface and groundwater modeling framework to investigate water resources in Tigris and Euphrates River Basin.

Objective 4.1: To apply the fully coupled SWAT-MODFLOW model to quantify regional spatiotemporal surface and groundwater interactions in

the river basin.

Objective 4.2: To test model outputs against streamflow, groundwater levels, and total water storage anomalies derived from satellite data (GRACE) especially with the lack of actual observations.

Objective 4.3: To predict the discharges that exchange between streams and groundwater in aquifers. Also, to estimate the spatial and temporal variations of infiltration and evaporation losses from different surfaces in the watershed.

1.5 Thesis Organization

This thesis contains six chapters with the main body of research presented in **Chapter 2** to **Chapter 5**. The following research points are presented into four journal papers with two already published papers (Ajaaj et al., 2016; Ajaaj et al., 2017).

Chapter 2 presents a conservative approach in detecting trends of long term precipitation and temperature (>100years) using different trend analysis approaches. This chapter also investigates the effect of land use on the trends by considering the largest urban vs peri-urban areas in the world. This paper is published in journal of Theoretical and Applied Climatology.

Chapter 3 evaluates and compares different bias correction techniques (BCT's) using gridded precipitation data with respect to rain gauges in semi-arid climatic zone. This work is published in **Stochastic Environmental Research and Risk Assessment**.

In **Chapter 4** the hydrologic evaluation framework for assessing multiple satellite precipitation data over the Tigris River Basin is introduced and the resulted

streamflow were evaluated using stochastic model approach. Additionally, the predictive uncertainty in simulating streamflow using three calibration approaches was compared to improve streamflow simulation. This Manuscript is completed and was submitted to the **Journal of Hydrologic Engineering**.

For **Chapter 5**, the hydrologic model built in **Chapter 4** was extended in area and included not only the surface water component but also the groundwater modeled using three dimensional groundwater fully coupled model. In this chapter, the calibrated mode was utilized to understand the role of surface and groundwater interactions in the Euphrates and Tigris River Basin was investigated. This Manuscript is completed and will be send to a journal.

The section, table and figure numbers have been changed in this dissertation but all contents were kept without change. Copies of **Chapter 2** and **Chapter 3**, papers, are provided in the Appendices A and B.

Finally conclusions, recommendation, and suggested future work are listed in **Chapter 6**.

Chapter 2

Urban and peri-urban precipitation and air temperature trends in mega cities of the world using multiple trend analysis methods

2.1 Abstract

Urbanization plays an important role in altering local to regional climate.In this study, the trends in precipitation and the air temperature were investigated for urban and peri-urban areas of 18 mega cities selected from six continents (representing a wide range of climatic patterns). Multiple statistical tests were used to examine long-term trends in annual and seasonal precipitation and air temperature for the selected cites.The urban and peri-urban are as were classified based on the percentage of land imperviousness. Through this study, it was evident that removal of the lag-k serial correlation caused a reduction of approximately 20 to 30% in significant

trend observability for temperature and precipitation data. This observation suggests that appropriate trend analysis methodology for climate studies is necessary. Additionally, about70% of the urban areas showed higher positive air temperature trends, compared with peri-urban areas. There were not clear trend signatures (i.e., mix of increase or decrease) when comparing urban vs peri-urban precipitation in each selected city. Overall, cities located in dry areas, for example, in Africa, southern parts of North America, and Eastern Asia, showed a decrease in annual and seasonal precipitation, while wetter conditions were favorable for cities located in wet regions such as, southeastern South America, eastern North America, and northern Europe. A positive relationship was observed between decadal trends of annual/seasonal air temperature and precipitation for all urban and peri-urban areas, with a higher rate being observed for urban areas.

2.2 Introduction

More than 50%of the global population lives in cities, and it is projected to be 70% by 2050 (UNFPA 2007). The expansion of global urban area was about 60,000 km^2 during 1970-2000 (Seto et al., 2011) and it is projected to increase by 1.7 million km2 in the less-developed countries during 2000 to 2050 (Angel et al., 2011). Development of urban areas significantly alters the natural land cover. Consequently, it has been suggested that human activities in cities lead to a distinct urban climate (e.g., urban heat island) in comparison to the less built up areas. These changes are primarily attributed to three drivers including land cover change, greenhouse gas, and aerosols (Niyogi et al., 2009; Rosenzweig et al., 2011; Liu et al., 2014). The climate change can bring additional stresses to the urban environment leading to heat waves, extreme urban flood, and health problems for vulnerable urban populations (Rosen-

zweig et al., 2011).

Several studies indicated the possible influence of global warming on intensification of precipitation near urban centers (Diem and Mote, 2005; Kug and Ahn, 2013; Sun et al., 2014; Shahid et al., 2016; Han et al., 2015). A positive correlation between precipitation and urbanization has been confirmed using different climate models (Changnon and Westcott, 2002; Argüeso et al., 2016). Such response in urban rainfall patterns were mainly attributed to Urban Heat Island (UHI; (Dixon and Mote, 2003; Bentley et al., 2010). However, there are few studies that did not agree with this hypothesis. For example, (Tayanc and Toros, 1997; Shepherd, 2006) and (Kusaka et al., 2014) found that air temperature in mega cities has no effect on urban rainfall, while (Kaufmann et al., 2007) showed a decreasing precipitation trends over urban zones. A consensus whether the urbanization results in an increase in precipitation are yet to be confirmed (Rosenzweig et al., 2011). It is often a challenge to quantify the possible impact of UHI on urban rainfall, which is further compounded by lack of accurate observed data in the vicinity of urban areas.

Climatological trends in air temperature and precipitation have been extensively analyzed for different regions around the world (Keggenhoff et al., 2014; Pingale et al., 2014; Sharma et al., 2016). For example, investigated the possible urban effect on precipitation over western Maritime by examining two scenarios (before and after construction of urban areas). Several studies analyzed short-term trends in sub-daily air temperature and precipitation over multi-urban areas based on the direction of predominant storms (Shepherd et al., 2002; Kharol et al., 2013; Velpuri and Senay, 2013). (Alexander et al., 2006) investigated long-term (1901 to 2003) global daily air temperature and precipitation over the Northern Hemisphere mid-latitudes (and part of Australia) and observed a significant warming and wetting trends during the second half of the twentieth century (1951-2003).

Precipitation in urban area is highly influenced by many factors such as, hydroscopic nuclei, turbulence via surface roughness, and convergent wind flow which may lead to rain producing clouds (Burian and Shepherd, 2005). The land use change (urbanization/imperviousness) can possibly influence the urban climate due to the changes in surface albedo, surface roughness, and thermal and hydrological features (Hu and Jia, 2010). Therefore, evaluation of climatological trends in urban areas is important to plan, manage, and take actions regarding water related issues, such as water supply, avoiding over or under designing of water resource systems, and assessing the urban floods and droughts. Moreover, air temperature and precipitation trends in both urban and peri-urban areas should be examined to determine possible changes in local climatology.

2.3 Objectives

In this study, we used a long-term (>100-year period) gridded mean monthly air temperature and precipitation data to investigate: (a) annual and seasonal precipitation (air temperature) trends in 18 mega cities using multiple trend analysis methods. We have selected top three mega cities from each continent and each city was further classified into urban and peri-urban areas according to their percentage of land cover imperviousness; and (b) the decadal change in air temperature and precipitation as well as their possible relationship.

2.4 Study area

Three densely populated urban areas (>5 million people in population) from each of the six continents; namely, Asia (AS), North America (NA), Africa (AF),

South America (SA), Europe (EU), and Australia (AU) were selected based on the population data provided by Environmental Systems Research Institute (ESRI). The geographic and climate information for the selected cities are provided in Table 2.1. These cities witness a wide range of climatic patterns, such as, tropical monsoon, humid continental, Mediterranean, high-land climate, humid sub-tropical, humid continental, oceanic climate, and semi-arid type.

The urban/peri-urban area is classified based on the percentage of the land imperviousness, (Lu and Weng, 2006). Based on this criterion, areas with imperviousness greater than or equal to 20% are identified as urban areas (Ganeshan et al., 2013). For each urban area, the corresponding peri-urban area was delineated using a band width of 80.5 km (50 miles) from urban boundaries. The delineation between urban and peri-urban areas was accomplished manually using the Geographic Information System (GIS) maps. The band width of the peri-urban area was selected to include at least one precipitation and air temperature grid point within the selected polygon. Selected urban and their corresponding peri-urban areas are shown in Figure 2.1. The percentages of imperviousness (land use) for the selected cities are shown in Figure 2.2, where the percentages refer to the land imperviousness.

2.5 Data

Long-term Terrestrial Air Temperature (TAT) monthly data available for the period 1900-2008 was used in this study. TAT data is compiled from actual station data gathered from several updated sources (e.g., Global Historical Climatology Network GHCN2) with support from the Institute of Global Environmental Strategies (IGES).

The Global Precipitation Climatological Center (GPCC), full data reanalysis

version 7) precipitation data (Schneider et al., 2014), are used to compare the precipitation trends in urban (peri-urban) areas. One of the main reasons for selecting GPCC data was the availability of long-term data sets for 110-year period (1901-2010). The GPCC data is derived from rain gauge information (over 85,000 stations worldwide) acquired from multiple sources and updated continuously to generate reanalysis product. GPCC compared well with observed data, for example, (Funk et al., 2015) reported that interpolated data from GPCC reanalysis version 6 precipitation product performed well when compared with station data in Africa even though the lack of actual station data.

Both TAT and GPCC data were reviewed for missing data. Grid points with one or more year of missing data were removed from the analysis. The missing data for shorter duration was estimated by taking the mean of the four surrounding grid points. The newly developed 1 km resolution Global Land Cover-SHARE (GLC-SHARE) shape file created by Food and Agriculture Organization (FAO) (Latham et al., 2014) was used to distinguish grids located within urban and peri-urban boundaries.

2.6 Methodology

This section describes four different methods used to for trend analysis for air temperature and precipitation over selected cities.

2.6.1 Linear least square fit (LR)

The linear least square fit is given by Eq.(2.1) and Eq.(2.2). Where t is sample number (t=1, 2, ...,n; n being the length of the sample), $Z(t)$ is the variable being considered (such as air temperature or precipitation), and indicate average values

Table 2.1: Geographic information and climate type for the selected cities.

Content	City	Country	Area mi2	Latitude	Longitude	Climate Type
Asia	Tokyo	Japan	791	35.5	139.75	Humid subtropical
	Delhi	India	127	28.75	77.25	Monsoon
	Beijing	China	1002	40	116.25	Monsoon
North America	New York	USA	1209	41.25	-73.5	Humid continental
	Los Angeles	USA	996	34.25	-118.25	Mediterranean
	Mexico City	Mexico	171	19.5	-99	Tropical
Africa	Lagos	Nigeria	516	7	3.25	Tropical
	Johannesburg	South Africa	598	-26.25	27.5	High-land climate
	Cairo	Egypt	493	30	31	Mediterranean
South America	Sao Paulo	Brazil	3305	-23.5	-46.5	Humid sub-tropical
	Buenos Aires	Argentina	377	-34.75	-58.5	Humid sub-tropical
	Santiago	Chile	1151	-33.25	-70.25	Mediterranean
Europe	Moscow	Russia	3278	56	37.5	Humid continental
	Berlin	Germany	6053	52.5	13	Oceanic climate
	Madrid	Spain	1674	40	-3.75	Mediterranean
Australia	Sydney	Australia	503	-34	150.25	Mediterranean
	Alice Spring	Australia	1063	-23.5	133.75	Semi-arid
	Perth	Australia	408	-32	116.5	Mediterranean

(Haan, 2002).

$$b = \frac{\sum_{i=1}^{n}(t-\bar{t})(Z(t)-\bar{Z})}{\sum_{t=1}^{n}(t-\bar{t})^2} \tag{2.1}$$

$$a = \bar{Z} - b\bar{t} \tag{2.2}$$

2.6.2 Mann-Kendall test (MK1)

The Mann−Kendall (MK) nonparametric test was first proposed by (Mann, 1945) and then (Kendall, 1975). The MannKendall test statistic S is given by Eq.(2.3) and variance of S is given by Eq.(2.5). The standardized normal test statistics is computed using Eq.(2.6);

$$S = \sum_{k=1}^{n-1}\sum_{j=k+1}^{n} sign(x_j - x_k) \tag{2.3}$$

$$sign(x_j - x_k) = \begin{cases} 1, & \text{for } sign(x_j - x_k) > 0 \\ 0, & \text{for } sign(x_j - x_k) = 0 \\ -1, & \text{for } sign(x_j - x_k) < 0 \end{cases} \tag{2.4}$$

$$V(S) = \frac{n(n-1)(2n+5)}{18} \tag{2.5}$$

$$Z = \begin{cases} \frac{S-1}{\sqrt{V(S)}}, & \text{if } S > 0 \\ 0, & \text{if } S = 0 \\ \frac{S+1}{\sqrt{V(S)}}, & \text{if } S < 0 \end{cases} \tag{2.6}$$

A positive (negative) value of Z indicates upward (downward) trend in the time series being tested (Luo et al., 2008); (Drápela et al., 2011). The advantage of MK1 is that it is distribution free test and insensitive to the outliers. However, the MK1 test requires the data to be serially uncorrelated or in other words the time series data should be independent (Yue et al., 2002); (Kumar et al., 2009). The MK test is widely used for trend analysis in hydro-climatic variables (Mishra et al., 2011); (Mishra and Singh, 2010).

2.6.3 Mann-Kendall test with trend-free pre-whitening (MK2)

The trend free pre-whiting process (TFPW) was proposed by (Yue et al., 2002) as a way to remove the serial correlation from the data before applying MK1 test. De-trending the time series is a necessary step to remove the effect of a significant linear trend on the serial correlation. It is demonstrated in Eq.(2.7), where X'_t is the de-trended data, X_t is the original data, slope (b) is calculated using the Theil-Sen

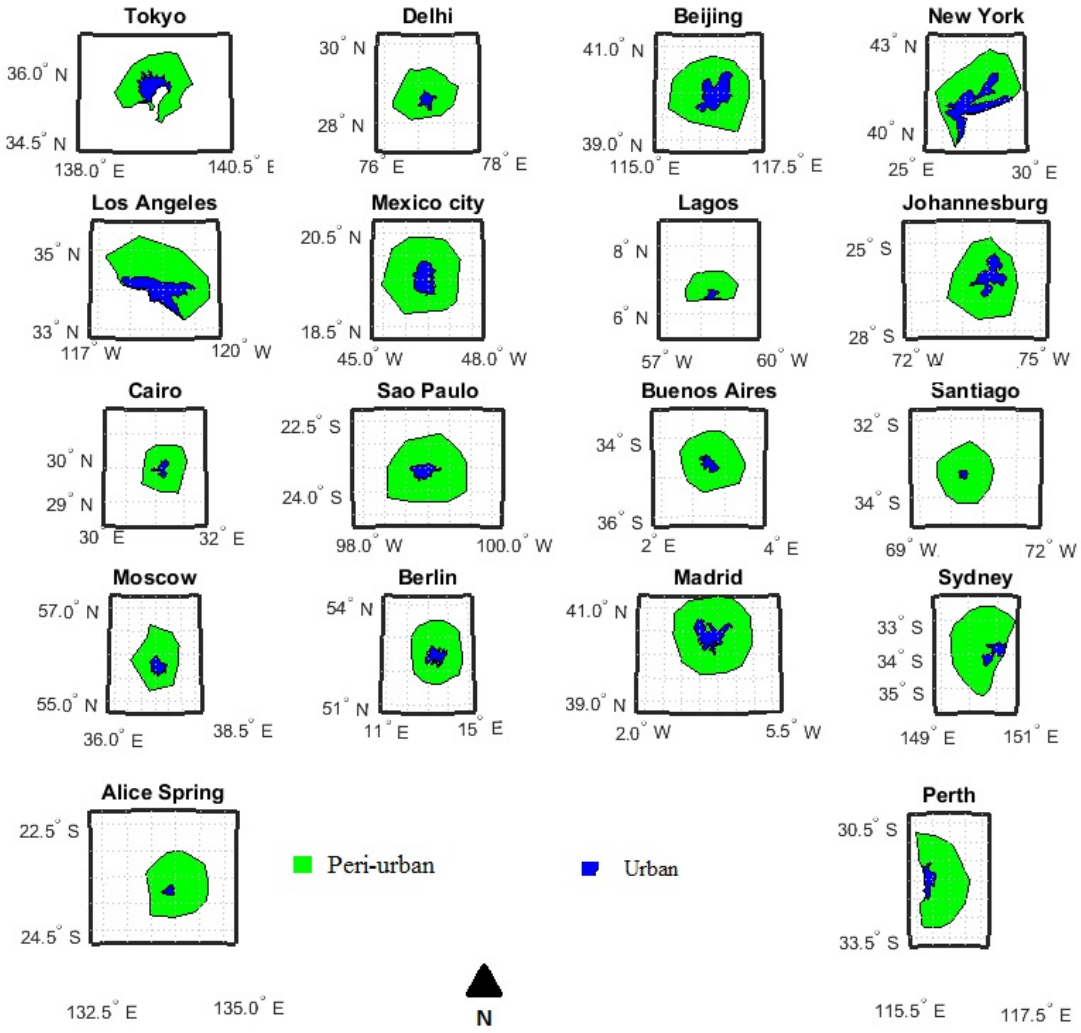

Figure 2.1: Location of selected mega cities and their urban and peri-urban boundaries. The blue polygon represents the urban area selected based on the surface imperviousness. The green polygons represent the peri-urban areas.

Approach (TSA), and t is the time.

$$X'_t = X_t - bt \tag{2.7}$$

Then lag-1 serial correlation can be removed from de-trended time series by using Eq.(2.8). Where Y'_t a trend-free and pre-whitened time series, and r_1 is the lag-1 serial correlation for the de-trended time series. The residuals are added to the time series data to get the blended time series as in Eq.(2.9), which is less influenced by serial correlation. Finally, the MK1 test is applied on the final data set as described in Section 2.6.2.

$$Y'_t = X'_t - r_1 Y'_{t-1} \tag{2.8}$$

$$Y_t = Y'_t + bt \tag{2.9}$$

2.6.4 Mann-Kendall test with variance correction (MK3)

To overcome the limitation of the presence of serial autocorrelation in time series, a correction procedure was proposed by (Hamed and Rao, 1998). First, the corrected variance S is calculated by Eq.(2.10), where $V(S)$ is the variance of the MK1 and CF is the correction factor due to existence of serial correlation in the data. This correction factor was suggested by (Hamed and Rao, 1998) and (Yue et al., 2002) and given by Eq.(2.11), where r_k^R is lag-ranked serial correlation, while n is the total number of observations.

$$V^*(S) = CF \times V(S) \tag{2.10}$$

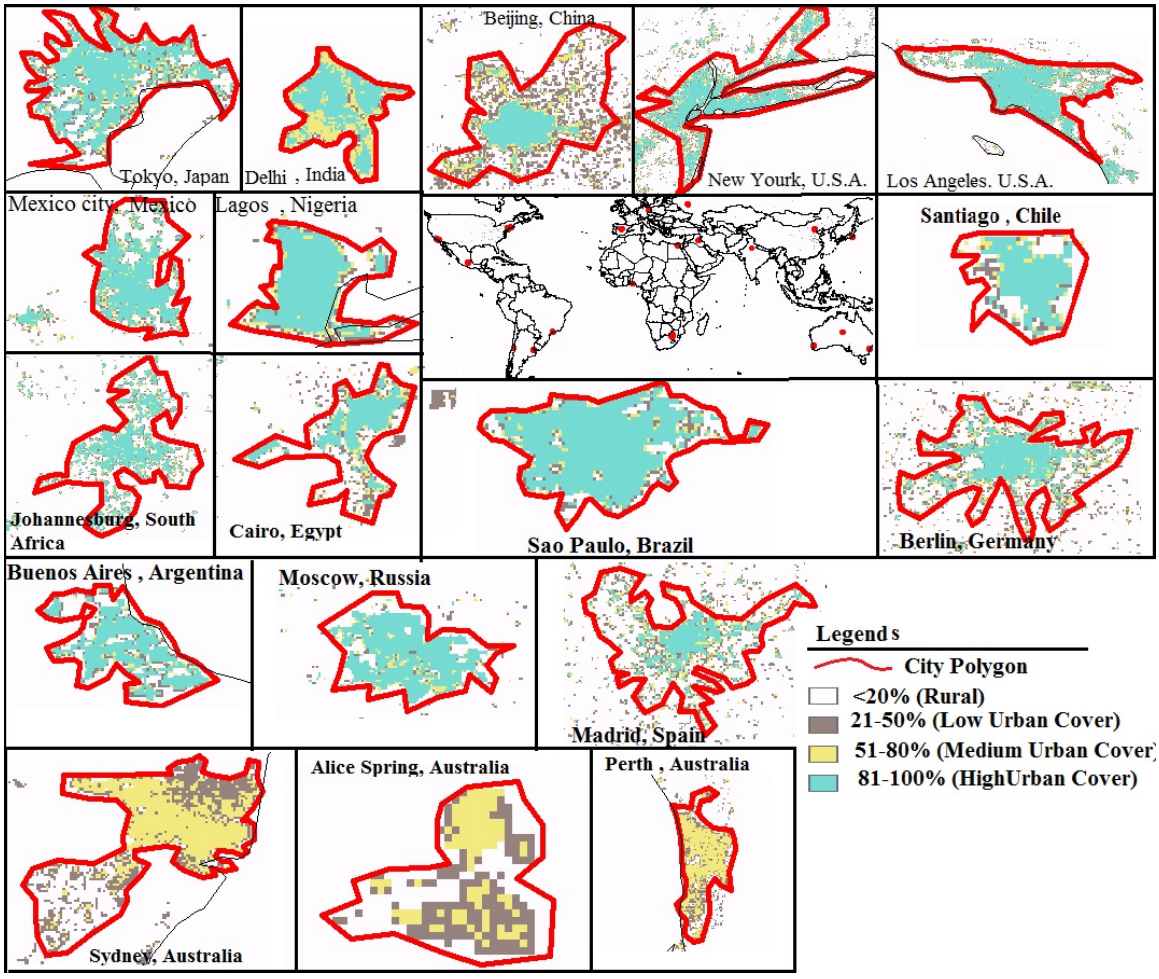

Figure 2.2: Percentage of imperviousness for the selected urban areas.

$$CF = 1 + \frac{2}{n(n-1)(n-2)} \sum_{k=1}^{n-1} (n-k)(n-k-1)(n-k-2) r_k^R \qquad (2.11)$$

The advantage of MK3 test over MK2 test is that it includes all possible serial correlations (lag-k) in the time series, while Mk2 only considers the lag-1 serial correlation (Yue et al., 2002).

2.7 Results

The selected cities are located in a wide range of climatic zones; therefore, they witness different rainfall, air temperature, and wet (dry) seasons. For example, Johannesburg winter months are counted from May to September, while in Delhi from November to January. For this reason, the year was divided into two distinct groups as wet and dry spells (or seasons). For each city, wet spell includes the months in which the total rainfall exceeds the average annual rainfall. The dry spell includes the months with total rainfall less than the average annual rainfall.The average monthly precipitation pat- tern for each city is presented in Figure 2.3, which clearly shows the variation of wet and dry seasons for different cities analyzed in this study. The mean of annual, dry and wet season precipitation was calculated from the GPCC monthly data for the period 1901 to 2010.

Table 2.2: Percentage of urban/peri-urban areas registered significant trend (at 5% significance level) using MK1, MK2, and MK3 tests.

Method	Urban			Peri -urban			Urban			Peri -urban		
	ANNT[a]	WETT	DRYT	ANNT	WETT	DRYT	ANNP[a]	WETP	DRYP	ANNP	WETP	DRYP
MK1	88.9	66.7	88.9	83.3	66.7	77.8	33.3	38.9	22.2	38.9	33.3	16.7
MK2	83.3	66.7	88.9	77.8	66.7	77.8	33.3	38.9	22.2	38.9	33.3	16.7
MK3	55.6	50	50	55.6	44.4	38.9	16.7	22.2	11.1	16.7	16.7	0

[a] The terms ANNT and ANNP shown in this table and later tables are the annual air temperature and precipitation,WETT and WETP represent wet season air temperature and precipitation, and DRYT and DRYP are dry season air temperature and precipitation.

2.7.1 Comparison between Mann-Kendall tests

The trend analysis was carried out using different Mann-Kendall tests (i.e., MK1, MK2, and MK3). In order to overcome the limitations due the presence of serial correlation in annual and seasonal mean air temperature and precipitation,

MK2 and MK3 methods were applied in trend analysis. MK2 eliminates the lag-1 auto correlation by using free pre-whitening (FPW), while MK3 removes the lag-k serial correlation by variance correction (VC) method. The percentage of significant trends for air temperature and precipitation based on MK1, MK2, and MK3 test are provided in Table 2.2. When using MK1 and MK2 tests, similar number of cities have significant trend in precipitation which indicates the removal of lag-1 auto-correlation that may not have much influence on the trend analysis. This pattern is also similar for air temperature during wet and dry seasons. However, MK1 test comparatively has higher number of stations for air temperature at annual scale. As reported in Table 2.2, the number of urban areas showing significant trend decreased when auto correlation correction was applied. The lower percentage of significant trends for both air temperature and precipitation was observed in case of MK3 test in comparison to MK1 and MK2 tests. Overall, the result obtained from MK3 test is more conservative in comparison to other two tests, therefore it is important to evaluate multiple MK test in trend analysis of hydro-climatic variables.

2.7.2 Trends in air temperature

The annual, wet, and dry season mean air temperature were analyzed using MK1, MK2, and MK3 tests for the period 1901-2008 to determine whether each city is experiencing cooling or warming trends (Table 2.3).The MK1, MK2, and MK3 test results were investigated for possible influence of presence of serial-1 and serial-k correlations on significant trend results for air temperature in urban and peri-urban areas. Many of the previous studies only focused on classical MK1 test for trend analysis in hydro-climatic time series, which ignores the presence of correlation in time series (Karabulut et al., 2008); (Karmeshu, 2012). However, we observed that MK3

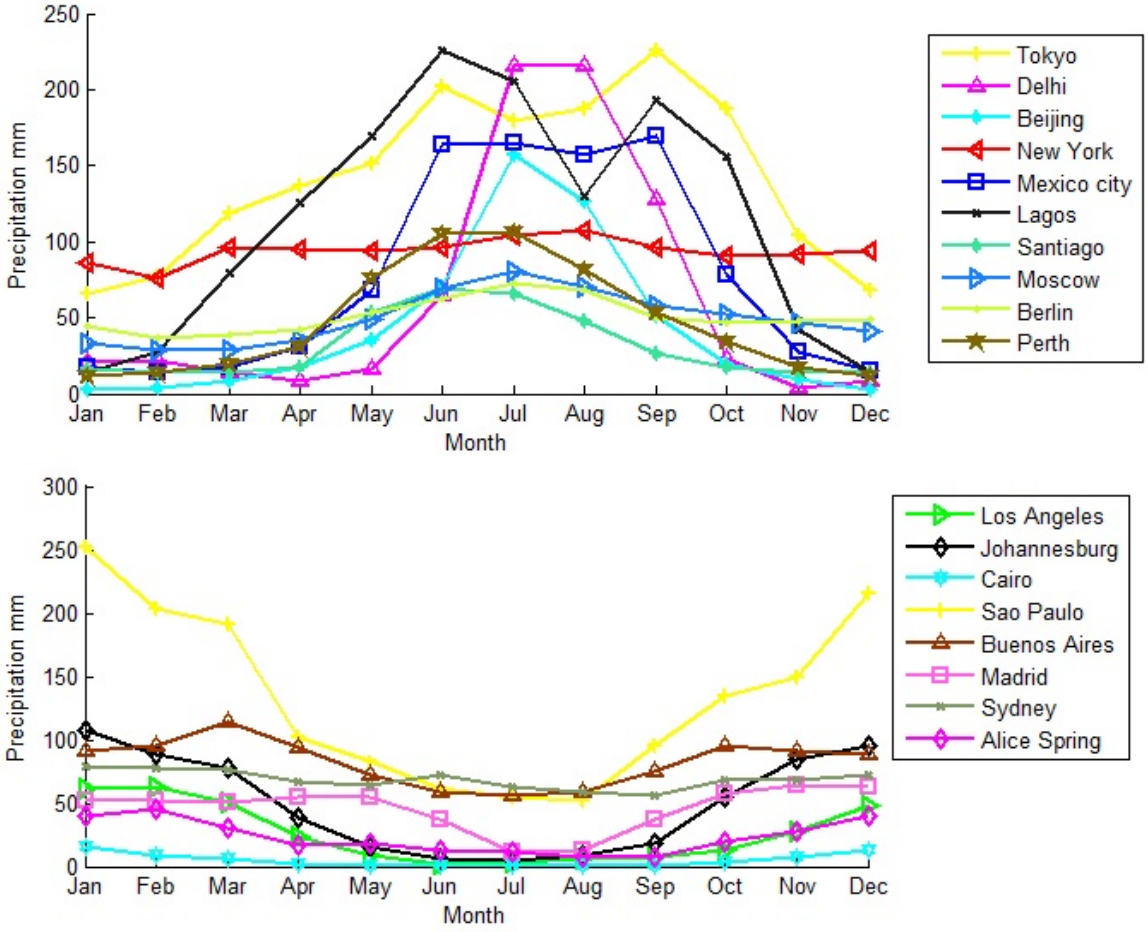

Figure 2.3: Variations of mean monthly precipitation for the selected cities calculated from GPCC data for the period 1901-2010.

results provide a conservative estimate after removing all forms of serial correlations.

Overall, there is an increasing trend for urban and peri-urban annual and seasonal air temperature. Based on the MK3 results (Table 2.3), it was observed that 70% of the urban areas experienced warmer trend (i.e., $Z > 0$) in annual and seasonal air temperature in comparison to the peri-urban areas. Significant warming trends are found in about 56% of urban areas (likewise for peri-urban areas) based on annual air temperature. None of the urban and peri-urban areas register a significant cooling trend based on annual and seasonal air temperature. However, the urban air temperature in wet and dry seasons illustrates higher significant trends (i.e., $Z > 1.96$) than peri-urban areas. About 50% of urban areas show significant warming trends, whereas for peri-urban areas, these values are lower than those in the urban areas with about 44 and 39% during wet and dry seasons, respectively. Significant warming trends in annual air temperature are observed in Tokyo and selected cities in North America, Johannesburg, Sao Paulo and Buenos Aires, and Moscow and Madrid. Urban areas located in Australia do not show any significant trend for annual air temperature; these urban areas show the lowest imperviousness among all selected urban areas, Figure 2.2.

We applied linear regression method to estimate the magnitude of change in air temperature with respect to time. The change in annual and seasonal air temperature over a 10-year period for urban and peri-urban areas is shown in Figure 2.4. The rectangular box plot shows three horizontal lines that represent the median (intermediate line), 25^{th} percentile (lower line), and 75^{th} percentile values (upper line), while the two top and bottom vertical lines represent the maximum and minimum changes over the 10-year period for the urban and peri-urban areas. The results show that the median rise in urban annual and seasonal air temperature is higher than that in the peri-urban areas, which is consistent with the results revealed by MK3 test.

Table 2.3: Trend analysis of air temperature using MK1/MK2/MK3 tests for urban and corresponding peri-urban areas. Significant trends tested at 95% confidence level (i.e. $|Z| > 1.96$), are shown as bold letters.

City	**Urban**			**Peri -urban**		
	ANNT	**WETT**	**DRYT**	**ANNT**	**WETT**	**DRYT**
Tokyo	**7.77/7.71/2.29**	**5.65/5.55/2.33**	**7.47/7.53/2.13**	**6.16/6.1/2.23**	**4.63/4.58/2.33**	**5.7/5.67/2.02**
Delhi	-0.59/-0.48/-0.67	-1.3/-1.09/-1.35	0.39/0.3/0.48	-0.33/-0.01/-0.4	-0.92/-0.68/-1	0.67/0.58/0.91
Beijing	**4.31/5.97**/1.77	**2.2/3.2/1.24**	**5.45/5.98/2.02**	**3.88/5.41**/1.67	1.82/**2.76**/1.05	**5.11/5.42/2.01**
New York	**4.32/4.16/2.22**	**3.48/3.57/2.14**	**3.48/3.24/2.12**	**2.6/2.33**/1.95	1.58/1.63/1.79	**2.38/2.05**/1.97
Los Angeles	**6.29/6.7/2.02**	**6.6/6.77/2.06**	**4.25/4.31**/1.84	**5.63/6.01/2.04**	**5.86/5.87/2.11**	**3.08/3.35**/1.72
Mexico City	**7.04/8.09/2.04**	**5.89/6.4**/1.92	**7.39/7.95/2.11**	**6.68/7.66/2.13**	**6.06/6.4/2.06**	**6.37/7.2/2.12**
Lagos	-0.11/0.46/-0.06	0.33/0.96/0.19	-0.54/0.05/-0.25	-0.1/0.26/-0.06	0.17/0.41/0.12	-0.5/0.03/-0.29
Johannesburg	**5.63/6.05/2.2**	**4.64/4.93/2.11**	**5.36/5.37/2.13**	**4.87/4.95/2.13**	**3.23/3.24**/1.87	**5.08/5.11/2.07**
Cairo	**2.59/3.27**/1.56	**3.08/3.57**/1.68	1.73/**2.02**/1.4	**2.06/2.62**/1.22	**2.93/3.67**/1.53	0.52/0.75/0.4
Sao Paulo	**9.17/9.1/2.28**	**8.91/8.8/2.26**	**7.86/7.76/2.24**	**8.66/8.53/2.24**	**8.38/8.28/2.22**	**7.14/6.99/2.2**
Buenos Aires	**9.19/9.25/2.25**	**7.12/7.05/2.17**	**7.61/7.95/2.15**	**8.06/7.96/2.23**	**6.16/6.05/2.2**	**6.35/6.85/2.08**
Santiago	**4.2/4.71**/1.77	**5.99/6.61**/1.97	1.49/1.89/1.34	**5.06/5.39/2.05**	**6.49/6.88/2.15**	**2.47/2.81**/1.81
Moscow	**5.66/5.78/2.19**	**5.09/5.32/2.22**	**4.23/4.22/1.99**	**4.49/4.57/2.19**	**4.19/4.33/2.22**	**3.08/3.09**/1.91
Berlin	**3.14/3.27**/1.86	**3.36/3.58/2.08**	1.62/1.59/1.34	**2.84/3.02**/1.82	**3.25/3.41/2.11**	1.49/1.41/1.3
Madrid	**5.75/5.58/2.27**	**3.48/3.65**/1.96	**5.28/4.99/2.04**	**5.67/5.9/2.12**	**4.16/4.41**/1.91	**4.74/4.7/2**
Sydney	**2.02**/1.74/1.87	0.51/0.53/0.81	**3.19/3.05/2.13**	-0.34/-0.27/-0.59	-1.39/-1.24/-1.72	0.96/0.52/1.45
Alice Spring	**3.86/4.38**/1.98	**4.29/4.62/2.07**	**2.54/2.43**/1.88	**4.09/4.62/2.05**	**4.49/4.65/2.12**	**2.73/2.54**/1.95
Perth	**3.01/2.86**/1.67	**2.62/2.54**/1.64	**2.71/2.56**/1.66	**2.05/1.96**/1.52	**2.07/2.08**/1.7	1.44/1.35/1.15

The magnitudes of decadal slopes for urban and peri-urban areas are presented in Table 2.4. Linear trend results indicate that about an average of 20% of urban areas experienced higher mean decadal increase in annual and seasonal air temperature in comparison to peri-urban areas. During the period 1901-2008, the average increase in air temperature for all 18 urban areas observed to be 1, 0.8, and 1.1 ^{o}C for annual, wet season, and dry season, respectively. Similarly, upward trends are also observed in peri-urban areas albeit with lower rates of warming. The average increase in 18 peri-urban areas observed to be remarkably less with 0.8, 0.6, and 0.9^{o}C for annual, wet, and dry air temperature respectively for the time period 1901-2008. For the same time period, Sao Paulo (Delhi) recorded the highest (lowest) change among all urban and peri-urban areas for annual data with 2 (-0.1)^{o}C.

Figure 2.5 shows the linear regression and the 5-year moving average trend for the annual air temperature. It can be observed that warming signature based on urban areas is located in the Mediterranean climate except Cairo, and Monsoon climate is comparatively higher than the corresponding sub-urban areas. Furthermore, the annual air temperature for peri-urban areas of Sao Paulo and Buenos Aires (both located in humid sub-tropical climate), and Johannesburg (located in high-land climate) show higher values than corresponding urban pairs. However, the rates of warming for these urban areas are relatively higher than those for the peri-urban sites Table 2.4. It can be suggested that regardless of the urban heat effect over urban areas, there is a general persistent growth of warming with time over almost all urban and peri-urban areas. For the period (1901-2008), significant warming trends were observed in mean annual and seasonal air temperature over the majority of urban and peri-urban pairs. The level of significance was found to be higher over urban areas in comparison to corresponding peri-urban areas, which indicates the clear influence of urbanization on air temperature.

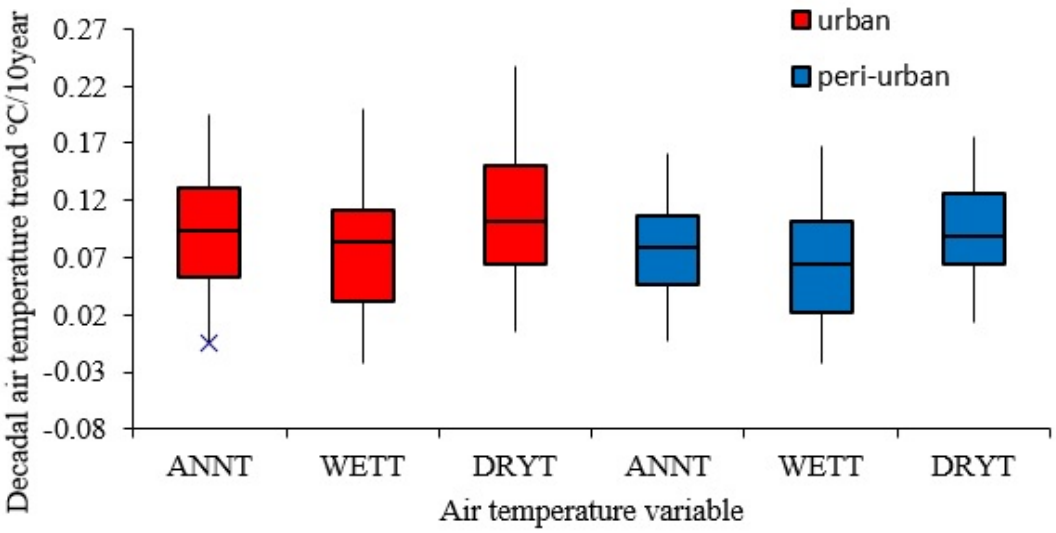

Figure 2.4: Box plot of mean slopes based on decadal change in air temperature during the period 1901-2008. [Steps used: (a) for a selected city, the time series is divided into decades, (b) the slopes associated for each decade are calculated, (c) the mean of decadal slope is calculated for each city, and (d) the box plot is constructed based on the mean of decadal slope calculated for the 18 selected cities]

2.7.3 Trends in precipitation

Trend analysis was performed for annual and seasonal (i.e., wet and dry) precipitation during the period 19012010 using MK1, MK2, and MK3 tests Table 2.5. Overall, annual and seasonal precipitation for urban and peri-urban areas shows mix (increasing and decreasing) trends unlike air temperature data. For annual precipitation, it was found that half of urban and peri-urban areas witness increasing trend while the other half a decreasing trend based on MK3 test. Trends in precipitation data were determined at a statistical significant level of 5% (similar to air temperature analysis). A significant increase in mean annual precipitation was found in two urban and peri-urban areas while one location shows a significant decreasing trend. Significant increasing precipitation trends for annual rainfall are mainly observed in the cities of Buenos Aires and Berlin, while a significant decreasing trend was found for Cairo. Trend results of seasonal precipitation for both urban/peri-urban areas exhibit similar pattern as in annual precipitation, Table 2.5. For the wet season, only two cities (Sao Paulo and Buenos Aires) appeared to have significant increasing trends, while peri-urban areas located in Buenos Aires witness a significant increasing trend. Both Perth and Cairo found to have a significant decreasing precipitation trend during wet season. For dry season, none of the urban/peri-urban areas have a positive significant trend. However, the urban areas of Cairo and Madrid show significant decreasing trend in dry season. It is worth to mention that the number of cities witnessing significant increasing (decreasing) trend is higher in MK1 and MK2 test in comparison to MK3 test, Table 2.5.

The box plot for the decadal change in precipitation was estimated using linear regression for annual and seasonal precipitation during the time period 1901-2010, Figure 2.6. The interquartile range (IQR) for decadal trends in annual and wet

Table 2.4: Decadal slope obtained from linear regression for air temperature during the period 1901-2008.

City	Urban ^{o}C/10-year			Peri-urban ^{o}C/10-year		
	ANNT	WETT	DRYT	ANNT	WETT	DRYT
Tokyo	0.14	0.11	0.16	0.1	0.08	0.11
Delhi	-0.01	-0.03	0	0	-0.03	0.01
Beijing	0.09	0.03	0.12	0.08	0.02	0.11
New York	0.09	0.08	0.11	0.06	0.04	0.08
Los Angeles	0.12	0.09	0.14	0.1	0.07	0.12
Mexico city	0.13	0.11	0.15	0.11	0.09	0.12
Lagos	0.01	0.00	0.01	0.00	0.00	0.01
Johannesburg	0.09	0.08	0.1	0.07	0.05	0.09
Cairo	0.04	0.03	0.05	0.04	0.01	0.06
Sao Paulo	0.19	0.19	0.19	0.16	0.16	0.15
Buenos Aires	0.16	0.15	0.17	0.13	0.12	0.14
Santiago	0.06	0.02	0.08	0.07	0.04	0.08
Moscow	0.19	0.13	0.23	0.15	0.11	0.17
Berlin	0.08	0.08	0.08	0.07	0.07	0.07
Madrid	0.1	0.1	0.1	0.1	0.1	0.11
Sydney	0.02	0.00	0.04	-0.01	-0.02	0.01
Alice Spring	0.09	0.11	0.07	0.09	0.1	0.08
Perth	0.04	0.04	0.05	0.03	0.02	0.04

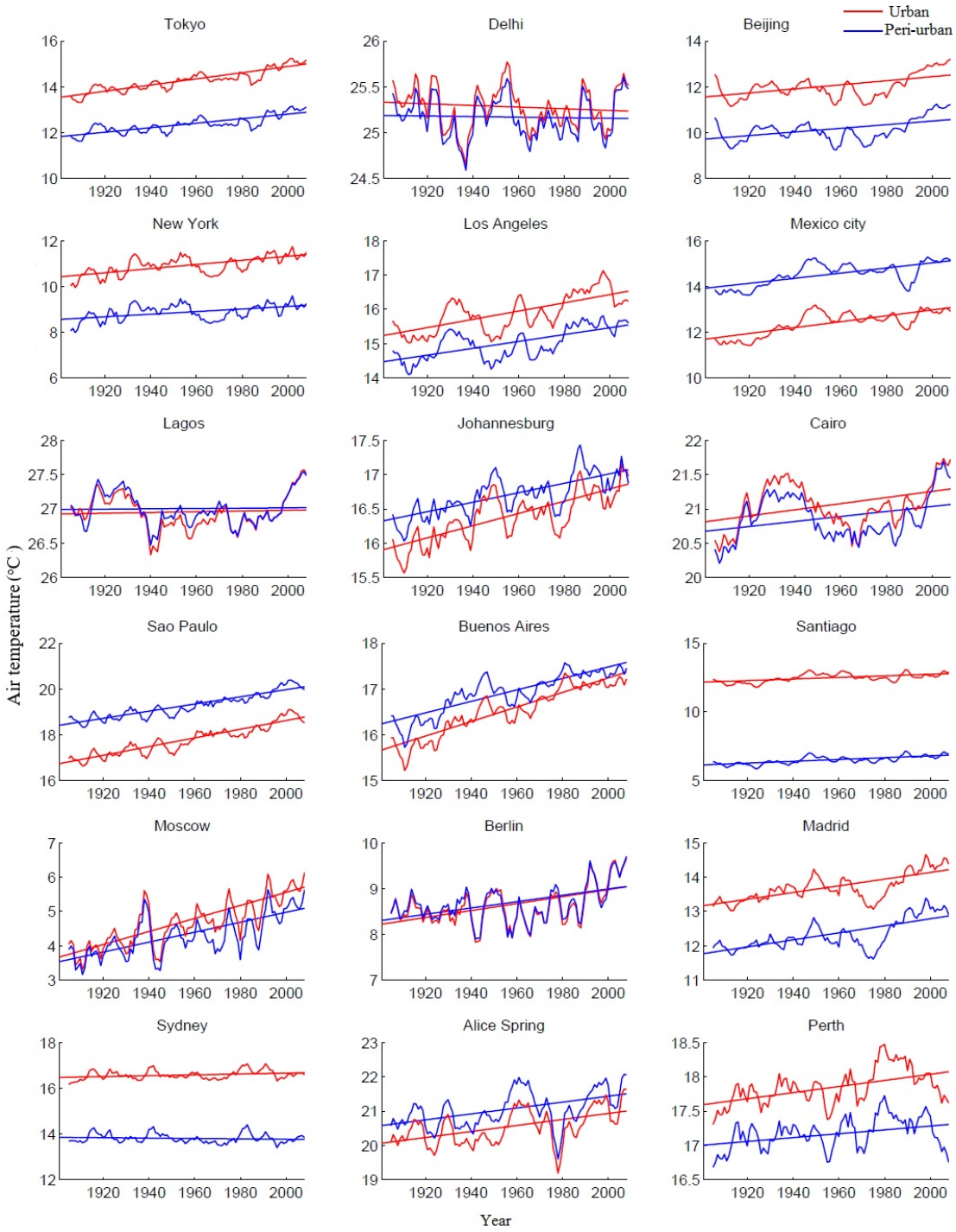

Figure 2.5: Linear trends based on 5-year moving average of annual air temperature for urban and peri-urban areas

Table 2.5: Trend analysis of precipitation using MK1/MK2/MK3 tests for urban and corresponding peri-urban areas. Significant trends are considered at 95% confidence level (i.e. $|Z|$), are shown as bold letters.

City	Urban ANNP	WETP	DRYP	Peri-urban ANNP	WETP	DRYP
Tokyo	-1.81/-1.91/-1.45	-1.49/-1.61/-1.34	-1.41/-1.36/-1.74	**-1.97/-2.07/-1.69**	-1.72/-1.87/-1.59	-1.44/-1.38/-1.71
Delhi	1.18/1/1.53	0.79/0.6/1.14	0.88/0.99/0.93	1.12/1/1.52	0.78/0.54/1.16	0.95/0.97/0.99
Beijing	-0.76/-0.57/-0.9	-1.22/-1.23/-1.15	1.98/1.97/1.77	-0.23/-0.09/-0.34	-0.92/-0.73/-0.95	2.17/2.35/1.8
New York	0.89/1.08/1.12	0.87/1.17/1.13	0.44/0.42/0.91	2.14/2.32/1.76	1.69/1.88/1.66	1.47/1.63/1.79
Los Angeles	-0.92/-0.98/-1.38	-0.83/-0.88/-1.33	-1.09/-0.91/-1.2	-1.33/-1.37/-1.51	-1.12/-1.21/-1.44	-1.62/-1.48/-1.49
Mexico city	**3.3/3.25**/1.83	3.96/4.15/1.89	0.2/-0.15/0.28	1.39/1.28/0.88	**2.43/2.37**/1.35	-0.68/-0.97/-0.75
Lagos	-1.61/-1.29/-1.61	-0.9/-0.73/-1.23	**-2.65/-2.55/-1.54**	0.08/0.31/0.13	1.04/1.26/1.23	**-3.15/-3.16/-1.67**
Johannesburg	-1.14/-1.01/-1.8	-1.1/-1.08/-1.55	-0.36/-0.22/-0.38	-0.51/-0.41/-0.98	-0.6/-0.49/-1.32	-0.11/0.1/-0.12
Cairo	**-3.74/-3.34/-2.09**	**-2.38/-2.25/-2.03**	**-2.11/-1.1/-2.04**	**-4.34/-4.35/-2.13**	**-3.29/-3.31/-2.14**	-1.63/-0.79/-1.61
Sao Paulo	**2.45/2.49**/1.74	2.91/2.71/1.98	0.46/0.44/0.7	1.98/1.99/1.63	2.46/2.33/1.83	0.4/0.48/0.62
Buenos Aires	**4.64/4.51/2.08**	**4.81/4.74**/1.96	0.87/0.87/0.93	**4.13/3.97/2.08**	**4.44/4.36/2.04**	0.46/0.38/0.51
Santiago	-0.94/-0.87/-1.24	-1.09/-1/-1.5	0.6/0.46/0.84	-0.37/-0.37/-0.52	-0.98/-0.83/-1.19	1.87/1.67/1.87
Moscow	4.31/4.37/1.94	2.52/2.23/1.9	4.2/4.24/1.82	4.15/4.06/1.86	2.41/2.04/1.85	4.13/4.19/1.78
Berlin	1.16/1.05/2.01	0.08/-0.06/0.17	1.27/1.3/1.59	0.95/0.89/1.98	-0.23/-0.37/-0.39	1.3/1.4/1.77
Madrid	-0.58/-0.59/-0.86	0.04/0.08/0.07	-1.86/-1.97/-2.01	-0.36/-0.32/-0.52	0.2/0.13/0.36	-1.48/-1.43/-1.8
Sydney	1.14/1/1.14	2.3/2.05/1.5	-1.1/-1.05/-1.6	1.2/1.12/1.07	1.71/1.6/1.43	-0.47/-0.51/-0.69
Alice Spring	0.75/0.75/0.95	0.36/0.47/0.6	0.15/0.01/0.25	-0.17/-0.07/-0.28	-0.33/-0.16/-0.55	-0.4/-0.54/-0.97
Perth	**-2.36/-2.54/-1.9**	**-3.33/-3.37/-2.03**	0.85/0.72/1.55	**-1.96/-2.22/-1.86**	**-2.99/-3.13/-1.97**	1.4/1.13/1.9

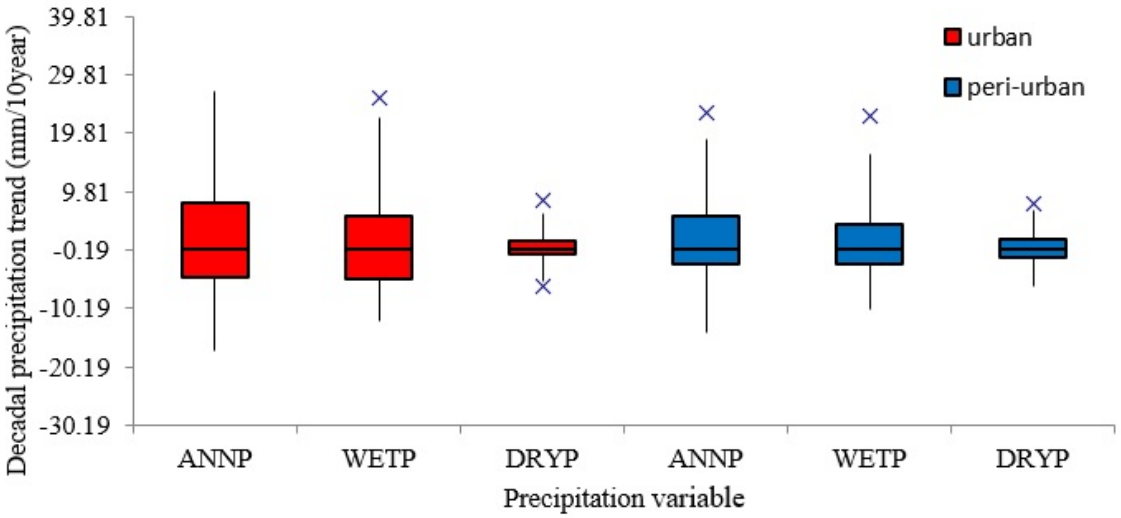

Figure 2.6: Box plot of mean slopes based on decadal change in precipitation. [Steps used: similar to Figure 2.4].

season precipitation for selected urban areas are comparatively higher than the peri-urban areas. This effect becomes less obvious in case of dry season. The median of decadal precipitation trends in urban areas during 1901-2010 is slightly higher than the peri-urban areas by the amount of 3.6, 1.6, and 0.5 mm/10 years for the annual, wet and dry season, respectively. An increase in mean annual and seasonal precipitation was also observed in urban averages over the surrounding peri-urban areas. The relative increase in average precipitation in urban areas with respect to peri-urban areas observed to be 41, 29.3, and 11.87 mm for annual, wet, and dry seasons, respectively, Table 2.6.

The maximum linear decadal increase for urban (and the corresponding peri-urban area) was observed for Buenos Aires with 27.87 (23.27) mm/10 years during annual precipitation, and 25.77 (22.72) mm/10 years for wet season precipitation. The lowest decadal trend in annual precipitation of urban (peri-urban) area was observed in Cairo with a value of -1.75 (-2.41) mm/10 years. The 5-year moving averages for

Table 2.6: Decadal slope for precipitation based on linear regression line during the period 1901-2010.

City	Urban mm /10-year			Peri-urban mm /10-year		
	ANNP	WETP	DRYP	ANNP	WETP	DRYP
Tokyo	-14.35	-11.02	-3.33	-14.3	-10.26	-4.05
Delhi	7.41	5.21	2.21	6.24	4.27	1.97
Beijing	-4.14	-6.34	2.2	-0.7	-2.78	2.08
New York	4.72	2.56	2.16	9.23	4.41	4.82
Los Angeles	-3.02	-2.09	-0.92	-5.4	-4.06	-1.34
Mexico City	10.96	11.55	-0.59	5.24	7.19	-1.95
Lagos	-17.48	-11	-6.48	-4.32	1.93	-6.24
Johannesburg	-5.72	-5.02	-0.71	-2.66	-2.34	-0.32
Cairo	-1.75	-1.11	-0.63	-2.41	-1.82	-0.59
Sao Paulo	17.81	14.77	3.04	14.52	11.61	2.91
Buenos Aires	27.87	25.77	2.1	23.27	22.72	0.55
Santiago	-4.99	-5.2	0.21	-1.23	-3.29	2.06
Moscow	14.69	6.43	8.26	13.22	5.57	7.65
Berlin	3.41	0.51	2.89	2.44	-0.02	2.46
Madrid	-1.59	0.48	-2.07	-0.69	0.82	-1.51
Sydney	9.16	13.52	-4.36	5.85	7.17	-1.32
Alice Spring	5.59	3.75	1.84	1.71	1.36	0.35
Perth	-11.29	-12.44	1.15	-5.94	-7.33	1.39

the mean annual precipitation time series are given in Figure 2.7. A general trend in annual precipitation for the urban/ peri-urban areas cannot be ascertained as both increasing and decreasing trends were observed in multiple cities. Interestingly, the significant increasing trends for both annual precipitation and air temperature were observed in urban areas of Sao Paulo and Buenos Aires (both located in humid sub-tropical climate), and Johannesburg (located in high-land climate). This obvious variation of urban precipitation signal in these locations Figure 2.5 is an option for future research direction and it deserves special attention.

The spatial distribution of trends based on MK3 statistics for annual and seasonal precipitation data for urban and surrounding peri-urban areas was analyzed and presented in Figures 2.8, 2.9, and 2.10. It was interesting to observe difference between annual precipitation trends for some urban and peri urban areas, for example

in Beijing and Lagos, where the negative trends are observed for urban whereas positive trends were observed in the vicinity of the urban polygons Figure 2.8. During the wet spell and for most locations, the negative trends in precipitation are more predominant in most urban areas Figure 2.9. Negative trends were less prevalent during the dry spells particularly in the cities of Beijing, Tokyo, and Perth. During the dry spell, positive trends are more dominated over negative trends Figure 2.10.

2.7.4 Possible Linkage between Precipitation, Temperature, and Imperviousness

The scattered plots between decadal linear slopes of annual (seasonal) precipitation and air temperature for selected cities are shown in Figure 2.11. A positive relationship between precipitation and air temperature was observed for all selected urban and peri-urban areas. The increments in precipitation and air temperature, however, seem to be relatively higher in urban than in peri-urban areas. This finding does not necessarily mean that higher air temperature trend results in higher precipitation over all urban areas because other drivers can influence the global precipitation such as topography and large climate oscillations.

The scatter plot between the decadal trends of annual and seasonal precipitation (air temperature) in urban areas and percentage of imperviousness of urban areas is presented in Figure 2.12. As illustrated in the top panel, with the increase of surface imperviousness, the majority of urban centers experienced more warming conditions, while only Delhi and Lagos cities registered cooling trend. The bottom panel of Figure 2.12 indicates that, along with the increasing imperviousness, an equal number of the cities showed two different trends, where 50% registered an increase in annual and seasonal precipitations and the other 50% showed decreasing trends.

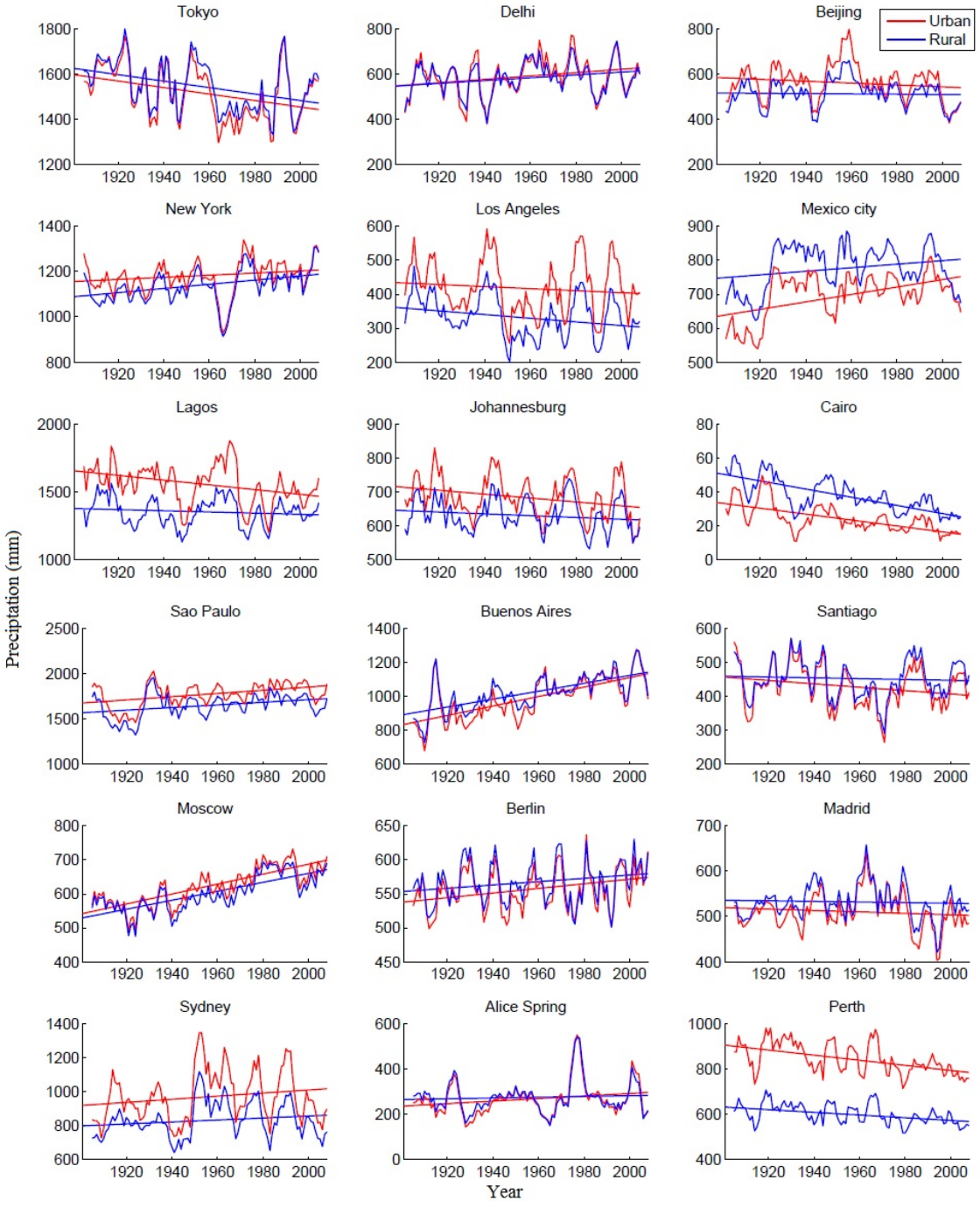

Figure 2.7: The linear trends based on 5-year moving average for annual precipitation for the period 1901-2008 for urban and peri-urban areas.

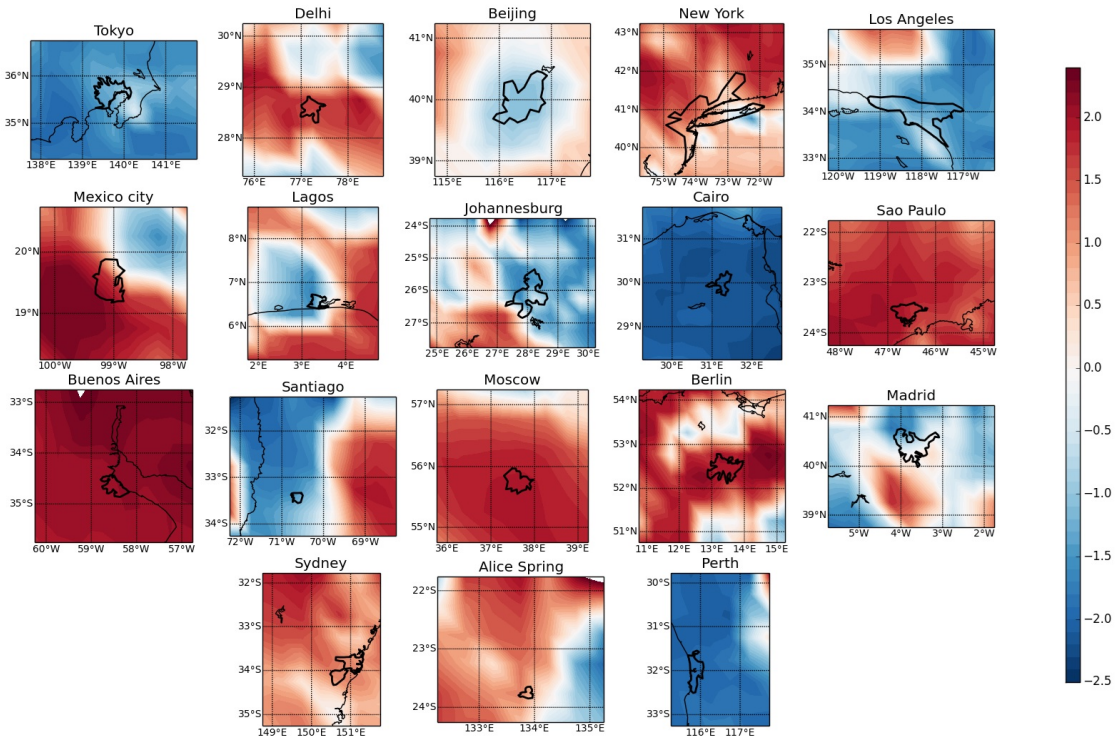

Figure 2.8: Spatial distribution of Z statistics based on MK3 test for annual precipitation (1901-2010) in urban and peri-urban areas.

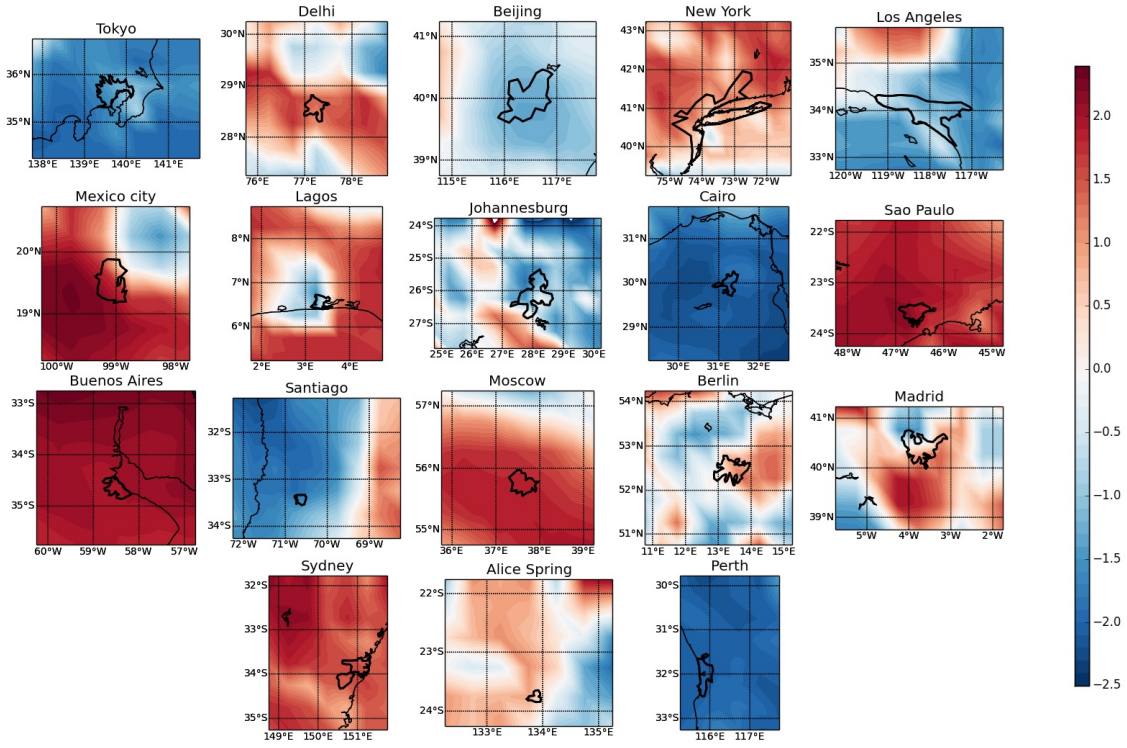

Figure 2.9: Spatial distribution of Z statistics based on MK3 test for wet season precipitation (1901-2010) in urban and peri-urban areas.

This suggests that, with land use change in urban areas, no clear signal was observed in annual and seasonal precipitation trends over the period 1901-2010.

2.8 Discussion

The trend analysis is likely to be influenced by the length of the time series (Yue et al., 2002), and to overcome this limitation, we used longer data length (>100 years) in our analysis. We found that majority of urban areas considered in the study showed warming trends at annual and seasonal time scale (urban areas is more than peri-urban areas), which makes them highly vulnerable to the effect of the climate change. This conclusion is also confirmed by several studies, i.e., (Han et al., 2015;

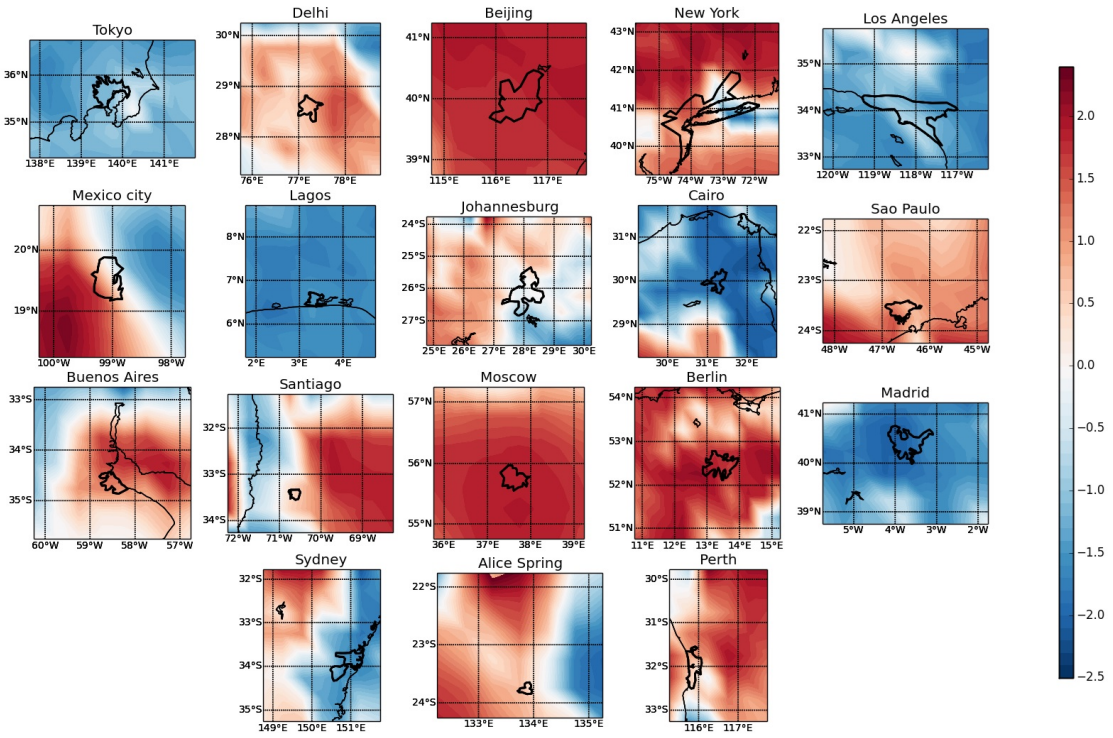

Figure 2.10: Spatial distribution of Z statistics based on MK3 test for dry season precipitation (1901-2010) in urban and peri-urban area.

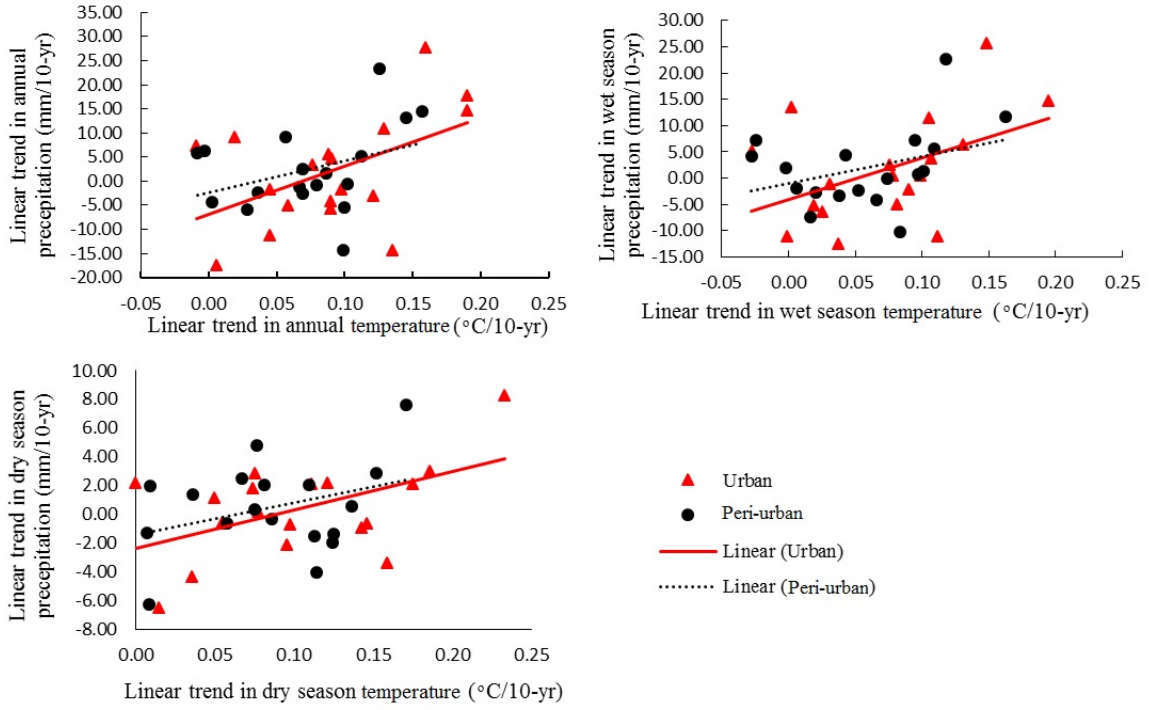

Figure 2.11: Scatter plot between mean decadal slopes based on annual air temperature and precipitation for urban and peri-urban areas.

Hu et al., 2016; Kephe et al., 2016). It was observed that cities located in dry regions such as Africa, southern parts of North America (Los Angeles), Eastern Asia (Tokyo and Beijing) witness a decrease in annual and seasonal precipitation, whereas increasing precipitation pattern was observed for cities located in wet regions such as, Southeastern South America (Buenos Aires and Sao Paulo), Eastern North America (New York), and Northern Europe (Berlin and Moscow). These results generally agree with previous findings based on observed data (Sun et al., 2014) and climate model outputs (O'Gorman and Schneider, 2009; Di Luca et al., 2015).

In our analysis, we identified that difference in land use plays an important role in temperature (precipitation) trends associated with urban (peri-urban) areas. This study can supplement previous studies where additional variables that influence the

precipitation and temperature patterns are as follows: (a) climate oscillations, such as El NioSouthern Oscillation (ENSO) by circulating energy between the tropics which leads to change in wind, temperature, and precipitation (Trenberth and Caron, 2000), (b) cloud mixing in urban areas which substantially increases near cities because uplifted moisture condenses once it reaches saturation level (Kusaka et al., 2014), and (c) Urban Heat Island (UHI), for example, (Fujibe, 2009) reported that Tokyo metropolitan has more prominent summer heat island which is caused by increasing urban land area and population. According to (Inoue and Kimura, 2007), this UHI enhances short-term intense precipitation over the city during summer while the long-term precipitation signal decreased during the wet spell. Overall, the unclear precipitation signal over urban areas creates a room for more investigations.

2.9 Summary and Conclusions

The long-term trends in mean annual, wet spell, and dry spell air temperature and precipitation was analyzed for 18 pairs of urban and peri-urban areas selected from six contents. The Global Precipitation Climatological Center (GPCC) monthly data for the period 19012010 was used along with the corresponding air temperature data derived from Terrestrial Air Temperature (TAT) during the period 19012008. Three non-parametric MannKendall and linear regression tests were adopted to identify the presence of serial correlation and to estimate the change value in the data. The following conclusions are drawn from the study:

a. The presence of serial correlation in precipitation (air temperature) time series likely to impact trend analysis, therefore application multiple trend analysis (i.e., MK1, MK2, and MK3) may be more useful in hydro-climate trend studies to arrive at a conservative result. In our study, the majority of the annual and

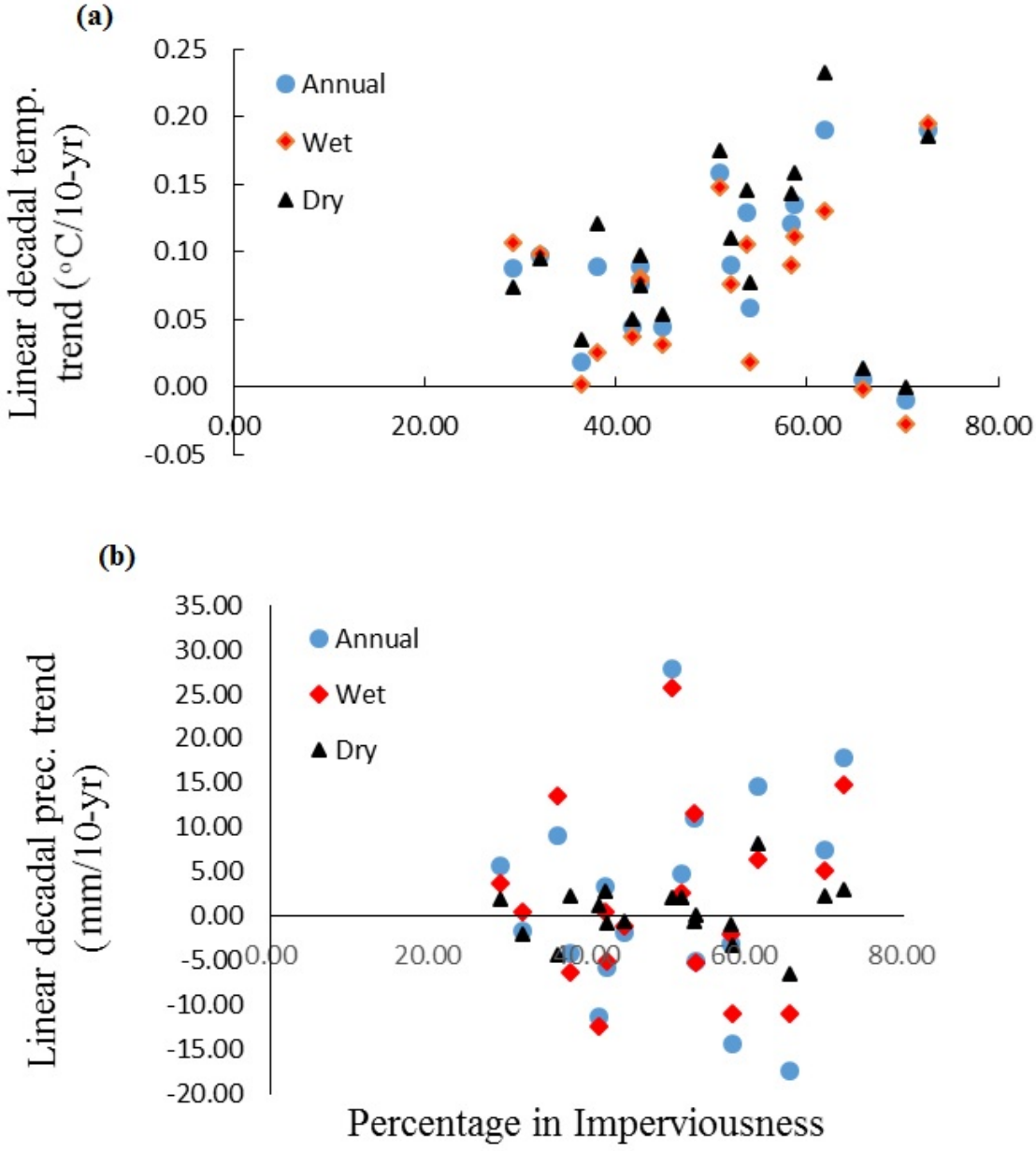

Figure 2.12: Scatter plot between: (a) mean decadal slope of annual, wet and dry seasons air temperature and the percentage of imperviousness for urban areas, (b) mean decadal slope of annual, wet and dry seasons precipitation and the percentage of imperviousness for urban areas.

seasonal air temperature and precipitation time series have significant lagged serial correlation.

b. There are relatively higher trends associated with annual and seasonal air temperature and precipitation in urban areas in comparison to peri-urban areas especially with significant trends.

c. There is a positive correlation between decadal changes of annual (seasonal) air temperature and precipitation for all urban and peri-urban areas, with urban areas witnessing slightly higher correlation than peri-urban areas. This indicates that there might be a combined influence of climate and human factors on the annual and seasonal precipitation for the selected urban areas.

d. It was observed that urbanization (i.e., percentage of imperviousness surface) brings more warming to the majority of geographic locations considered in the analysis; however, there is a mix (increasing and decreasing) pattern observed for precipitation. Additional efforts are required to investigate the influence of urbanization on hydrological variables as well as climate extremes.

Chapter 3

Comparison of BIAS correction techniques for GPCC rainfall data in semi-arid climate

3.1 Abstract

Long-term historical precipitation data are important in developing metrics for studying the impacts of past hydrologic events (e.g., droughts) on water resources management. Many geographical regions around the world often witness lack of long term historical observation and to overcome this challenge, Global Precipitation Climatology Center (GPCC) datasets are found to be useful. However, the GPCC data are available at coarser scale (0.5^o resolution), therefore bias correction techniques are often applied to generate local scale information before it can be applied for decision making activities. The objective of this study is to evaluate and compare five different bias correction techniques (BCT's) to correct the GPCC data with respect to rain gauges in Iraq, which is located in a semi-arid climatic zone. The BCT's

included in this study are: Mean Bias-remove (B) technique, Multiplicative Shift (M), Standardized-Reconstruction (S), Linear Regression (R), and Quantile Mapping (Q). It was observed that the Performance Index (PI) of BCT's differs in space (i.e., precipitation pattern) and temporal scale (i.e., seasonal and monthly). In general, the PI for the Q and B were better compared to other three (M, S and R) bias correction techniques. Comparatively, Q performs better than B during wet season. However, both these techniques performed equally well during average rainy season. This study suggests that instead of using a single bias correction technique at different climatic regimes, multiple BCT's needs to be evaluated for identifying appropriate methodology that suits local climatology.

3.2 Introduction

The long-term rainfall data are important for developing metrics (i.e., risk, uncertainty and vulnerability) to evaluate climate change impact assessment by comparing past extreme events. Freshwater is mainly driven by precipitation (Kundzewicz et al., 2007) and it is an important component for water resources planning and management purposes. One of the challenges for improving water resources management is lack of long term hydroclimatic information. This is evident due to a marked decline in hydroclimatic gauging stations in many parts of the world during past decades (Song et al., 2014; Rodda, 1995a; Rodda, 1995b; Mishra and Coulibaly, 2009). Due to the lack of long term hydroclimatic information, water resources managers struggle to generate historical (i.e., beyond 50 years) water availability and drought information in many parts of Africa, Latin America, and Asia (WMO 1996; Mishra and Coulibaly 2009).

In recent years, several efforts have taken place to develop a long term global

precipitation database (Tanarhte et al., 2012; Hijmans et al., 2005). One such example is the Global Precipitation Climate Center (GPCC) database, which was derived by World Climate Research Program (WCRP) based on a combination of radiometric observations from satellites and rain-gauges. GPCC data were widely used during recent decades (Prakash et al., 2011; Raziei et al., 2011). For example, (Nicholson et al., 2003) validated both the GPCC and the Global Precipitation Climatology Project (GPCP) datasets against the rain gauge data over North Africa. (Chokngamwong and Chiu, 2004) compared the rain gauge data from more than a hundred stations with both the GPCC and the tropical rainfall measuring mission (TRMM) data. The results showed the mean gridded monthly GPCC rainfall data was very close to observed data with mean bias of 1.4 mm/month. (Raziei et al., 2010) and (Raziei et al., 2011) observed that the GPCC data performed well in reproducing the observed precipitations over Iran which can be used to fill the missing observed data. However, the GPCC data may not represent local scale precipitation information accurately due to its coarser spatial resolution (Schneider et al., 2008; Bolvin et al., 2009). In general, the precipitation information obtained from such coarser resolution (e.g., GCMs) needs to be treated (i.e., downscaling and bias correction) before applying it to water resources planning and decision making activities (Christensen et al., 2007; Prudhomme et al., 2002; Fowler et al., 2007; Maraun et al., 2010).

Despite the increasing application of climate model out- puts in water resources and hydrologic sciences, there are often challenges due to the presence of considerable biases (Ines and Hansen, 2006; Mishra and Singh, 2009; Li et al., 2014). Common reasons for such biases are due to imperfect conceptualization, discretization and spatial averaging within grid cells (Teutschbein and Seibert, 2012). There are numerous applications of bias correction techniques to utilize coarse scale climate information at finer scale (Teutschbein and Seibert, 2012; Li et al., 2014), for example, appli-

cation to Regional Climate Model outputs (Ashfaq et al., 2010; Dosio and Paruolo, 2011; Rojas et al., 2011; Sunyer et al., 2012; Gudmundsson et al., 2012), and Global Climate Model outputs (Boé et al., 2007; Li et al., 2010; Johnson and Sharma, 2011; Acharya et al., 2013; Shao and Li, 2013; Jeong et al., 2012). These bias corrected climate model outputs are used in different sectors, such as, agriculture (Ines and Hansen, 2006; Mishra et al., 2013) and water resources (Wood et al., 2004; Maurer and Hidalgo, 2008; Mishra and Singh, 2009; Rajsekhar et al., 2015). The commonly used BCT's along with their advantages and disadvantages are provided in Table 3.1.

3.3 Objectives

Limited investigations were done to evaluate multiple bias correction techniques in different climatic regions under data scarce conditions at different temporal scales (seasonal and monthly). Therefore, for this objective, we evaluated the performance of GPCC data against the in-situ precipitation record to choose the best bias correction technique that fits each rain-gauge station. The motivation for this research is derived from: (a) Single bias correction techniques: It is a common practice to use a single bias correction technique for correcting GCM outputs. Our study indicates that multiple BCTs should be tested instead of applying a single BCT in a non-homogeneous climatic region. (b) No prior comparison: Even though a number of studies were carried out to evaluate and compare multiple bias correction techniques for GCM's (RCM's) outputs, a limited study was done for GPCC data sets. (c) Data scarce conditions: We applied our modeling framework to Iraq due to: (i) limited hydro-climatic study in the region, and (ii) lack of continuous and dense gauge based precipitation data which is very important for water resources planning purposes. Even though remote sensing products can provide finer scale information, they may

not provide long term hydro-climatic information.

Section 3.4 discusses the methodology with a focus on bias correction techniques and goodness of fit tests, whereas Section 3.5 provides an overview of study area and data used in the study are discussed in Section 3.6. Results are presented in Section 3.7 and conclusions are drawn in Section 3.8.

3.4 Methodology

Following steps were used: (a) gauge based rainfall station was first defined by its latitude and longitude and the corresponding GPCC data at these locations were estimated by interpolating from four surrounding grid points. Linear inverse distance weighting interpolation method was used to estimate GPCC rainfall from the nearest four grid points. (b) The GPCC datasets for each of these stations were then corrected using five different BCTs. The monthly data includes January through May, and October through December. They were chosen because 99% of the rainfall occurs in these months, while no correction was done for summer months (June through September) as it contributes less than 1% of the total rainfall. The seasonal data includes two seasons: the wet spell (December through March) when much of the rainfall occurred, and the average spell (April, May, October, and November) when relatively less rainfall was recorded. (c) The performance of bias corrected GPCC data was then evaluated using seven goodness of fit tests (GOF's) to identify best BCT for a given gauge location.

3.4.1 Bias correction techniques (BCT's)

Five BCT's were implemented for comparing bias corrected GPCC data with respect to gauge based rainfall data. A brief discussion on the BCT's is provided in

Table 3.1: Bias correction techniques commonly used in hydro-climatic studies.

Method	Reference	Advantage	Disadvantage
Linear correction method	Hay et al., (2000) Lafon et al., (2013)	Simplicity and modest data requirements	It may not capture inter-monthly variability and possibly affect moments of the probability distribution of daily precipitations (Diaz-Nieto and Wilby, 2005).
Nonlinear correction method	Shabalova et al. (2003); Leander and Buishand (2007)	Simplicity and it requires monthly observed statistics	Biases associated with higher order moments may not be removed by this method (Lafon et al., 2013)
Mean Bias-removal technique	Davis, (1976); Kharin and Zwiers, (2002)	Simple mean based method. The mean monthly correction factor is applied to GPCC data for the same month. Performs better when large set of data used in model training.	It does not account for cyclical nature of the climate pattern and it may not remove bias associated with higher order moments.
Multiplicative Shift technique	Ines and Hansen, (2006); Acharya et al., (2013)	It can remove the bias from mean monthly rainfall and it can be used for correcting daily GCM rainfall.	Bias exists in rainfall intensity and frequency and specifically for dry periods. It fails to correct year to year variations in rainfall total and intensities.
Standardized-Reconstruction technique	Pan and van den Dool (1998); Acharya et al., (2013)	Elimination of possible systematic error.	May not fit to skewed data very well.
Linear Regression	Davis (1976); Kharin and Zwiers, (2002); Acharya et al., (2013)	Simple mean based method	Over-fitting issue and it may not capture changes in frequency distribution.
Quantile Mapping	Ines and Hanson (2006), Piani et al. (2010), Wood et al. (2004), Maurer and Hidalgo, 2008, Teutschbein and Seibert (2012), Mishra et al., (2013)	Widely used and it can effectively remove biases in the first two statistical moments. It can capture evolution of mean and variability of a GCM while matching all statistical moments.	No adjustment is made to the temporal structure of daily precipitation. Unable to capture modeled wet and dry spell lengths. It lacks to generate interannual variability of precipitation.
Local intensity scaling	Schmidli et al. (2006); (Chen et al., 2013).	The wet-day frequency is corrected.	It does not account for the changes in the frequency distribution as well as Temporal structure of daily precipitation occurrence
Daily translation	Mpelasoka and Chiew (2009); (Chen et al., 2013).	Correction factors can be applied to correct frequency distribution	Unable to adjust temporal structure of daily precipitation

following sections.

Mean bias-remove (B): The presence of mean bias in simulated data can often increase the value of mean square error (MSE). The mean bias can be removed if both simulated and corresponding observed records are available (Kharin and Zwiers, 2002). In this technique the mean bias b_t is calculated each year by calculating the difference between observed and simulated rainfall as follows:

$$b_t = Y - F \tag{3.1}$$

Where, Y is observed climatology, and F is simulated climatology. This difference b_t is calculated using the leave one year out method. This "mean bias" is then added to uncorrected simulated data for that year to get the corrected simulated climatology i.e. $B_t = F_t + b_t$, (Acharya et al., 2013). For example, if we want to correct the year 1935, first the mean bias b_{1935} is calculated from the difference between the observed and simulated data from 1936 up to 1958. Then b_{1935} is added to simulated mean of 1935 (i.e., F_{1935}). This process is systematically repeated for each year in the data set.

Multiplicative shift (M): The simulated data was first corrected by finding the ratio between observed (Y) and simulated (F) climatologies for each year using the following expression, $m_t = \frac{Y}{F}$ (Ines and Hansen, 2006; Acharya et al., 2013). The m_t value should be calculated in the cross validation manner. It is then multiplied by the model simulated value for generating bias corrected climatology i.e., $M_t = F_t \times m_t$, where F_t is explained previously.

Standardized-reconstruction (S): Standardized-reconstruction technique was introduced by (Pan and van den Dool, 1998). One of the main problems of model

forecasts is systematic error which is the algebraic mean difference between the simulated and the observed data for each year. To eliminate this problem, standardization process is required for simulated and observed data. The standardization of simulated data ($F_t^{'}$) can be obtained from simulated climatology, and standard deviation. This can be expressed as follows (Acharya et al., 2013):

$$F_t' = F_t - \frac{F}{\sigma_F} \tag{3.2}$$

where σ_F is the standard deviation of simulated data. The simulated forecast (F), observed climatology (Y) and observed standard deviation (σ_Y) can be used along with (F_t') to reconstruct the observed data. In other words, the reconstruction can be represented as follows $S_t = F_t \times \sigma_Y + Y$. Again, all statistical variables, (F,Y, σ_F and σ_Y), should be calculated in leave one out cross validation process.

Linear regression (R): In this technique, the general linear regression equation is used, which is given by:

$$R_t = a_o + a_t \times F_t \tag{3.3}$$

Where a_0 and a_t are called the constant and coefficient of the linear regression data and R_t is the corrected simulated climatology. (Krishnamurti et al., 2000) described that the coefficients of the linear fit can be evaluated using the least

square estimates as follows.

$$a_t = \frac{Cov(Y, F)}{Var(F)} \tag{3.4}$$

$$a_o = Y - a_t \times F \tag{3.5}$$

where $Cov()$ is the covariance for the observed (Y) and the simulated (F) climatologies, respectively. $Var()$ is the variance of the simulated (F) data. Again, it should be mentioned that a_0 and a_t are calculated by the leave one out cross validate manner (Kharin and Zwiers, 2002).

Quantile mapping (Q) Quantile mapping is one of the most common statistical bias correction techniques which has been widely used to correct the biases in model forecasts, e.g. (Wood et al., 2002; Wood et al., 2004; Ines and Hansen, 2006; Piani et al., 2010a; Piani et al., 2010b; Acharya et al., 2013)). In this technique, a transformation function is directly derived from the observed (Y) and the simulated (F) climatologies. The transformation function for both rainfall datasets is fitted with a statistical continuous probability distribution function (PDF). Most of the rainfall time series in Iraq follows a gamma probability distribution function (Al-Suhili and Khanbilvardi, 2014; Alghazali and Alawadi, 2014). Quintile mapping based BCT follow two steps: (a)first calculate the cumulative distribution functions (CDF's) for both observed and simulated climatologies, and (b) use the transfer function to generate bias corrected climatology (Ines and Hansen, 2006):

$$F = CDF_F^{-1} \times (CDF_Y \times Y) \tag{3.6}$$

where CDF_F and CDF_Y are the cumulative distribution functions for both observed (Y) and simulated (F) climatologies respectively.

3.4.2 Goodness of fit tests (GOF's)

Seven statistical GOF tests are used to determine appropriate BCT for each station. The terminology used to describe GOF tests are listed here: $C()$ is the covariance of observed (Y) and simulated (F) climatologies respectively, Y_t and F_t are observed and simulated climatologies at time unit t respectively, and $\bar{Y}$ and $\bar{F}$ are the mean of observed and simulated climatologies for the entire time period respectively, and n is the total number of years in the dataset.

Correlation coefficient (R): is a measure of the degree of linear relationship between two variables. The correlation coefficient is related to the covariance as follows:

$$R(i,j) = \frac{C(Y,F)}{\sqrt{C(Y,Y)(F,F)}} \tag{3.7}$$

Correlation coefficient value varies between -1, which indicates perfect negative correlation, to 0, no correlation, to +1, perfect positive correlation (Crawford, 2006).

Coefficient of determination (R^2): describes the proportion of the variance in measured data explained by the model. R^2 values varies from 0 to 1, with values closer to 1 indicates better agreement between the data in comparison. Typically, R^2 bigger than 0.5 can be considered reasonable value for hydrological

purposes (Santhi et al., 2001; Moriasi et al., 2007). This test is given as:

$$R^2 = \left\{ \frac{\sum_{t=1}^{T}(Y_t - \bar{Y})(F_t - \bar{F})}{[(Y_t - \bar{Y})^2]^{0.5}[(F_t - \bar{F})^2]} \right\}^2 \tag{3.8}$$

Root mean square error (RMSE): is the most commonly used error statistics test (Chu and Shirmohammadi, 2004; Singh et al., 2005; Moriasi et al., 2007). The RMSE value closer to zero indicates better the performance of the model. The RMSE value is given by the following equation:

$$RMSE = \sqrt{\frac{\sum_{t=1}^{T}(Y_t - F_t)^2}{n}} \tag{3.9}$$

Standard deviation ratio (RSR): It is given by the Eq.(3.10):

$$RSR = \frac{\sqrt{\sum_{t=1}^{T}(Y_t - F_t)^2}}{\sqrt{\sum_{t=1}^{T}(Y_t - Y_t)^2}} \tag{3.10}$$

RSR always has positive value and it ranges from the lower optimal value of 0 (zero RMSE or perfect model simulation) to large positive value (poor model simulation). The closer the value of RSR is to zero, the better the simulation of the model (Moriasi et al., 2007).

Percent bias (PBIAS): gives an indication about the general tendency of the error in the simulated data (Gupta et al., 1999; Santhi et al., 2001; Moriasi et al., 2007). The closer magnitude the PBIAS is to zero, the more accurate the model simulation. Positive PBIAS values indicate model underestimated bias, however negative values indicate model overestimated bias. The result of

PBIAS is given as percentage and as follows:

$$PBIAS = \frac{\sum_{t=1}^{T}(Y_t - F_t)^2}{\sum_{t=1}^{T} Y_t} \times 100 \tag{3.11}$$

Nash-Sutcliffe efficiency (NSE): It is computed using the following equation (Nash and Sutcliffe, 1970; Moriasi et al., 2007):

$$NSE = 1 - \frac{\sum_{t=1}^{T}(Y_t - F_t)^2}{\sum_{t=1}^{T}(Y_t - \bar{Y})^2} \tag{3.12}$$

NSE values vary from ($-\infty$ to 1) and generally, the values between 0 and 1 are considered acceptable values for the model performance with an optimal value of 1, which means perfect performance for the model.

Willmott index of agreement (d): Willmott index is calculated according to the following equation (Willmott et al., 1985):

$$d = 1 - \frac{\sum_{t=1}^{T}(Y_t - F_t)^2}{\sum_{t=1}^{T}(|F_{-}\bar{Y}| + |Y_t - \bar{Y}|)^2} \tag{3.13}$$

It ranges between 0, which indicates no agreement between the observed and model datasets, to 1, which means perfect agreement. Willmott index of agreement is sensitive to extreme events due to its dependence on squared differences (Legates and McCabe, 1999); (Sexton, 2007).

Performance index (PI) For a given BCT, it is defined as the ratio between number of stations performed well based on GOF's with respect to the total number of stations within the basin, and it is given in term of percentage.

3.5 Study Area

Iraq is located in the southwest of the Asian continent and shares boundaries with each Syria and Jordan from the west, Turkey from the north, Iran from the east, and Saudi Arabia and Kuwait from the south, Figure 3.1. Iraq is comprised of an area of 437,065 km^2 (Malinowski, 2002). Iraq has a transitional climate between the Mediterranean climate and desert climate moving from the north to the south, which is generally known as arid or semi-arid climate (hot dry summers and cold winters). Most of the rainfall occurs in the winter months between December and April, and remaining months can relatively be considered average-to-dry months with the hottest months being June, July and August. Generally, the mean minimum temperatures during winter reaches very low ranging from freezing in the north and northeast regions (mountains) to 2.5^{o}C in the western part and 4.5^{o}C in the south. During summer the mean maximum temperature can range from 37.7^{o}C in the northeast (mountains) and the southwest parts (Desert) to 43.3^{o}C in the south and in some stations, it reaches up to 48^{o}C.

Iraq's elevation reduces from north and the northeast where the mountains are near the Turkish-Iranian borders (3607 m) to the west and south where the desert near Saudi Arabian-Syrian borders (few meters). We utilize these different elevations to classify Iraq into five climate zones namely northeast (mountains) (NEMZ), north (cultivated foothills and lower mountain valleys) (NVZ), south and southwestern (desert) (SDZ), central to southeastern (fertile Tigris and Euphrates alluvial plain) (CFZ), and west (WZ) (western plateau) (see Figure 3.1). It is obvious from Figure 3.1 that most of the rainfall stations are concentrated in three zones namely NEMZ, NVZ, and CFZ. At the same time, there are not many stations in the desert (SDZ) region. The reason for this is that measuring the amounts of rainfall in Iraq oc-

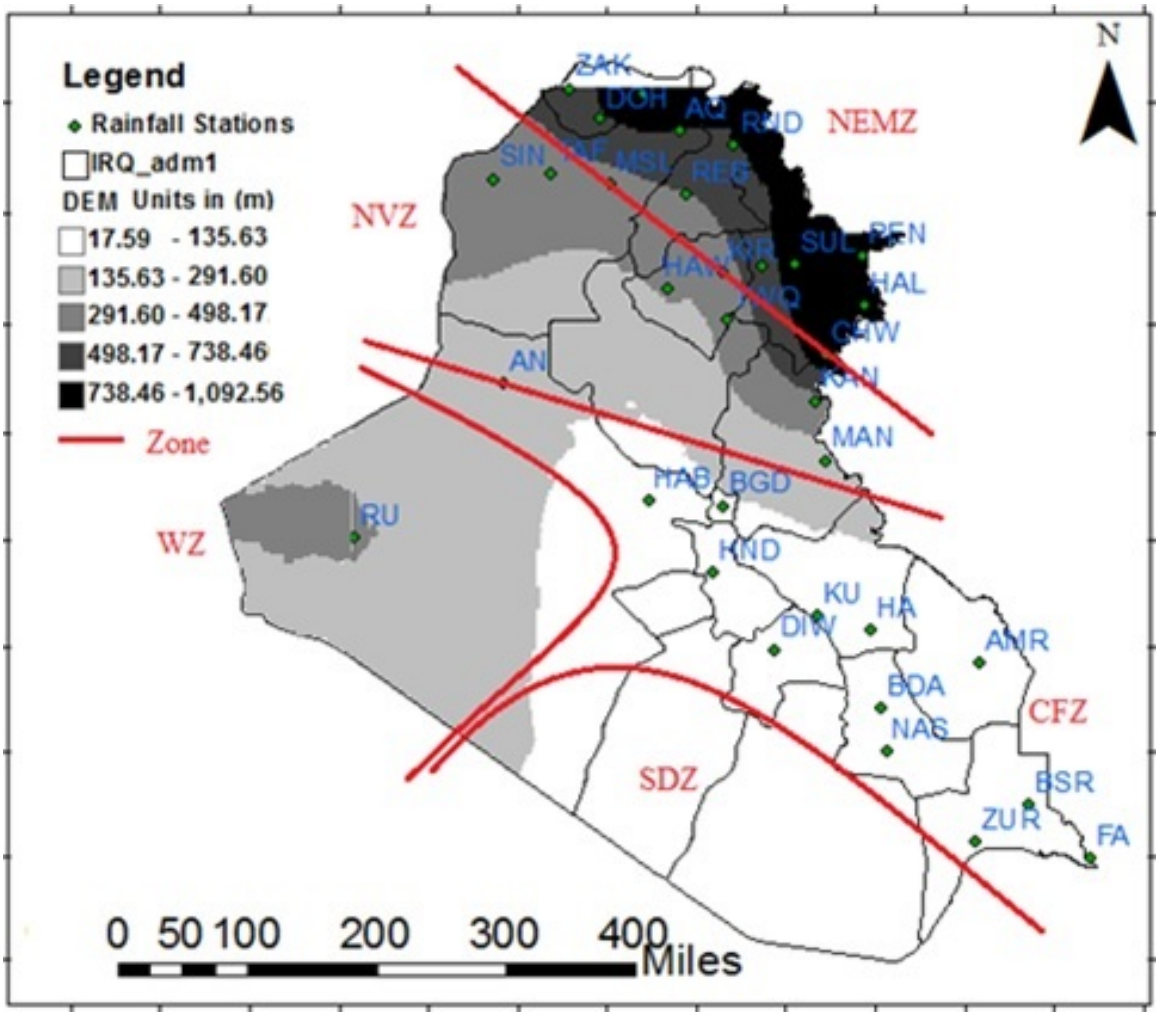

Figure 3.1: The location of climate zones and rain-gauge stations in Iraq. Red solid lines denote the boundaries of the five zones NEMZ, NVZ, WZ, CFZ, and SDZ referred as mountains area in northeast, hills area in north, west area, Central area, and southwestern area, respectively. Rainfall stations are shown in Table 3.2.

curred close to urban and agricultural areas that were experiencing increasing growth of industrialized population, and agricultural soil. Therefore, the SDZ zone will not be considered in our calculations. Table 3.2 shows additional information of the rainfall stations that were chosen to represent all provinces of Iraq including all urban and rural areas.

Table 3.2: Information for all the rainfall stations in the Iraq area.

Station Name	Abb.	Long. E	Latit. N	Altitude m	Station Name	Abb.	Long. E	Latit. N	Altitude m
Amadiya	AMD	43.5	37.08	1210	Hindiya	HND	44.28	32.7	34
Amarah	AMR	47.27	31.85	9	Tawuq	TWQ	44.45	35.05	204
Ana	AN	41.95	34.47	150	Khanaqin	KAN	45.43	34.3	201.2
Aqra	AQ	43.92	36.75	716	Kirkuk	KIR	44.4	35.47	331
Badaa	BDA	46.17	31.43	9	Kut	KU	45.45	32.3	137
Baghdad	BGD	44.4	33.33	150	Mandali	MAN	45.55	33.75	137
Basra	BSR	47.83	30.5	2	Mosul	MSL	43.15	36.27	222
Chamchamal	CHM	44.85	35.53	701	Nasiriya	NAS	46.23	31.02	3
Chwarta	CHW	45.55	34.73	1356	Penjwin	PEN	45.97	35.62	1311
Diwaniya	DIW	44.98	31.98	20.4	Rawanduz	RND	44.53	36.62	690
Dohuk	DOH	43.03	36.87	860	Rutba	RU	40.28	33.03	315.5
Erbil	REB	44	36.18	414	Zubayr	ZUR	47.234	30.15	204
Fao	FA	48.5	29.98	2	Singar	SIN	41.83	36.32	476
Habbaniyah	HAB	43.57	33.37	43.6	Sulaimaniya	SUL	45.2	35.55	853
Hai	HA	46.05	32.17	14.9	Tel Afar	TAF	42.47	36.37	373
Halabja	HAL	45.98	35.18	724	Zakho	ZAK	42.68	37.13	442
Hawija	HAW	43.78	35.32	305					

3.6 Data

Mean monthly observed precipitation data over Iraq are provided by the United States Geological survey (USGS), which was originally obtained from the Directorate of Meteorology of Iraq. This information was available for 33 rain gauges during the period (1935−1958; Figure 3.1). The Global Precipitation Climatology Center (GPCC) dataset was originally gathered from different global datasets named as the total monthly land-surface precipitation. The datasets used in this study are available in reanalysis version 6.0 at 0.5^o grid resolution. The GPCC data was

also derived from rain-gauges (almost over 85,000 stations world-wide), and compiled based on data from Global Telecommunication System (GTS) (Becker et al., 2013); (Huffman et al., 2009); (Xie and Arkin, 1997); (Chen et al., 2002). The GPCC data that compiled based on satellite rain gauge precipitation analysis is used because of its high accuracy (Schneider et al., 2014); (Becker et al., 2013).

3.7 Results and Discussion

3.7.1 Spatiotemporal Variations of Precipitation over Iraq

The spatiotemporal analysis of rainfall was carried out based on the 1923-1958 time period due to: (a) availability of high quality rainfall data for large number of stations with relatively few missing values, i.e., 33 stations during 1923−1958, and (b) unavailability of the rainfall data at a greater number of stations during recent decades due to the past and on going crisis. We used 8 stations that are available during 19802004 for model verification. To evaluate the spatiotemporal variability, we have divided the available data sets into five temporal bands, which are 1935−1940, 1941−1945, 1946−1950, 1951−1955, and 1956−1958. By using a box plot approach, Figure 3.2, we investigated the variability of seasonal and annual patterns of rainfall obtained from 33 stations and based on the five temporal bands defined previously. It can be observed from the Figure 3.2 that the precipitation pattern changes at different temporal bands as well as seasons. For example, medians for winter and annual precipitation (Figure 3.2a, e) were increasing during the initial two periods and then decreases towards end. The median value for spring rainfall (Figure 3.2b) indicates an increasing trend with time. In fall (Figure 3.2d) the median seems to decrease first and reach a minimum during 1946−1950, and then increased afterwards.

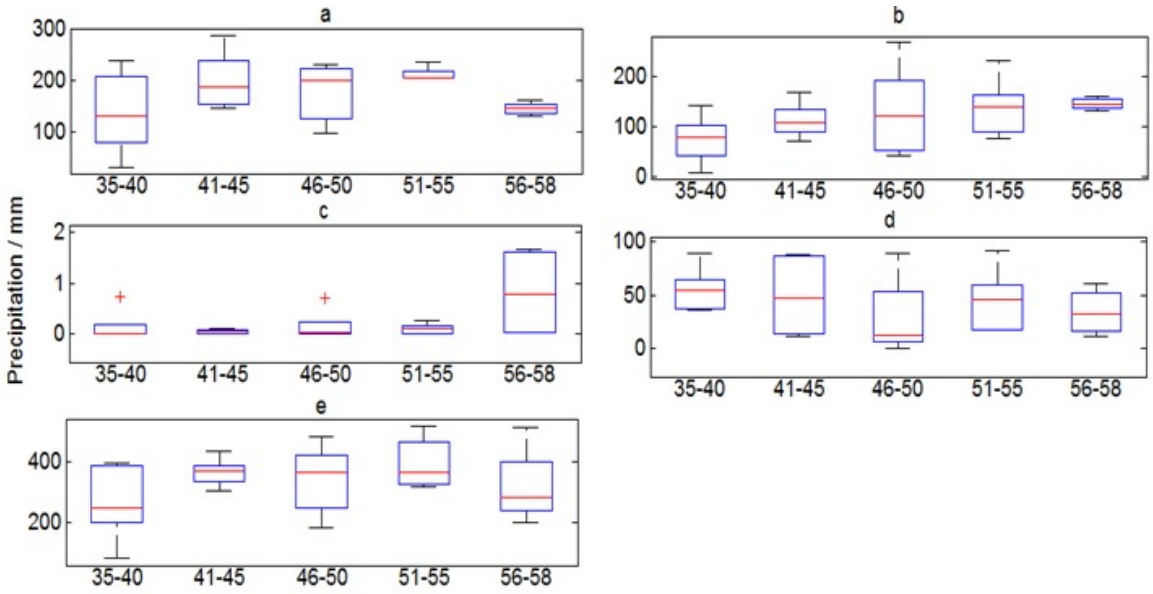

Figure 3.2: Box plots of average precipitation in Iraq for different temporal bands from 1935 to 1958. (a) winter, (b) spring, (c) summer, (d) fall, (e) annual [Note: The x-axis represents time interval, y-axis represents mean annual or seasonal rainfall amount in millimeters].

The mean annual monthly rainfall for Iraq varies from low (79.47 mm in 1935) to high (518.08 mm in 1954) with a mean of 337.94 mm. The variation of annual precipitation (Figure 3.2e) can be utilized to demonstrate the shifting between wet and dry periods occurring with time. For instance, for the period 1935−1940, there was a period of dry spell followed by an increase in average annual rainfall; which is observed after 1940 to reach a long-term average value from 1941 to 1955. Another dry spell occurred after 1956, and it showed less magnitude than the latter dry spell. Iraq experienced a relatively longer wet spell during the period 1941-1955, with 1951-1955 being the wettest during the entire period. It was observed that the seasonal precipitation during the winter season contributes about 52.2% of the annual precipitation, while spring contributes about 35.1%for the annual rainfall. Precipitation during the fall season accounts for 11.7% of the annual and it shows a slowly decreas-

ing trend starting in 1935 to the end of 1950 (Figure 3.2d). Then there is a change point showing an increasing precipitation from 1951 to 1955, followed by a decrease in 1956. The spring data (Figure 3.2b) almost showed a similar trend as in annual precipitation. It should be mentioned that the variations of rainfall during fall season were very high. No summer precipitation was recorded where its amount was 1% of the annual precipitation which can be overlooked.

The records for the same period (1923-1958) are utilized in analyzing the spatial variations of mean annual precipitation. The distribution of observed annual monthly rainfall is exhibited in (Figure 3.3). It was observed that most of the precipitation occurs in the northeast zone (NEMZ; mountains), with highest mean annual rainfall observed at stations PEN (808.85 mm) and AQ (782 mm; see Table 3.2 for the stations reference). A comparatively lower amount of precipitation was observed for cultivated foot hills and lower mountain valleys of the NVZ zone with (500 mm). In the plain areas CFZ and SDZ zones, the mean annual rainfall was usually less than 400 mm, with minimum record near BDA station (60.71 mm). We also noticed a little increase in annual rainfall at ZUR station (450 mm). The WZ zone receives an average annual amount of rainfall (100 mm) with the highest record surpassing 126 mm near HAB station. The above discussion indicates that there are relatively high variations in precipitation recorded in different zones. Observed results confirmed that precipitation amounts were higher in the northern area than in the south. Moreover, precipitation in the plain areas was less than in the mountainous areas. Basically, these changes can be attributed to the topography, climate and land use or cover changes.

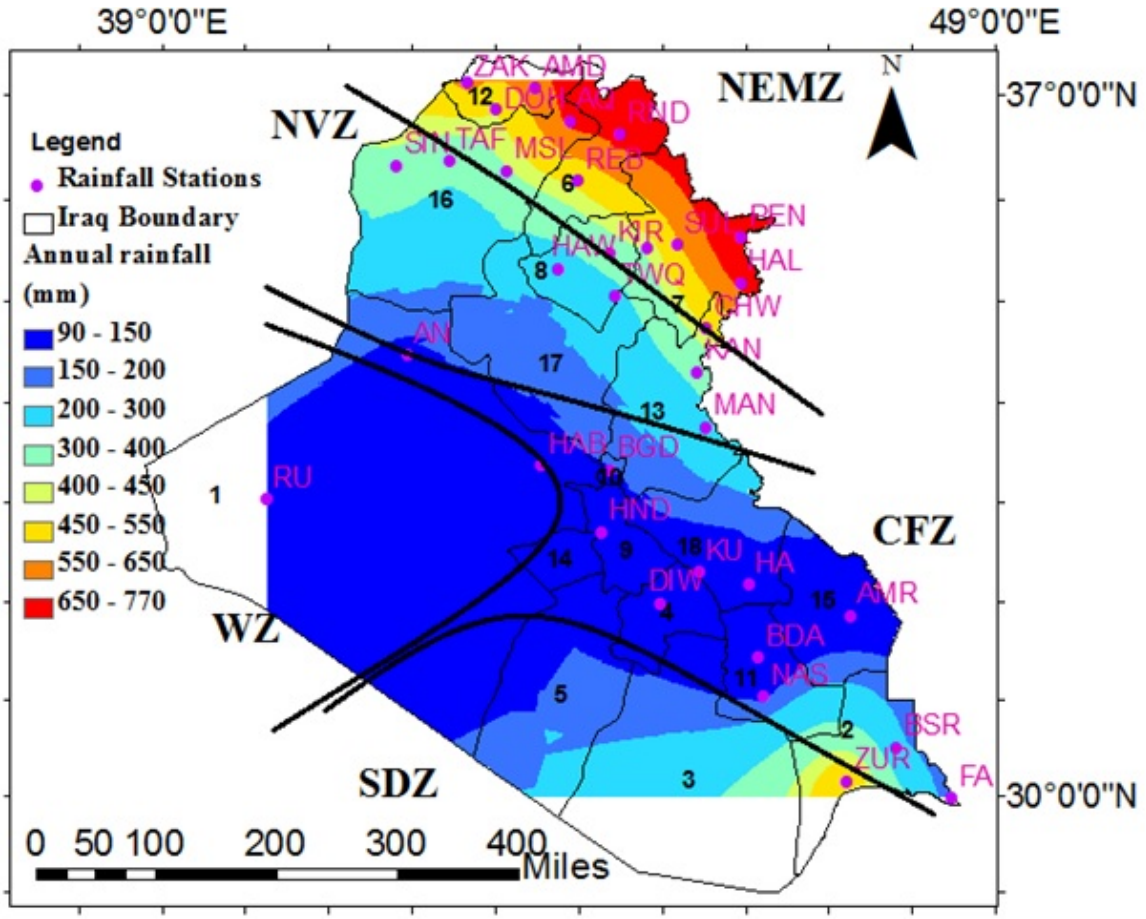

Figure 3.3: Variation of observed average annual precipitation from 1935 to 1958 over different zones of Iraq. Solid black lines represent different topographical terrains: NEMZ, NVZ, WZ, CFZ, and SDZ namely as mountains area in northeast, hills area in north, Western Plateau, Alluvial plain, and desert area, respectively.

3.7.2 Bias Description in GPCC Precipitation Data

We evaluated bias based on the difference between annual/ seasonal observed and GPCC data collected during 24 years of records and presented in (Figure 3.4). Positive biases were observed over NEMZ, and lower parts of SDZ and CFZ zones. The highest positive error values occurred in these zones was during winter (Figure 3.4b). These zones have somewhat higher precipitation records; especially near stations AMB (95.27 mm) and SUL (93.42 mm) in the north and ZBR (147.22 mm) in the south. This indicates that the GPCC data were highly underestimated compared to the observed data over these areas. The magnitude of bias has relatively become negative (over-estimated) along the upper region of NVZ zone. On the other hand, the lowest amount of bias was observed over CZ zone, the upper parts of SDZ, and CFZ zones of Iraq. This is approximately equal to or a bit higher than zero (underestimated) near BGH, and RU stations. Bias during spring and fall (Figure 3.4c, d) shows that the highest underestimated bias were again more concentrated over NEMZ, lower parts of SDZ, and CFZ zones, especially, near stations of AQ (66.06, 32.15 mm), PEN(25.82, 12.63 mm), and ZUR (104.25, 43.51 mm). At the same time, the GPCC data performed well over the central part of Iraq. For example, the lowest bias was observed near HAB (0.98, 1.16 mm) and NAS (0.18−3.72 mm) stations during spring and fall seasons respectively. Further analysis was done (not shown) to check the annual bias. We found that the overall annual mean bias value for Iraq was approximately (0.25 mm/month) implying the GPCC data most of the time was underestimating the observed data. However, it should be noted that the bias values do not necessarily remain fixed during all months, because its value randomly changes according to the time and location.

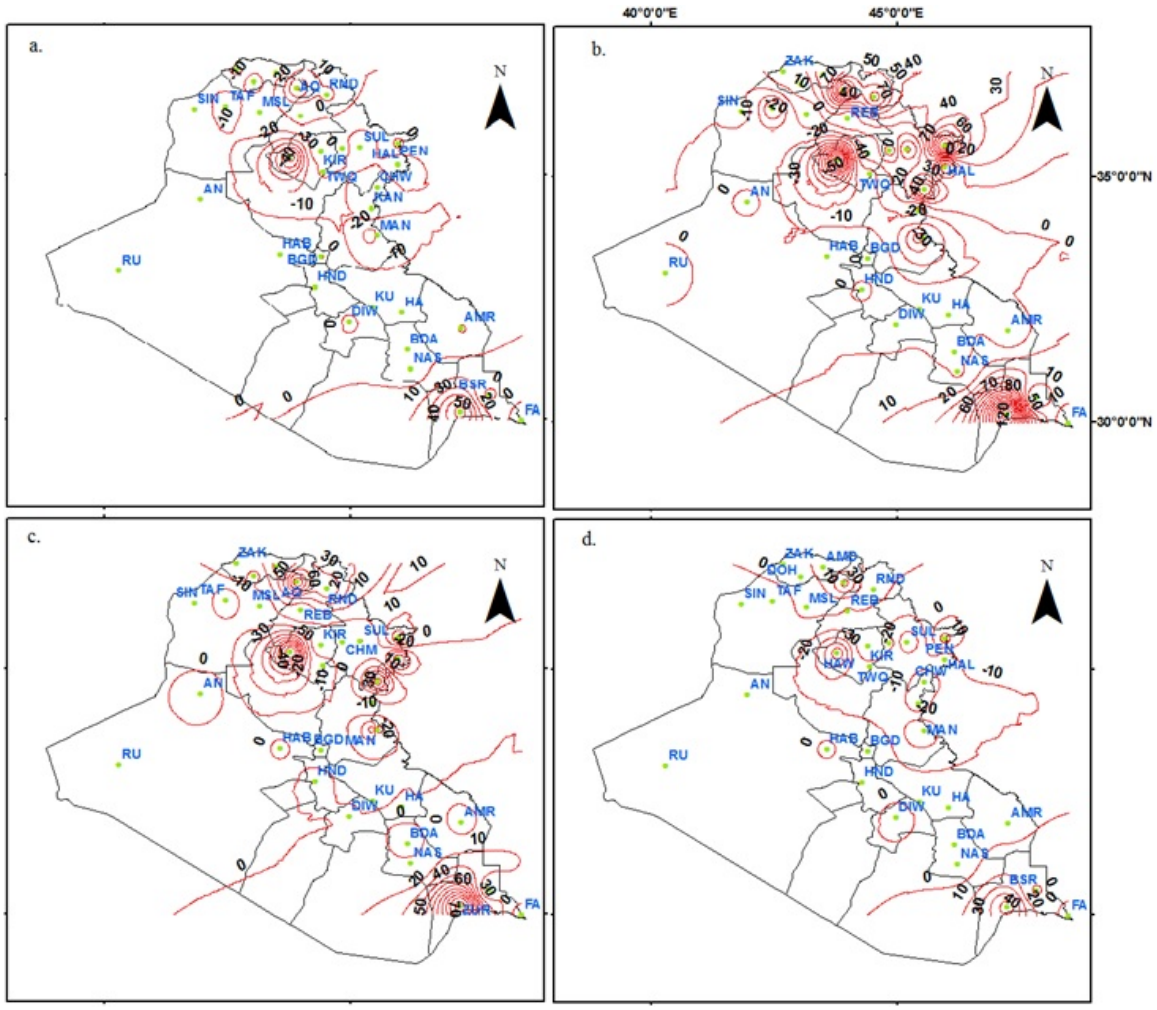

Figure 3.4: Spatial distribution of bias calculated based on the average annual and seasonal monthly observed and GPCC rainfall data for 24 years (1935−1958) over Iraq: a) annual, b winter (January, February, and December), c) spring (March, April, and May), and d) fall (October, and November). The small green dots identify the stations locations.

3.7.3 BCT's for Monthly Rainfall

The five BCT's previously explained were employed to identify the technique that can be used successfully to correct the GPCC data with respect to 33 stations located in different climatic zones. The number of stations successfully corrected by each BCT to the total number of the stations are expressed as a percent and shown in Table 3.3. It was referred as the PI. There are spatial domains where the GPCC data was able to produce the gauge based rainfall data. That is, the GPCC rainfall data for these locations was close to the observed data, so that no bias correction method was required to improve GPCC data. Generally, these percentages (shown in Table 3.3) indicate that there were a good number of spatial locations where GPCC data can be used directly without correction.

Table 3.3: Performance Index (PI) of individual BCT.

BCT	Jan	Feb	Mar	Apr	May	Oct	Nov	Dec	Wet	Ave.
GPCC	27.27	33.4	27.3	30.4	24.3	9.1	24.3	33.4	33.4	18.2
Q	27.3	30.4	27.3	36.4	36.4	48.5	24.3	39.4	27.3	30.4
B	24.3	24.3	30.4	18.2	15.2	21.2	30.4	12.2	18.2	30.4
M	15.2	6	12.2	15.2	9.1	12.2	12.2	12.2	12.2	15.2
S	0.0	3.0	3.0	0.0	0.0	6.0	6.0	0.0	0.0	3.0
R	6.0	3.0	0.0	0.0	9.1	3.0	3.0	3.0	0.0	3.0

Spatial locations of the best selected BCT's for the months of January, February and December are shown in Figure 3.5. In the case of January, it was found that 27.27% of the stations comparatively matches well with GPCC data (Table 3.3). Most of these stations are located along the northeastern (mountains; NEMZ) zone, which relatively receives high precipitation (Figure 3.5a). GPCC data series performed better for those locations wherein the rain gauge was located within a GPCC grid. For example, for MSL station (Figure 3.6), the observed, GPCC and bias cor-

rected January rainfall suggests a close match, which is evident since none of the BCTs was able to improve the original GPCC data. The majority of the stations located along the CFZ zone were successfully corrected using the quantile method (Q) and it represents 27.3% of total number of stations. Some of the stations located in the NVZ and NEMZ zones, the multiple shift technique (M) fits better for very wet stations with 15.2% PI. It was found that the PI of the Bias technique (B) was also high (24.3%), and they are more concentrated in the east of CFZ and NEMZ zones. It should be mentioned that GPCP rainfall products along the southern regions of Iraq for January has more uncertainty in reproducing the observed rainfall. As an example, this is evident based on time series plotted between gauge, GPCC and bias corrected data for KUT station (Figure 3.7) for the month of January (1935-1958).

For February and December (Figure 3.5b, c), the results for the NEMZ zone (mountains) and some parts of CFZ zone provides the best fit between GPCC and observed data. Throughout these 2 months, the PI was 34.4% for both months. The best performance among all zones based on all BCTs was observed for quantile method(Q) with PI of 30.4 and 39.4% for February and December respectively. For bias method (B), the PI reached up to 24.3% during February, and a somewhat lower PI for December with 12.2% (Table 3.3). The locations of stations corrected by these two techniques were concentrated in the CFZ zone, as well as the north of NVZ zone. On the other hand, the lowest performance during the months of January, February and December was recorded for multiple shift technique (M) with PI of 6.1% during February, except January and December where the PI was relatively high with 15.2 and 12.2% respectively. For Standard reconstruction technique (S) the performance was low with PI of (0, 3, and 0%), and for regression techniques (R) it was (6, 3, and 3%) for January, February, and December, respectively.

The information regarding the locations of BCT's during the months of March,

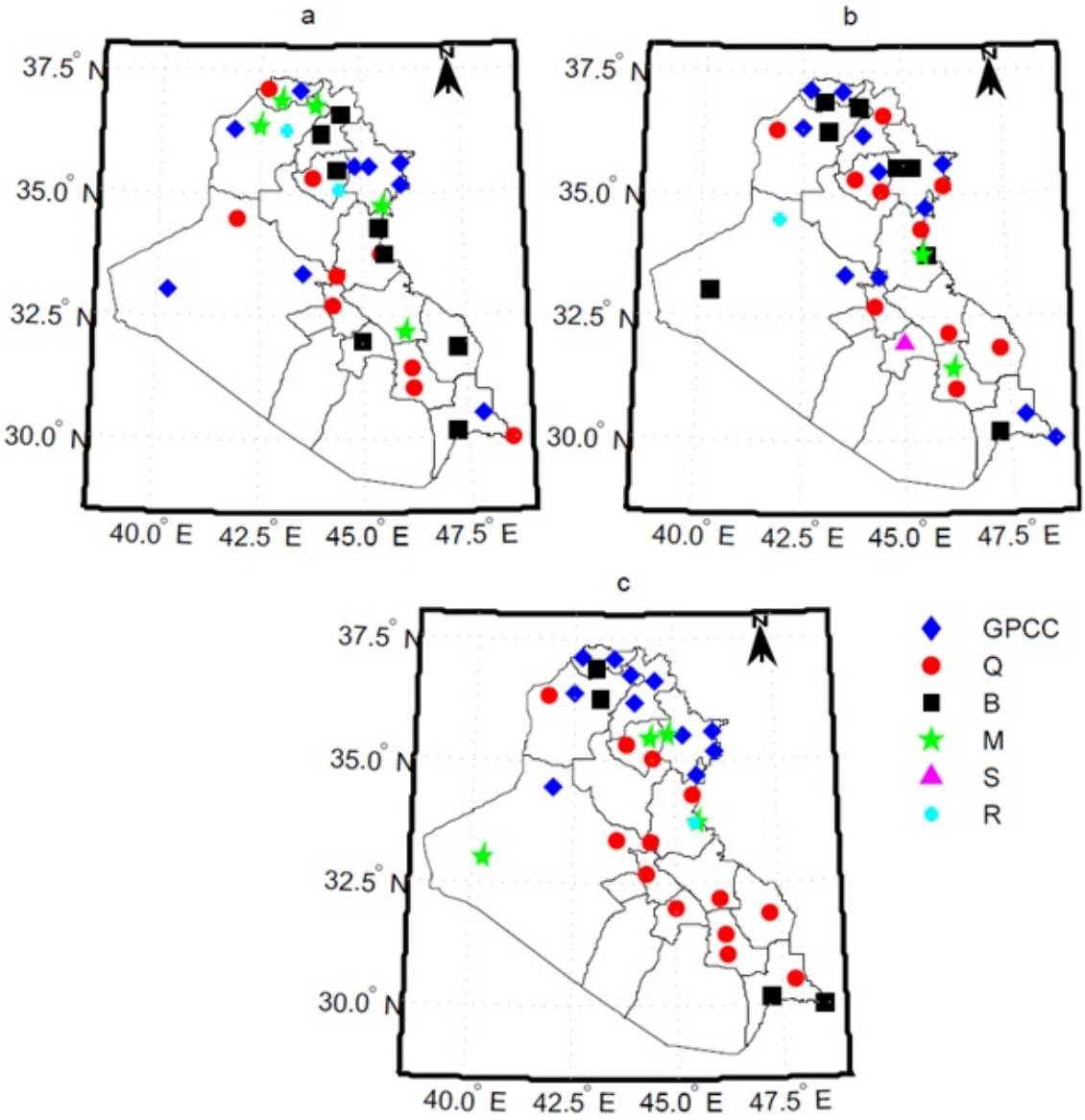

Figure 3.5: Distribution of Bias correction techniques (BCT's) for during winter months: a) January, b) February, and c) December.

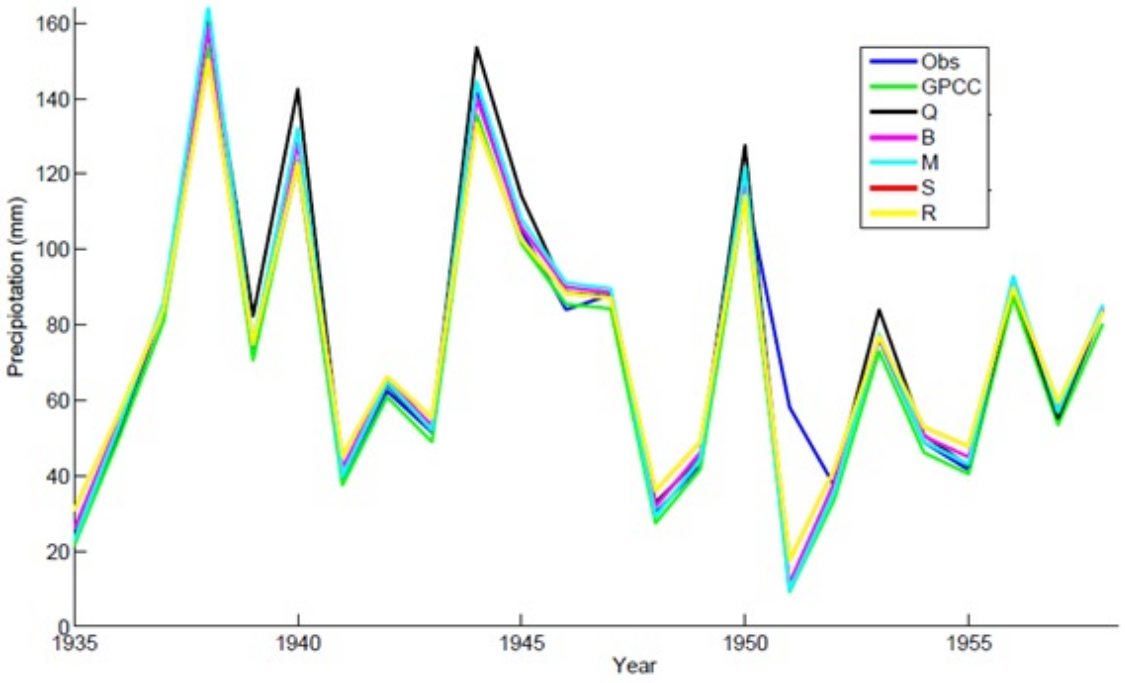

Figure 3.6: Time series showing gauge, GPCC and bias corrected data for MSL station for the month of January (1935-1958).

April, and May is provided in (Figure 3.8). For these months, the performance of the GPCC data was comparatively good in simulating the observed rainfall at stations located mainly at Mountains (NEMZ), NVZ, and east and middle of CFZ zones with PI of 27.3, 30.4, and 24.3% during March, April, and May respectively. Also within these months, bias values appear to be relatively higher over the south of CFZ and WZ zones. Apparently, three BCT's were significantly skillful in correcting the GPCC when compared to other methods. The quantile mapping technique (Q) has the most acceptable PI with 27.3% for March, and 36.3% during both April and May. The stations corrected using this method were concentrated in NEMZ and east of CFZ zones. The multiple shift technique (M) appears to be more common in the NVZ and south of CFZ zones with a PI of (12.2, 15.2, and 9.1%) for March, April, and May respectively. The bias technique (B) is more likely to spread over NVZ and some locations in CFZ zones with PI of (18.2, 15.2%) for April and May, and little higher for March (30.4%) see (Table 3.3). However, the Standard reconstruction (S) and Regression (R) techniques have the lowest PI during all 3 months. The PI values for Standard reconstruction technique (S) during March, April, and May were 3, 0, and 0% respectively. For the Regression (R) technique, it was 0, 0, and 9.1% during March, April, and May respectively. These S and R based stations were located more towards northeast of NVZ and southeast and south of CFZ zones.

The results of BCT's for the months of October and November are presented in (Figure 3.9). It was observed that the number of stations with their GPCC rainfall data better representing the observed rainfall were relatively higher in November than October with PI of (24.3 and 9.1%) respectively (Table 3.3). The distribution of these methods showed that they were more focused in the NEMZ and CFZ zones for November, while for October in the east of CFZ zone. Again both the Bias (B) and quantile mapping (Q) were the best techniques during the 2 months and their

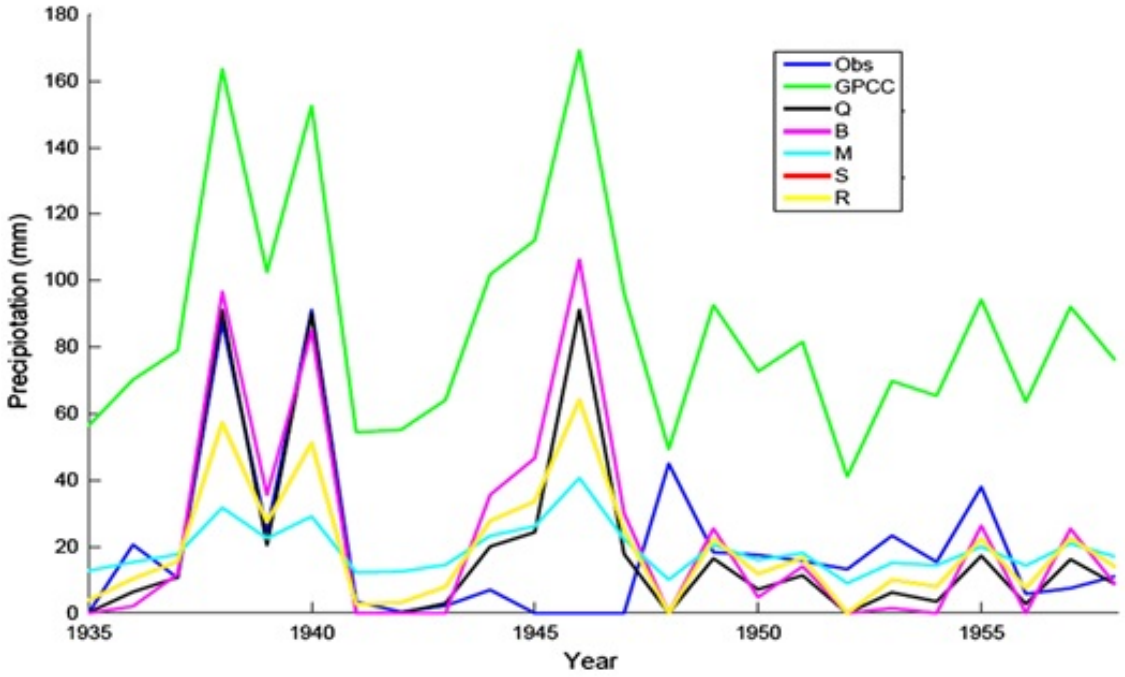

Figure 3.7: Time series showing gauge, GPCC and bias corrected data for KUT station for the month of January (1935−1958).

PI were (48.5, 21.2%) for quantile mapping (Q), and (21.2, and 30.4%) for Bias (B) during October and November respectively. The stations per- formed well using bias technique (B) was located mostly over NEMZ zone during October and over CFZ during November. The quantile (Q) technique stations were more over the NEMZ, NVZ, and WZ zones during October and November.

3.7.4 BCT's for seasonal rainfall

The evaluation of seasonal precipitations is another important quantity in our analysis as their variations are the key factor in understanding rainfall distribution throughout the year and its relation to the droughts in the drainage areas. Seasonal result showed a clear difference between correction methods. The wet season includes the four rainiest months (December, January, February, and March). The average

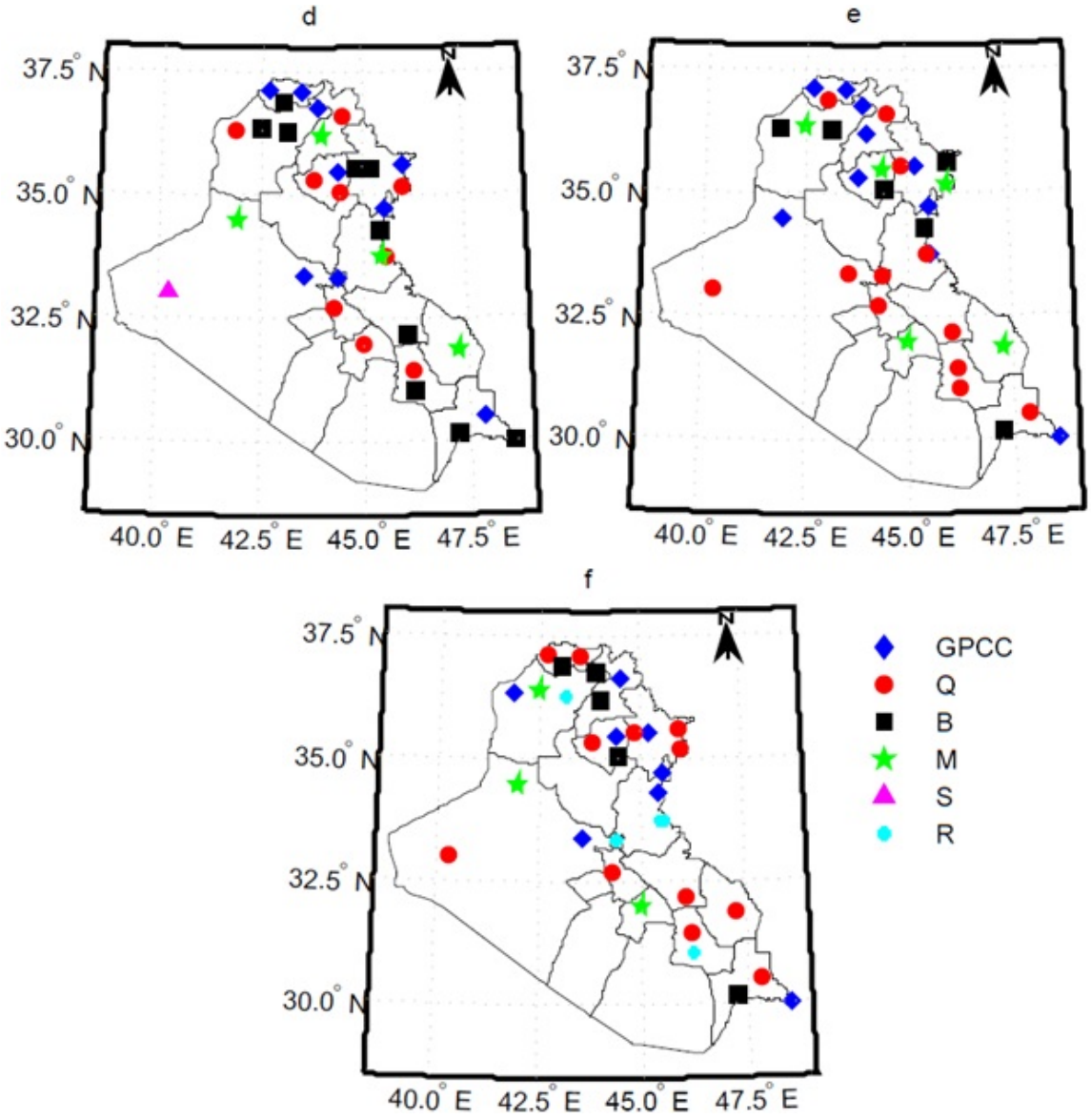

Figure 3.8: Distribution of Bias correction techniques (BCTs) for GPCC data during spring months: a) March, b) April, and c) May.

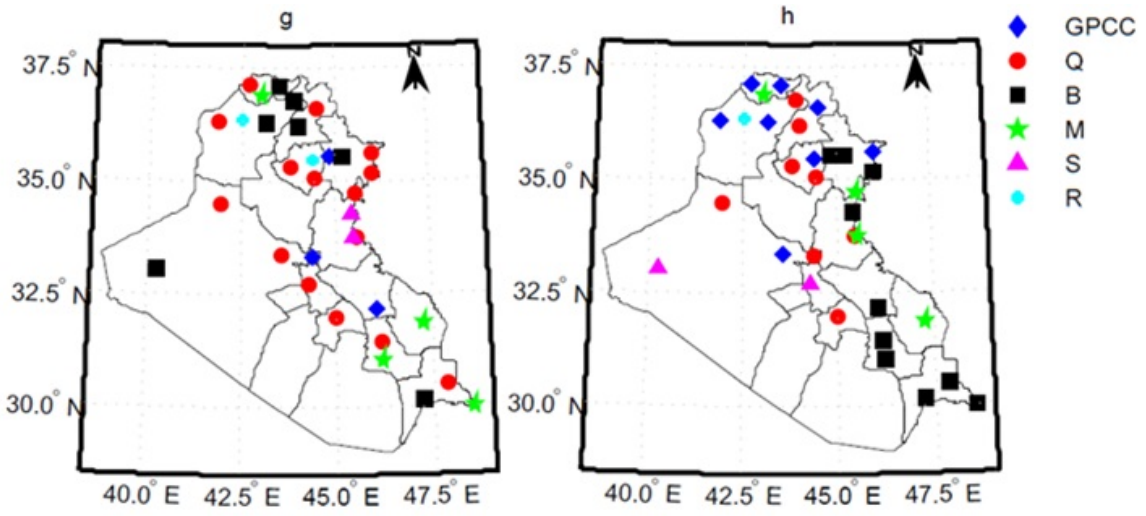

Figure 3.9: Distribution of Bias correction techniques (BCT's) for GPCC data during months of: a) October, b) November.

season consist of 4 months with relatively lower rainfall (April, May, October, and November). The BCT's results for both wet and average seasons are presented in (Figure 3.10; Table 3.3). The PI of original GPCC data during wet season (33.4%) was higher than the average season (18.2%). The original GPCC data performed better during wet seasons were mostly located in the northern part, NEMZ zone, which relatively receives higher amounts of precipitation, while the locations during average season is shifted a bit towards the southern part, NVZ and CFZ zones, which receive somewhat lower rainfall.

In terms of the BCT's, it appears that both quantile (Q) and Bias (B) techniques have the highest performance with PI of 27.3, 18.2% for the wet season respectively, and both methods have PI of 30.4% for the average season. The spatial distribution of the latter method found to be concentrated over the NVZ zone with a little spread over e other zones for both seasons (Figure 3.10). The performance of other bias correction techniques (M, S, and R) was significantly lower than the other

two methods (Q and B) in correcting the GPCC data where PI ranged from 0 to 15% in the best cases.

3.7.5 Verification of BCT's for recent dataset

The BCT's developed during 1935-1958 was used to validate the recent (1980-2004) GPCC data. The observed records for the recent time period (19802004) were avail- able for 8 stations out of the 33 stations used previously. These available stations (8 nos.) are spread over different climatological zones, which include MSL, KIR, RU, BGD, DIW, HA, NAS, and BSR (Table 3.2). The verification was done in two steps: (a) First, the monthly and seasonal GPCC precipitation data for the 8 stations during the period (1980-2004) was corrected based on BCT's developed corresponding to the observed data (1935-1958), (b) Second, the corrected GPCC data was evaluated against the observed gauge data for the period (1980-2004) using the seven GOFs. We have presented results based on the three commonly used GOF's: R, RSR, and d.

It was observed that in some stations the uncorrected GPCC data represents the observed data very well, which concur with our previous findings. For instance, the GPCC bias corrected January month precipitation (1980−2004) for MSL station shows a good agreement (Figure 3.11). The PI of each BCT estimated for eight stations were evaluated using three selected GOFs is shown in (Figure 3.12). The correlation coefficient (R) between observed and GPCC uncorrected data shows a moderate agreement as the values of R values varies from 0.4 to 0.65. After the correction was made, there was a relative improvement in the values of R among all BCT's. Based on the R as goodness of fit, the performance of quintile mapping (Q) performs well for January, March, October, November and December as well as wet

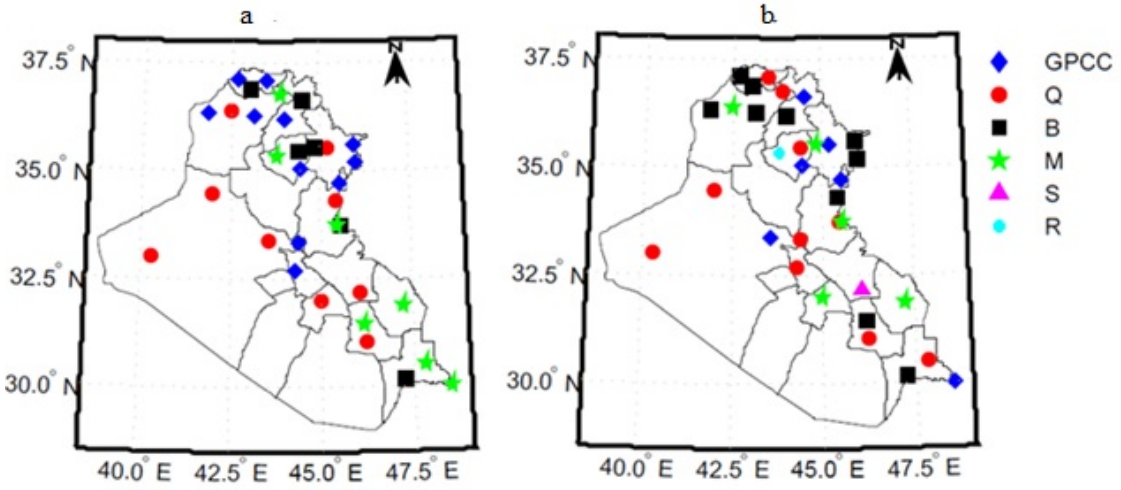

Figure 3.10: Distribution of Bias correction techniques (BCT's) for GPCC data during, a) Wet Season, and b) Average season.

season. The maximum value was recorded in December for quintile technique (Q) and in February for bias technique (B) with PI of 87.5 and 62% respectively. Then they decreased during relatively dry months, reaching their minimum during May for Q technique and in April for B technique with PI close to 13% for both methods. For February, the PI of M, S, and R methods was relatively high (62%) for all three methods. It can be noted that Q technique performed better for wet months while B technique worked for average months.

RSR values for all BCT's (Figure 3.12b) indicate that the variation in errors were relatively small and they reach their minimum for the B and Q technique and the maximum performance of the two techniques was observed during the month of December for Q method and B method during May and October. Other methods M, S, and R seem to have better performance during wet season. We used Willmott index of agreement (d) to measure the correction efficiency for each BCT. The comparison of d revealed that the Q and B techniques were the most efficient methods for correcting the GPCC data. The highest PI was for Q technique (87%) during December, while

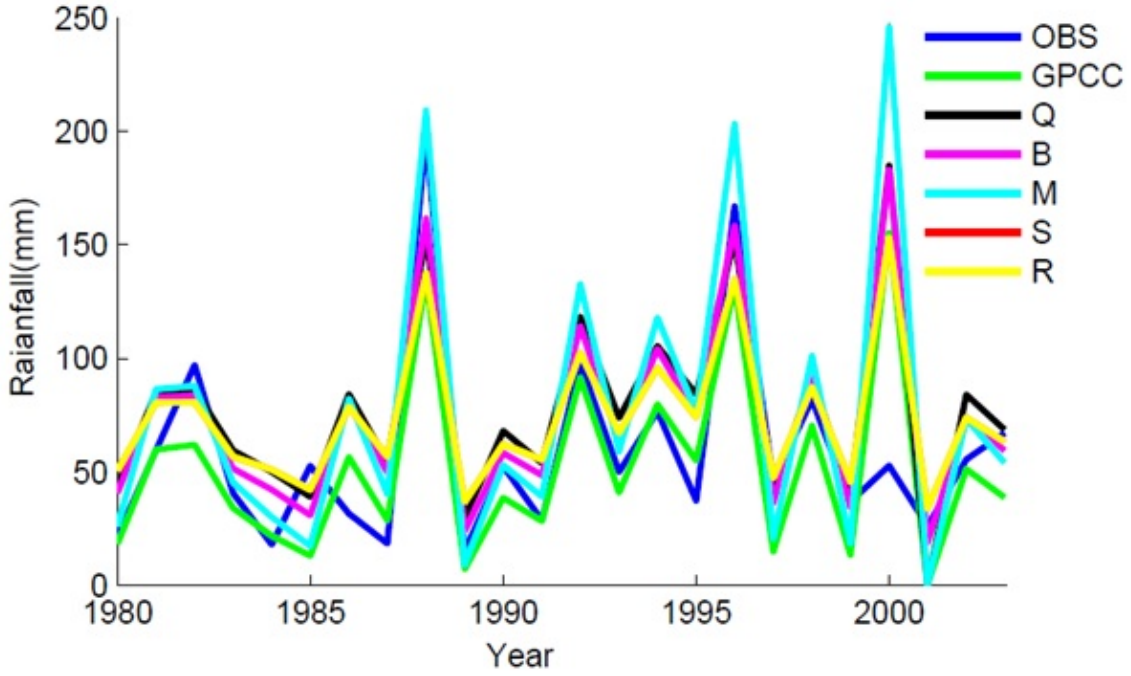

Figure 3.11: Time series showing gauge, GPCC and bias corrected data for MSL station for the month of January (1980-2004).

for B technique it was 75% during May. The lowest performance was observed for Q technique during October and B technique in February. The Q method was the best BCT for correcting the GPCC during the wet months, while B performs well for the months with moderate rainfall (May, October, and November) (Figure 3.12c). Overall, verification the GPCC data for recent periods (1980-2004) approximately revealed the similar information observed during model development period (1935-1958).

3.8 Summary and conclusion

We evaluated and compared five different bias correction techniques (BCT's) to correct the GPCC precipitation data with respect to gauge precipitation located in

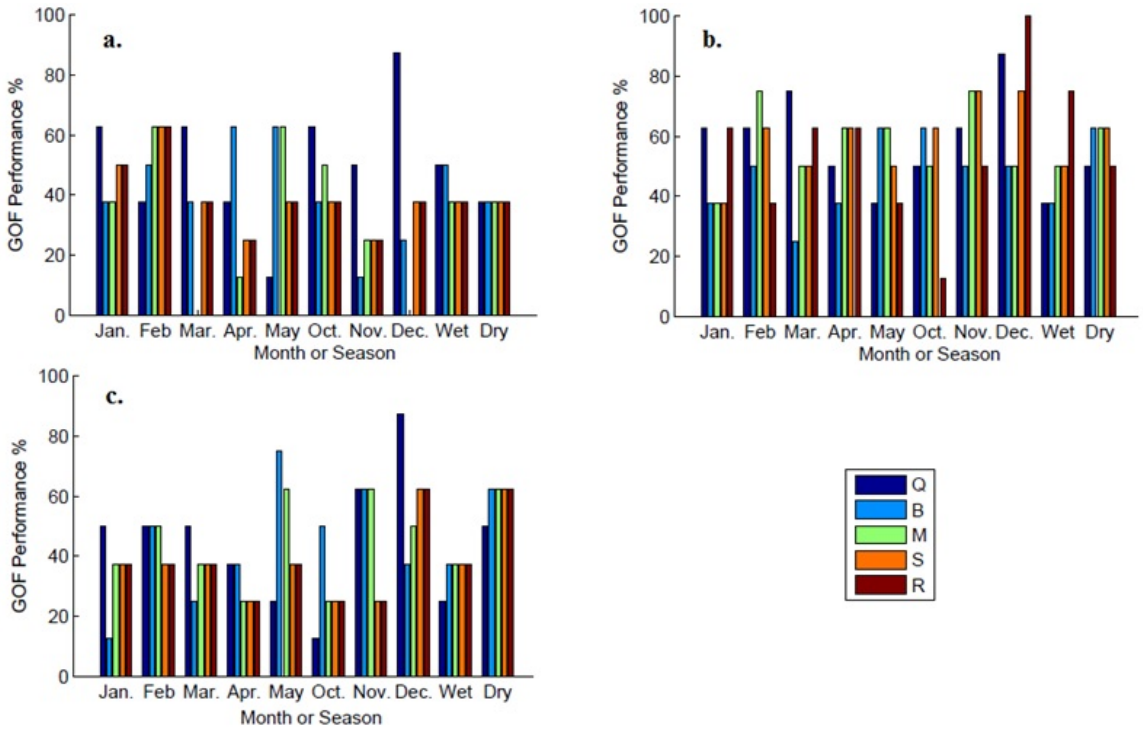

Figure 3.12: Goodness of fit test results for the bias corrected monthly and seasonal GPCC precipitation for the period (1980−2004). Columns indicate the percentage of BCTs performed well based on: a) correlation coefficient (R), b) standard deviation ratio (RSR) test, and c) Willmott index of agreement (d).

a semi-arid climatic zone. These BCT's were applied at different spatial domains (i.e., different precipitation zones) as well as temporal scales (i.e., monthly and seasonal). The BCT's were calibrated based on GPCC data for the time period of 1935-1958 and validated during 1980-2004. In general it was observed that quantile mapping and mean bias remove technique performs well in comparison to multiplicative shift, standardized-reconstruction and linear regression approach. The quantile mapping technique performs well in comparison to the mean bias remove technique during wet season and associated months. Both these techniques perform satisfactorily during average rainy season. There are spatial domains where the GPCC data was able to produce the gauged based rainfall fairly well without applying any BCT's. This study suggests that instead of using a single bias correction technique at different climatic regimes, multiple BCT's needs to be evaluated for identifying appropriate methodology that suits local climatology.

Chapter 4

Hydrologic Evaluation of Satellite and Gauged Based Precipitation Products in Tigris River Basin

4.1 Abstract

This study investigates four widely used satellite and gauged-based precipitation products for hydrologic evaluation in poorly gauged Tigris River Basin (TRB) (Area: 445,656 km^2) using Soil and Water Assessment Tool (SWAT) watershed model. The satellite rainfall products evaluated in this study includes Precipitation Estimation from Remotely Sensed Information using Artificial Neural Networks-Climate Data Record (PERSIANN-CDR), Multi-Source Weighted-Ensemble Precipitation (MSWEP), Asian Precipitation Highly Resolved Observational Data Integration Towards the Evaluation of water resources project (APHRODITE), and NOAA Climate Prediction Center (CPC) data. Overall APHRODITE precipitation data was able to capture spatiotemporal distributions and streamflow simulations for the

selected streamflow stations. On the other hand, MSWEP (CPC) overestimated (underestimated) the observed rainfall climatology and had similar effects on streamflow simulations. Among all the selected precipitation products, the relative performance of CPC is poor in comparison to other data sets. PERSIANN-CDR data performed well in streamflow simulations at selected stations within TRB. Thus, PERSIANN-CDR data can be considered as a reasonable remote sensing product for poorly gauged TRB.

4.2 Introduction

Hydrological models are useful tools for investigating hydrological processes in watersheds with limited hydrological measurements (Amisigo et al., 2008; Li et al., 2009; Abbaspour et al., 2015). The precipitation is one important driver for hydrological models to study surface and subsurface water flow and drought analysis in any watershed (Beven, 2011; Miao et al., 2015). The availability of precipitation estimates from multi-source data (i.e., satellite and radar data, interpolated from actual observations, or a combination of all) extended the application of hydrological models to areas where the actual observations are scarce. However, the quality, reliability, and the spatiotemporal variability of these precipitation data sources (PDS) need validation prior to their sectoral applications. Failure in representing the accurate spatiotemporal variability of precipitation may lead to errors and uncertainties in stream flow predictions especially in basins poorly represented by actual rain gauge network (Faurès et al., 1995); (Taesombat and Sriwongsitanon, 2009; Mishra and Singh, 2010; Andréassian et al., 2012). Therefore, it is important to validate the ability of a hydrological model driven by various PDS to simulate the actual streamflow information for a specific region especially with scarce precipitation data and

to evaluate the errors associated with each precipitation data source (Yang et al., 2015). For this purpose, the Soil and water Assessment Tool (SWAT; (Arnold and Fohrer, 2005)) hydrological model is utilized in this study due to its effectiveness in evaluating streamflow and water quantity (quality) (Gassman et al., 2007).

Several remote sensing (satellite-based) precipitation products recently evaluated (validated) against in-situ precipitation for streamflow simulation using hydrological models (Behrangi et al., 2011). The ongoing efforts for improving remotely sensed measurements have produced many high-resolution (< 4 km) and temporal (< 3 hours) precipitation products (Sorooshian et al., 2000). Recently there are several studies evaluated the performance of satellite-based precipitation products to predict streamflow in data sparse regions using hydrological models. For example, (Thiemig et al., 2013); and (Zhu et al., 2016) evaluated the use of satellite precipitation data in the hydrological applications and reported that two satellite-based precipitation products named TRMM and PERSIANN-CDR performed better in comparison to the reanalysis gauged-based data. Many studies have concluded that satellite-based precipitation products could be potentially used for hydrological predictions particularly for un-gauged basins (Xue et al., 2013; Jiang et al., 2012).

The uncertainty associated with hydrological models, especially when using different model inputs greatly affects the model performance. This may lead to less meaningful and sometimes misleading predictions if such uncertainties are not addressed in the calibration process (Vrugt and Bouten, 2002; Schuol and Abbaspour, 2006; Yang et al., 2007a; Yang et al., 2007b). In model calibration, instead of relying on a single model prediction, statistical methods are used to represent uncertainties in hydrological models, where such uncertainties are given a probabilistic range to account for several sources of errors in the model (Franz et al., 2010). The simplest statistical method is the first order approximation, which uses a linear objective function.

This approach does not account for correlation between model parameters (Vrugt and Bouten, 2002). More complex algorithms such as Sequential Uncertainty FItting (SUFI), Monte Carlo-based algorithms, and Markov Chain Monte-Carlo (MCMC) have been successfully applied to provide improved meteorological and hydrological predictions as well as to represent uncertainties in hydrological model parameters (Bates and Campbell, 2001; Blasone et al., 2008; Gallagher and Doherty, 2007). Although SUFI optimization method requires a massive number of simulations, it is very robust in predicting the parameters uncertainty and the corresponding streamflow simulations (Abbaspour et al., 1997; Abbaspour et al., 2004) and this method was applied in this study.

For the last few decades, the water scarcity in the Lower part of Tigris River Basin (LTRB), situated in Iraq has remarkably increased. This is highly attributed to the intense water management practices (including dam constructions, irrigation systems, and meeting drinking water demands) implemented in the Upper part of Tigris River Basin (UTRP), located in Turkey and Iran (Wilson, 2012; Voss et al., 2013; Bozkurt and Sen, 2011; Issa et al., 2014). The analysis of water resources in such watershed is challenging due to scarcity of observed precipitation data caused by the ongoing conflicts and political instability (Marghany et al., 2016). The main objective of present study focuses on three aspects: (a) to evaluate the spatiotemporal heterogeneities of the four PDS (APHRODITE, MSWEP, CPC, and PERSIANN-CDR) compared to actual gauge data over the TRB, (b) to evaluate the suitability of using these PDS to simulate streamflow in such a large river basin with limited hydroclimate information, and (c) the predictive uncertainty in simulating streamflow using three calibration approaches was compared to improve streamflow simulation. The results of this study will provide an insight into the importance of validating multiple PDS for hydrological modeling when precipitation data are inadequate or

unavailable.

4.3 Study Area

This study was conducted on the Tigris River Basin (Figure 4.1a). The TRB encompasses a total drainage area of around 445,656 km^2, of which 56.1% is in Iraq, 24.5% in Turkey, 19% in Iran, and 0.4% in Syria (UN-ESCWA and BGR, 2013). The TRB has nine major tributaries, most of which originate in Turkey and Iran and eventually meet Tigris River in Iraq (Shahin, 2007; Frenken et al., 2009). Approximately 30% of the TRB land is covered by intense agricultural areas (Figure 4.1b), 26% is mainly covered with grassland, 35% is arid land, and the remaining 9% represents settlements in the basin (Kibaroğlu, 2002). Based on the Digital Elevation Map (DEM) of the area, the topography of the TRB is highly variable where the elevation ranges from few meters in the south (lowlands) to 4356 m above the sea level in the northeast (highlands).

The TRB is characterized by its transitional climate from semi-humid in the headwaters (highlands) to semi-arid (lowlands) (Ajaaj et al., 2016). The resulting change in elevation from the north to the south creates a strong spatial distribution of precipitation in the TRB. In TRB, most of the rain occurs between November and April, reaching maximum during winter months (December-February). The rest of the years (May-October) are dry particularly from June to August. Since most of the winter precipitation occurs in the mountains (UTRB), it is mostly stored as snow pack. Therefore, the resulting flow of the Tigris River is seasonal and dominantly relies on snow melt during spring season, March-May (Jones et al., 2008). Given the semi-arid climate of the LTRB, the evaporation causes a considerable loss of water from this part of the basin. Mean air temperature ranges from -35^{o}C in winter

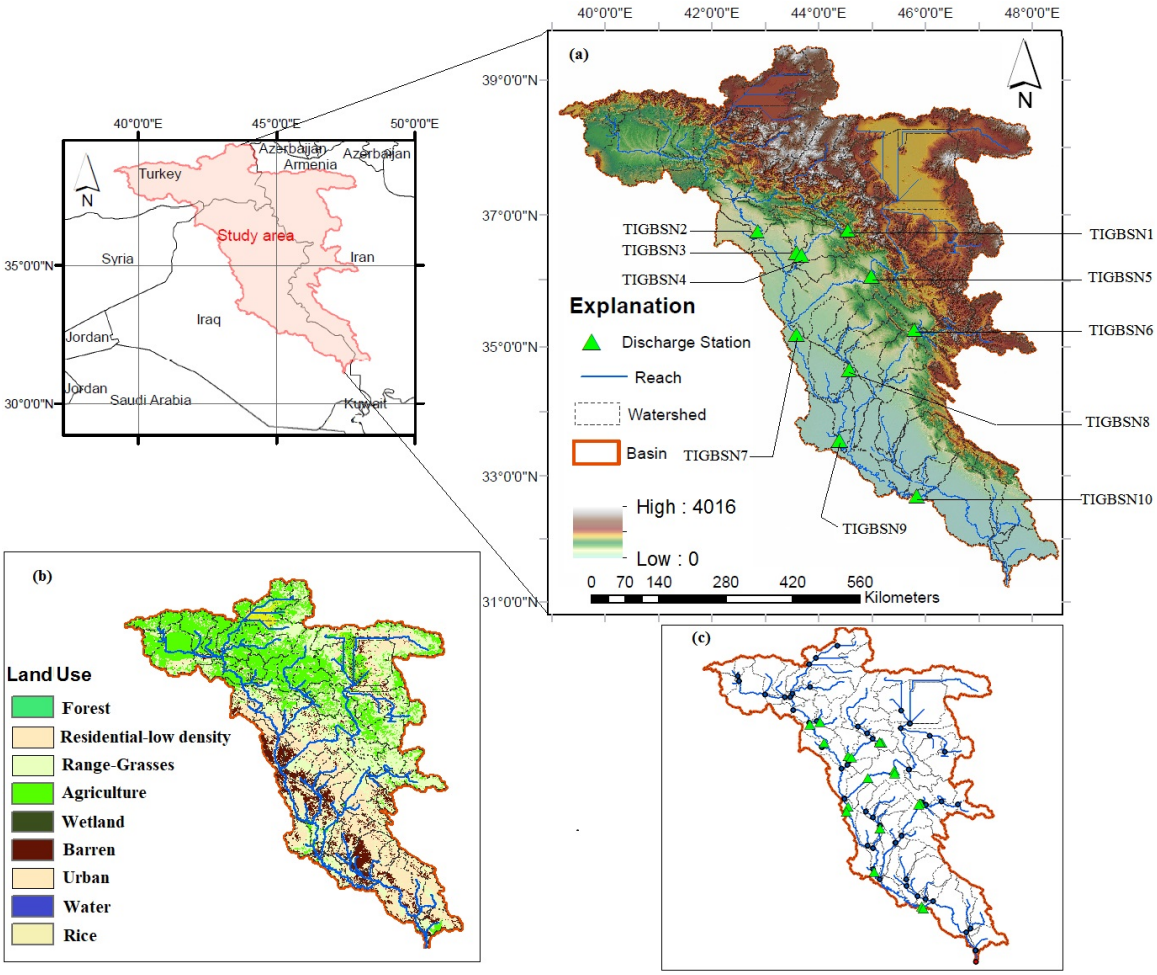

Figure 4.1: Tigris River Basin location map: (a) DEM with stream gauges, (b) land use map, (c) subbasins with outlets (blue dots).

(mountains) to 40^{o}C in summer (Mesopotamian plain in the south of the TRB; UN-ESCWA and BGR, 2013).

In mid-1970's, a general regional water resources plan was implemented in the UTRB aimed at increasing water withdrawal for agricultural, industrial, and municipal water supply (Tigrek and Kibaroglu, 2011). Consequently, a progressive reduction in the flow of the Tigris River has been noticed in the LTRB, especially during dry season months (May-October). This has resulted in a loss of about 25% of the irrigated areas and drying up of most of the marshlands in the LTRB (Jones et al., 2008). For example, the mean annual flow rate at Kut station (Southern LTRB) has reduced by 50 m^3s^{-1} from 1931-1973 to 1974-2004. The mean annual precipitations over the entire river basin for these two time periods are the same (473.34 mm and 472.80 mm, respectively), which makes the LTRB vulnerable to extreme drought under such management plans (Wilson, 2012; Issa et al., 2014).

4.4 Hydrological Model

SWAT is a popular hydrological and water quality model developed by the USDA-Agricultural Research Service (USDA-ARS). It is a long-term, lumped, continuous, watershed-scale simulation model designed to assess the impact of different management practices on surface water, sediment, and agricultural chemical yields on sub-basin scale (Arnold and Fohrer, 2005). The watershed in SWAT is classified into multiple sub-basins that are further divided into unique combinations of land use, soil type, and slope known as Hydrologic Response Units (HRUs). SWAT performs its calculations for each HRU then scales it back to sub-basins based on the percentage of each HRU in that sub-basin (Wible, 2014). This hydrological model is based on water balance equation (Arnold et al., 1998) as given by Eq.(4.1). In this equation, SW_t

is the soil water content at time t, SW_o is the initial soil water content, R, Q, ET, P and QR are the precipitation, runoff, evapotranspiration, percolation, and the return flow, respectively, all measured in (mm) and at the time t in (day).

$$SW_t = SW_o + \sum_{t=1}^{n}(R - Q - E - P - QR) \tag{4.1}$$

SWAT commonly uses two methods to estimate the surface runoff (infiltration) including the Soil Conservation Service (SCS) and the Green-Ampt infiltration method (Arnold et al., 1998). In this study, the SCS curve number method is chosen to model surface runoff in SWAT model. Three methods are used to simulate evapotranspiration in SWAT model including Penman-Monteith, Priestley-Taylor, and Hargreaves. Penman-Monteith is used in this study as it counts for wind speed, air temperature, relative humidity, and different land uses (Arnold et al., 2012), and has shown good empirical simulations (Earls and Dixon, 2008). In SWAT, the snow is simulated as an equivalent depth of water as it is packed with different densities. The precipitation within an HRU is classified as snow if the mean air temperature drops below the snow melt temperature threshold, which is determined through calibration (Wang and Melesse, 2005). The subsurface system in SWAT is modeled as two components, shallow and deep aquifers. The shallow aquifer receives water from the unsaturated soil profile with a delay estimated using an exponential delay function, while only a fraction of the total recharge can percolate to the deep aquifer and eventually out of the system (Arnold and Fohrer, 2005). SWAT model routes surface water as a volume through the channel network using either the variable storage routing method or the Muskingum routing method (used in this study). Both methods utilize the channel inputs including the reach length, channel geometry, floodplain slope, and channel roughness to estimate outflow at the end of each day (Arnold

et al., 1995).

4.4.1 Model Inputs

Land use data used in the SWAT model was derived from maps provided by European Commission Joint Research Center for Central Asia for the year 2000 (Tateishi et al., 2011). Soil map for the study area was obtained from the global digital soil map provided by Food and Agricultural Organization of the United Nations (FAO, 2003). A DEM at 90 m resolution is obtained from the Shuttle Radar Topography Mission (SRTM). This DEM is used to delineate the watershed. All meteorological inputs (i.e., temperature, wind, humidity, solar radiation) except precipitation were compiled from National Centers for Environmental Prediction (NCEP) and Climate Forecast System Reanalysis (CFSR; (Fuka et al., 2014); (Dile and Srinivasan, 2014).

Monthly streamflow data for multiple gauging stations located on Tigris River and its tributaries were obtained from the U.S. Geological Survey (USGS; (Saleh, 2010). A total of 10 stations were found reliable for use in calibration and validation of SWAT model. Table 4.1 summarizes the main characteristics of these gauging stations for which streamflow was evaluated. The selected gauge stations represent two climate regimes (semi-humid and semi-arid). The discharge data was examined and validated for missing data. If the flow rate was missing in any month, the mean flow rate of the two forward and two backward months was substituted for the missing month.

4.4.2 Precipitation Data

This section provides an overview of the major characteristics of the precipitation data sources considered in this study. Four grid-based daily precipitation data

Table 4.1: Streamflow gauging stations located in Tigris River Basin and used in this study.

River name and station location	Station ID	Latitude (degrees)	Longitude (degrees)	Drainage area (km^2)	Mean monthly discharge (m3s-1)
Tigris River at Mosul	TIGBSN1	36.63	42.82	54,900	460.83
Greater Zab River at Bakhem	TIGBSN2	36.64	44.5	383	382.78
Khazir River at Manquba	TIGBSN3	36.3	43.55	2,900	31.2
Greater Zab River at Eski-Kelek	TIGBSN4	36.27	43.65	20,500	425.53
Lesser Zab River at Doka	TIGBSN5	35.95	44.95	233	233.36
Adhiam River at Fatha	TIGBSN6	35.05	43.55	107,600	767.04
Tigris River Injana	TIGBSN7	34.5	44.52	9,840	33.14
Diyala River at Derbindi-Khan	TIGBSN8	35.13	45.75	17,800	154
Tigris River at Baghdad	TIGBSN9	33.41	44.34	134,000	479.2
Tigris River at Gharraf	TIGBSN10	32.53	45.79	150,964	208.45

derived from multiple sources (historical observations, radar, satellite, or a combination of the three) were used as input in SWAT model to simulate the observed monthly stream flow in the TRB for the period 1979−1997. In addition, we included one actual gauge-based precipitation dataset for the period 1957 to 1963 to provide a realistic range of model parameters and to account for model uncertainty due to changing precipitation inputs. The following subsections provide an overview of precipitation products used in this study:

Asian Precipitation Highly Resolved Observational Data Integration towards the Evaluation of Water Resources project (APHRODITE); (Yatagai et al., 2012). APHRODITE is a product from the Research Institute for Humanity and Nature (RIHN) and the Meteorological Research Institute of Japan Meteorological Agency (MRI/JMA). This precipitation data product is interpolated from rain gauges and available for continental Asia including Himalayas, Southeast Asia and mountainous areas of the Middle East for the period 1951−2007. This study uses the current version (V1101R1) of the data with a spatial resolution of 0.25^o that covers the entire TRB domain.

Multi-Source Weighted Ensemble Precipitation (MSWEP) is a recent global

daily precipitation dataset with 0.25^o grid spatial resolution and available for the period 1979−2015. MSWEP (Beck et al., 2017) combines data from satellite and both reanalysis and observed precipitation. The MSWEP data was further corrected for gauge-under catch and orographic errors by inferring catchment average precipitation from the streamflow data for 13762 stations globally.

The National Ocean and Atmospheric Administration (NOAA) Climate Prediction Center (CPC); (Xie et al., 2007) is based on the analysis of daily global precipitation data from multiple sources and available for the period 1979−2005 at 0.5^o grid resolution. The CPC data is developed to create a precipitation database by combining precipitation from radar, satellite and over 30,000 rain gauge stations data across the globe.

The Precipitation Estimation from Remotely Sensed Information using Artificial Neural Networks-Climate Data Record (PERSIANN-CDR); (Sorooshian et al., 2000); (Ashouri et al., 2015) provides multi-satellite, high resolution, daily estimations by combining geostationary and low orbital satellite imagery. This data set is available for the period 1983−2016 at a spatial resolution of 0.25^o in latitude band (60S−60N). The CDR version used in this work does not resolve the diurnal cycle and greatly depends on other estimations such as Global Precipitation Climatology Project (GPCP) and National Centers for Environmental Prediction (NCEP).

To consider the uncertainty in precipitation datasets and to provide more spatiotemporal representation in the precipitation over the entire river basin, the Actual daily gauge-based Precipitation Data (APD) was obtained from approximately 33 stations located in the TRB for the period 1957−1963 (the data is scarce and difficult to access). The continuity and the quality of this data source were examined; it was found that the daily data was not consistently documented for some gauge stations each month. Thus, the following steps were taken to generate APD gauge-based

data: 1) for each month, the original stations were remapped (re-gridded) to a new uniform mesh grid defined on 0.25^o longitude and latitude spatial resolution, 2) the precipitation at those new grid locations was evaluated using Kriging interpolation method. The Kriging technique is recommended for interpolating daily precipitation over deterministic methods (Ly et al., 2013). Although the APD data is interpolated, it still represents the actual rainfall quantity, intensity, and the number of days registered precipitation within the TRB.

4.5 Methodology

4.5.1 Model Setup and Calibration

ArcSWAT (2012) was used in this study. The delineation of the watershed and streams network was done based on the DEM (90 m resolution), which resulted into 99 sub-basins for the TRB (Figure 4.1c). The sub-basins were further divided into 5371 HRUs based on unique combinations of soil, land use, and slope. The Sequential Uncertainty Fitting-2 (SUFI-2), available in the SWAT-CUP package (Abbaspour et al., 2015) was used for model calibration. The SUFI-2 algorithm maps all model parameter uncertainties and express them as a range of uniform distributions that account for all sources of uncertainties in the hydrological model (Abbaspour et al., 2004). A set of 22 flow parameters along with their range was identified for this process to determine the most sensitive parameters. Initial parameter ranges were assigned from large-scale SWAT models developed for neighboring areas and from tabulated parameter values in SWAT manual (Faramarzi et al., 2009). A full list of these parameters along with their default range is shown in Table 4.2. The sensitivity of the selected parameters was found using a global sensitivity analysis tool known

as LH-Oah which combines Latin Hypercube sampling and One-Factor-At-A-Time sampling (Van Griensven et al., 2006).

In general, model parameters are usually sensitive with respect to change in the precipitation data source used in the hydrological model. Besides, different models forcing data could result in similar stream flow predictions after optimizing different parameters. Therefore, parameter sensitivity analysis of SWAT model for each of the fours PDS and APD was conducted by applying three approaches for selection of parameters as follows:

a. Cumulative Ranked Parameter Set (CRPS): The parameters obtained from SWAT model by forcing each of the PDS were ranked from 1 to 22 (with 1 being the most sensitive parameter). The mean of the four ranks from all PDS was determined to represent an overall cumulative rank (hereby called Cumulative Ranked Parameter Set or CRPS), shown in Table 4.3. Top eight most sensitive parameters were identified using this procedure and other 14 parameters were given default values. Final parameter ranges obtained from the CRPS approach assures comparing similar model parameters from estimated and observed precipitation. (Strauch et al., 2012) used a similar procedure for calibrating SWAT model using five precipitation data sets.

b. Gauge Ranked Parameter Set (GRPS): The eight most sensitive parameters from SWAT model run with actual gauge precipitation data were identified. Then, this set of parameters was used to calibrate SWAT model for streamflow for each of the PDS. This procedure is termed as Gauge Ranked Parameter Set (GRPS). This fixed parameter set procedure may have better representation for the hydrological conditions in the TRB and similar approach was earlier applied by (Jiang et al., 2012).

c. Individual Ranked Parameter Set (IRPS): SWAT model is calibrated in-

Table 4.2: List of parameters and their default ranges used for the SWAT model development.

Type[a]	Parameter	Description (units)	SWAT default range Max.	Min.
r__	CN2	SCSII Curve Number	-0.3	0.3
r__	SOL_AWC	Average available soil water content	-0.3	0.3
r__	ESCO	Soil evaporation compensation factor	-0.4	0.4
v__	EPCO	Plant uptake factor	0.01	1
r__	SURLAG	Surface runoff lag coefficient	-0.2	0.2
v__	CH_N2	Mannings n value for the main channel	0.04	0.14
v__	CH_K2	Effective soil hydraulic conductivity (mm/h)	5	150
r__	OV_N	Overland flow Mannings coefficient	-0.4	0.4
r__	ALPHA_BF	Base-flow recession factor (days)	-0.3	0.3
v__	GW_REVAP	Groundwater revap coefficient	0.02	0.2
v__	GW_DELAY	Groundwater delay time (days)	0	500
v__	GWQMN	Threshold water depth in shallow aquifer requires for return flow to occur	0	5000
r__	SOL_K	Saturated hydraulic conductivity (mm/day)	-0.3	0.3
r__	REVAPMN	Threshold water depth in shallow aquifer requires for revap to occur	-0.3	0.3
r__	RCHRG_DP	Deep aquifer percolation fraction	-0.3	0.3
v__	SFTMP	Mean temperature of snow melt (oC)	-5	5
v__	SMTMP	Snow melt base temperature (oC)	-5	5
v__	SMFMX	Maximum melt factor (mm H2O/oC-day)	1.7	6.5
v__	SMFMN	Minimum melt factor (mm H2O/oC-day)	1.4	4.5
v__	TIMP	Snow pack temperature lag factor	0.01	1
v__	SNOCOVMX	Minimum snow water content corresponds to 100% snow cover (mm H2O)	0	1
v__	SNO50COV	Fraction of snow volume represented by SNOCOVMX corresponds to 50% snow cover	0.01	0.99

[a] v__: means the default parameter is replaced by a given value, and r__ means the existing parameter value is multiplied by (1+the given value).

Table 4.3: Rank of most sensitive model parameters resulted from sensitivity analysis for four precipitation products.

Parameter	MDL_{APH}	MDL_{MSW}	MDL_{CPC}	MDL_{PER}	Average
SOL_AWC	2	1	4	2	2.25
CH_K2	1	2	14	1	4.5
SFTMP	3	5	2	4	3.5
OV_N	11	13	1	8	8.25
CN2	4	22	7	5	9.5
GW_REVAP	6	8	5	10	7.25
EPCO	22	3	19	3	11.75
ALPHA_BF	10	11	16	14	12.75

dividually with each of the PDS and labeled as Individual Ranked Parameter Set (IRPS). The IRPS allows selecting the 8 most sensitive parameters for each PDS independently in model calibration and validation. This method is different from CRPS because it allows SWAT model with each PDS to be calibrated independently (i.e., four parameter sets are identified in this process, one for each PDS).

4.5.2 Model Uncertainty and Performance Measures

In SUFI-2, the propagation of uncertainties in hydrologic model parameters leads to uncertainties in model output variables. These are usually expressed as probabilistic predictions calculated at 2.5% and 97.5% levels of the cumulative distribution of the output variables, which is also known as 95% Prediction Probability Uncertainty (95PPU); (Abbaspour et al., 2015). Two statistical based factors, known as p-factor and r-factor, are commonly used to quantify uncertainties in simulated results (expressed as lower and upper bands of the 95PPU). The p-factor (>70% is acceptable value) is the percentage of the observed data bounded by upper and lower model outputs, while r-factor (around 1 is acceptable value) is the thickness of that band (Abbaspour et al., 2007). The r-factor is given by Eq.(4.2). Where the term

$y_{t,97.5\%} - y_{t,25\%}$ includes the upper and the lower bounds of 95PPU at time t, and σ_{obs} is the standard deviation of the observed data sample.

$$r - factor = \frac{\frac{1}{n}\sum_{t}^{n}(y_{t,97.5\%} - y_{t,25\%})}{\sigma_{obs}} \tag{4.2}$$

Model streamflow outputs are evaluated using multiple statistical criteria including Correlation Coefficient (CC), Root Mean Square Error (RMSE), Percent BAIS (PBIAS), and Nash-Sutcliffe Efficiency coefficient (NSE). The calculation procedure for CC, RMSE, PBIAS, and NSE are given in Eq.(4.3) to Eq.(4.6) respectively. The O_i represents the observed variable and P_i is the simulated variable at a time step i. The $\bar{P}$ and $\bar{O}$ denote the average simulated and observed values of the same variable, respectively.

$$CC = \frac{\left[\sum_{i=1}^{n}(P_i - \bar{P})(O_i - \bar{O})\right]^2}{\sum_{i=1}^{n}(P_i - \bar{P})^2 \sum_{i=1}^{n}(O_i - \bar{O})^2} \tag{4.3}$$

$$RMSE = \sqrt{\frac{1}{n}\sum_{i=12}^{n}(P_i - O_i)^2} \tag{4.4}$$

$$PBIAS = \frac{\sum_{i=1}^{n}(P_i - O_i)}{\sum_{i=1}^{n} O_i} \tag{4.5}$$

$$NSE = 1 - \frac{\sum_{i=1}^{n}(P_i - \bar{P})}{\sum_{i=1}^{n}(O_i - \bar{O})} \tag{4.6}$$

4.6 Results

4.6.1 Spatiotemporal Distribution of Precipitation

The spatiotemporal variation of long term precipitation climatology from the four PDS (APHRODITE, MSWEP, CPC, and PERSIANN-CDR) is compared with the actual precipitation represented by APD data. As described earlier, all PDS are available for the period (1979−1997), except PERSIANN-CDR data for the period (1983-1997), while the APD precipitation data set is available for the period 1953−1963. The long-term mean annual precipitation climatology averaged across the TRB varies significantly among the datasets ranging from 242.87 mm/year for CPC to 503.55 mm/year for MSWEP compared to the reference dataset APD 364.156 mm/year. This indicates that MSWEP data overestimates (+38%) the actual annual precipitation, whereas the CPC data underestimates the actual precipitation as it gives the minimum estimate with -33% relative errors. PERSIANN-CDR precipitation derived from satellite data performed quite well in estimating annual precipitation with amount of 361.56 mm/year (-0.7% relative error), followed by APHRODITE with 295 mm/year (-19% relative error).

The temporal variations of mean monthly precipitation data average over the TRB for all PDS and APD are compared (Figure 4.2). In Figure 4.2a, the comparison between all PDS the APD data clearly shows that CPC underestimates mean monthly precipitation during wet months (November-April) while MSWEP overestimates during the same period. The dry season mean monthly precipitations (May to October) is overestimated by all PDS. However, all PDS were relatively able to capture rainfall signal (rain/no rain) appropriately because of that wet and dry seasons are clearly distinguished as in Figure 4.2a. The empirical cumulative probability functions for monthly precipitation estimations for PDS and APD are shown in Figure 4.2b. It was

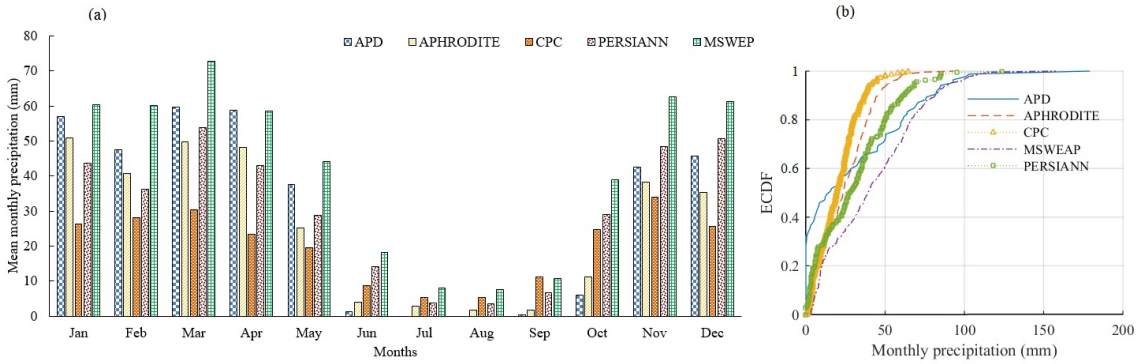

Figure 4.2: (a) Mean monthly precipitation over Tigris River Basin based on APD (1957-1963); APHRODITE, MSWEAP, and CPC (1979-1997); and PERSIANN-CDR (1983-1997), (b) Empirical cumulative probability function (ECDF) for monthly precipitation data.

observed that at any given probability, the PDS either over (under) predicts APD. Mostly MSWEP product is higher than other PDS, whereas for other products over (under) estimates are observed beyond a threshold.

The spatial distribution (using Kriging interpolation) of the long-term annual precipitation estimated from each dataset is provided in Figure 4.3 for the TRB. This figure shows that the spatial distribution of precipitation from APHRODITE and MSWEP (Figure 4.3b and c) data have a good agreement with APD data (Figure 4.3a). All PDS registered higher annual precipitation in northern and northeastern parts of the river basin than the southern and southwestern parts, which agrees with APD data albeit different magnitudes. The precipitation gradient (the rate of change in precipitation with distance) was not well represented by the PERSIANN-CDR and CPC data (Figure 4.3e and f) compared to the other data sets that indicates a clear pattern in annual precipitation (higher gradients at the northern than the southern parts of the TRB).

Quantitative statistics such as Correlation Coefficient, Percent Bias, and Root Mean Square Error are calculated for daily mean precipitation estimates (using annual

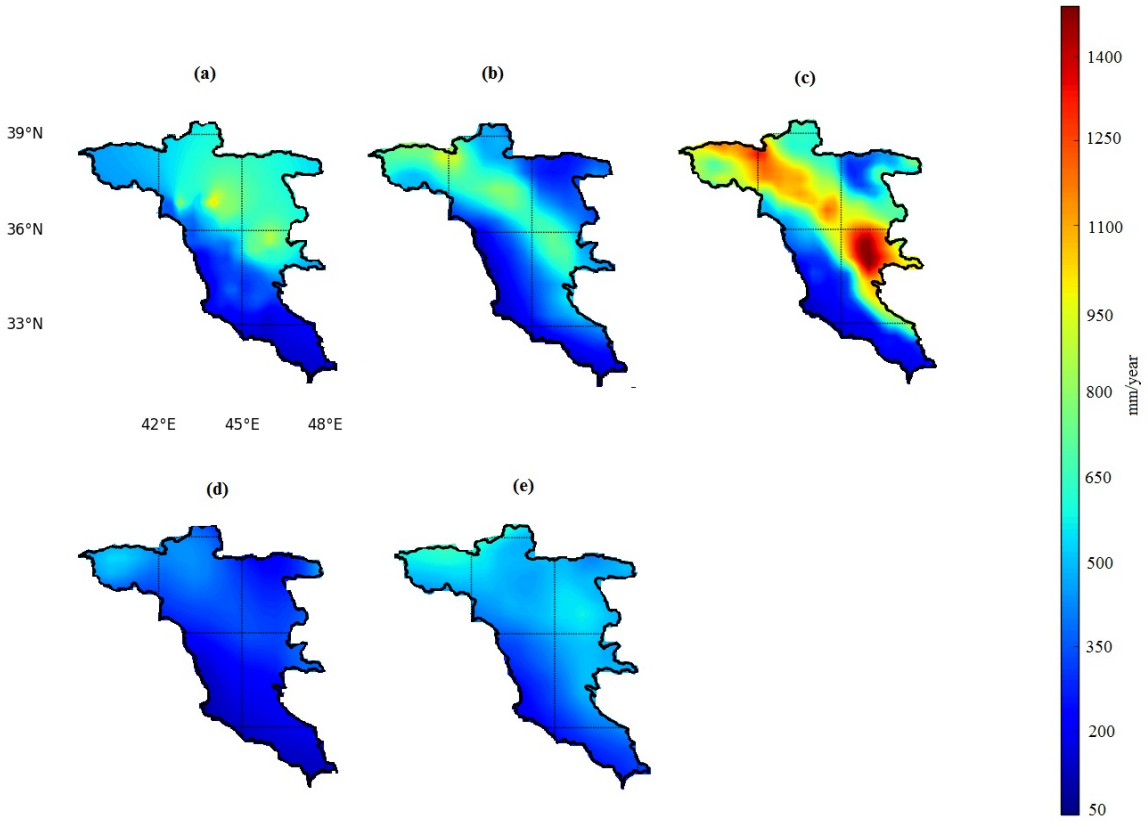

Figure 4.3: Long-term mean annual precipitation for Tigris River Basin derived from (a) APD, (b) APHRODITE, (c) MSWEP, (d) CPC, and (e) PERSIANN-CDR data.

cycle averaged over the TRB) for PDS versus APD and presented in Table 4.4. It was observed that APHRODITE, CPC, and PERSIANN-CDR have a positive percentage bias (PBIAS), which indicates that these products mostly underestimate the daily precipitation in the TRB (Table 4.4). However, MSWEP shows the opposite behavior in the study area with negative PBIAS of -38.2%. Based on our observations, most PDS estimates registered about 30% more rainy days than gauge data APD during the dry season of the year, yet with less estimates of extreme precipitation (wet season) which possibly led to the data underestimation. The table also demonstrates that APHRODITE provides the best estimates for actual rain gauge data with the highest correlation coefficient (0.65), and lowest RMSE (0.62) and PBIAS (19.1), followed by PERSIANN-CDR, MSWEAP, and CPC, respectively.

Table 4.4: Quantitative Statistics (CC, RMSE, and PBIAS) for area-averaged daily mean annual cycle precipitation from PDS and APD in Tigris River Basin.

Precipitation data set	CC	RMSE (mm)	PBIAS (%)
APHRODITE	0.65	0.62	19.1
MSWEAP	0.55	0.92	-38.2
CPC	0.44	0.99	33.3
PERSIANN-CDR	0.55	0.92	0.6

4.6.2 SWAT Model Parameters Uncertainty

Five sets of precipitation products APHRODITE (APH), MSWEP (MSW), CPC, PERSIANN-CDR (PER) and Actual Precipitation Data (APD) are used as inputs to SWAT and the corresponding modeled streamflow outputs are represented by MDL_{APH}, MDL_{MSW}, MDL_{CPC}, MDL_{PER}, and MDL_{APD}. The best-fit and the final ranges of the parameters resulted from the calibrated SWAT models for the four PDS (using CRPS) and APD (using GPRS) approaches are compared in Figure 4.4. This figure clearly indicates that changing precipitation inputs in the SWAT model

produces different sets of parameter uncertainties. Comparing parameter ranges of four models (MDL_{APH}, MDL_{MSW}, MDL_{CPC}, and $MDLPER$) with MDL_{APD} (the leftmost bars) reveals that parameter range for MDL_{APD} tends to have the least uncertainty (lowest variations). Likewise, MDL_{APH} shows comparatively lower parameter uncertainty compared to the other three models, namely MDL_{MSW}, MDL_{PER}, and MDL_{CPC}. For MDL_{CPC} model, the fitted parameter of SOL_AWC is lowered, which allows producing more runoff as this precipitation product underestimated the APD data, while the SOL_AWC value in MDL_{MSW} is higher allowing for less runoff as this precipitation overestimated the APD data (Figure 4.4).

Most of the rainfall occurs in the northern part of the TRB (where the snowfall is dominant); therefore the snow melt temperature parameter (SFTMP) seems to be more significant in all models calibrated with PDS. The range of SFTMP value uniformly varies between models with a range of -1 to 2^oC, which is consistent with other studies in similar climate regions, e.g., Iran, (Rostamian et al., 2008). The best fit of CH_K2 value (hydraulic conductivity for alluvial main channel) indicates that the main channels in the TRB are covered mainly with clean sand and gravel (CH_K2>100 mm/hr) to silty sand with gravel (CH_K2>50 mm/hr). Considering the shallow aquifers (100−200 m deep) in the study area, which mainly consists of sandstone, limestone, silty soils with a transmissivity ranging from 200 to 560 m^2/day (Jassim and Goff, 2006), the CH_K2 values used are reasonable. Overall, the parameter ranges and best fit values vary by changing the precipitation data source in SWAT model, which may need extra attention when considering only one model input; as the issue of parameterization is an important task in hydrological model development. This reinforces the idea of using multiple parameter sets including the one derived from the actual precipitation model to validate the other precipitation models with a large number of simulations (>500 simulations), given that SUFI-2 parameter range

width is highly affected by the number of simulations and consequently the simulated streamflow.

4.6.3 Evaluation of Precipitation Products for Streamflow Simulation

The performance of four PDS was evaluated for streamflow simulation in SWAT model calibrated using parameters obtained from CRPS for PDS and from GRPS for ADP. The simulated streamflow with each PDS is compared with the actual observations using quantitative statistics (CC, NSE, and PBIAS), as shown in Table 4.5. The precipitation product is considered performing well if the goodness of fit measures for streamflow stations satisfy the following thresholds; CC>0.65, NSE>0.50, and |PBIAS| <25% (Moriasi et al., 2007; Duda et al., 2012). Based on these model performance measures, half of the streamflow simulated in MDL_{APD}, driven by actual precipitation data (i.e., APD) satisfied the goodness of fit performance criteria. This seems to emphasize the significance of using point-based precipitation data in representing the spatiotemporal variability even in relatively large-scale watersheds, such as the TRB. Satisfying the goodness of fit criteria by only half of the stations also shows the complexity of the relationship between the daily rainfall and the generated streamflow. For all other precipitation sources (products), the goodness of fit performance indicators is relatively higher during calibration than validation period. The best individual streamflow prediction among all PDS was obtained from MDL_{APH}, which suggests that APHRODITE performed better in hydrological modeling compared to other gauged-based global precipitation products (i.e., CPC and MSWEP), especially in areas that witness high precipitation variability and lack of data (Table 4.5). The possible reason maybe because of the dense gauge repre-

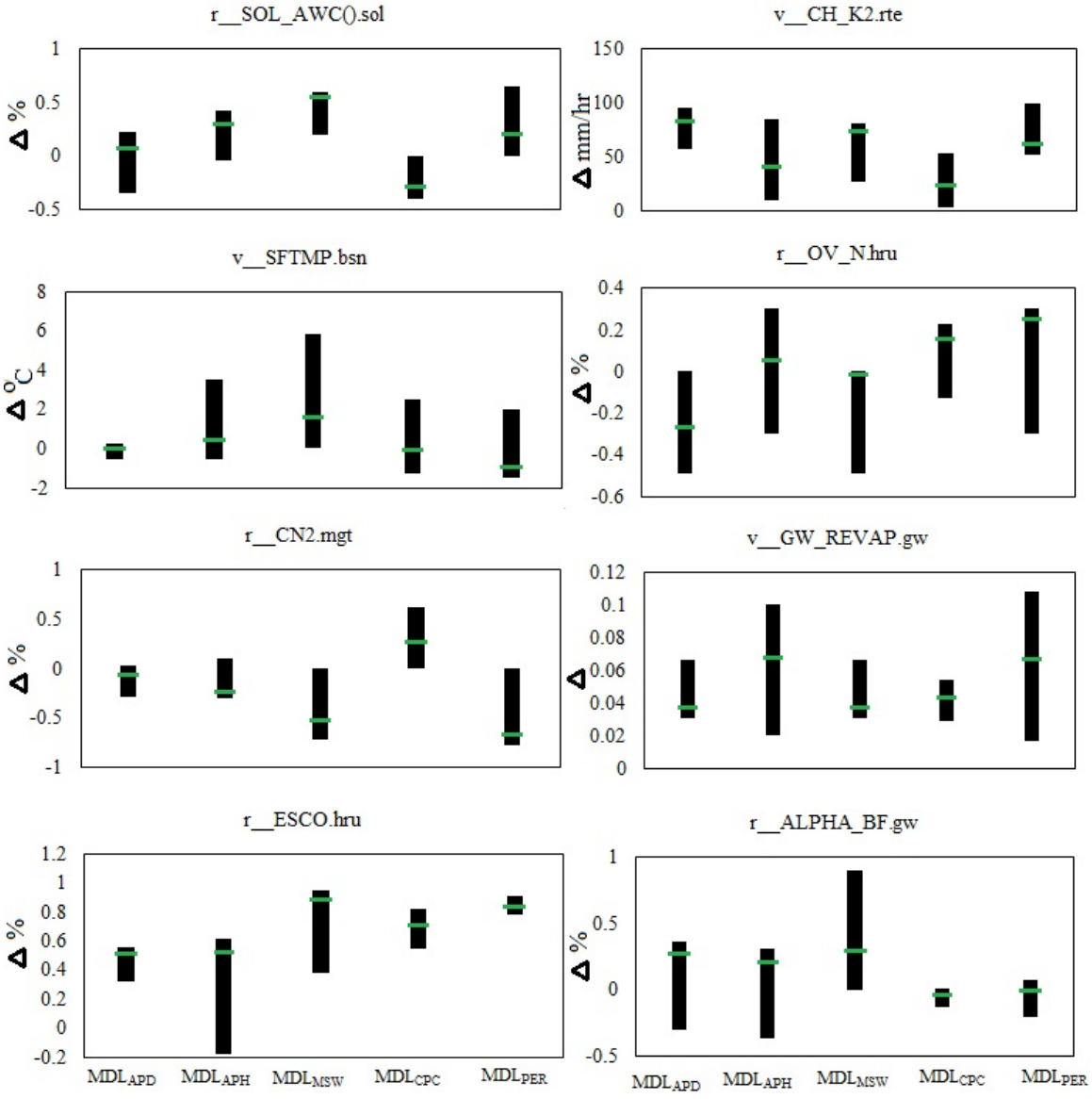

Figure 4.4: Calibrated model parameter range (black rectangles) and best-fit parameter values (green lines) for SWAT model derived based on five precipitation products. MDL_{APD} is calibrated using GRPS while the other four models are calibrated based on CRPS approaches. Δ represents the range of parameters. [Note: The five sets of precipitation products are used as inputs to SWAT and the corresponding modeled streamflow outputs are represented by MDL_{APH}, MDL_{MSW}, MDL_{CPC}, MDL_{PER}, and MDL_{APD}].

sentation in case of APHRODITE over the global grid-based precipitation data. In addition, Global precipitation data are often available on coarser grid scale which may misrepresent the spatial variability information in precipitation data.

Among all the PDS, MDL_{CPC} performed poorly for most of the streamflow stations during calibration and validation periods, even though it is compiled from an observed data. Part of this poor performance could be because the CPC precipitation data is given on coarser mesh grid data points than all other PDS (0.5^o compared 0.25^o longitude x latitude). This is consistent with the precipitation comparison results obtained in the previous section. The poor correlation between simulated and observed precipitation as well as streamflow simulation using CPC brings into question the credibility of this precipitation product in the hydrologic simulation and that further process might be required to enhance the spatiotemporal representation for the simulated streamflow data (e.g., downscaling). In contrast, PERSIANN-CDR data performed relatively good based on only NSE and PBIAS criteria. Given that PERSIANN-CDR is a satellite data and available for areas with limited data measurements, it can be considered invaluable for hydrological modeling in the TRB. These findings are in accordance with the results of (Behrangi et al., 2011); (Sidike et al., 2016); (Zhu et al., 2016), where the PERSIANN-CDR data showed potentially encouraging results in simulating monthly streamflow data when evaluated against actual point based precipitation data.

The monthly streamflow simulated by all PDS for the period $1983-1997$ (consistent for all models) is presented in Figure 4.5. This analysis was carried out based on the SWAT-CUP best fit streamflow outputs at four discharge stations, out of which two stations (TIGBSN4 and TIGBSN7) are located on the main Tigris River and the other two on its tributaries (TIGBSN1 and TIGBSN6). These stations represent different flow conditions and climate zones in the watershed. It can be no-

Table 4.5: Correlation metrics based on CC, NS, and PBIAS calculated based on observed streamflow and SWAT based flows obtained from different precipitation data sources. Each cell has two values representing calibration/validation respectively.

Outlet	MDL_{APD}			$MDLAPH$			MDL_{CPC}			MDL_{MSW}			MDL_{PER}		
	CC	NS	PBIAS	CC	NS	PBIAS	CC	NS	PBIAS	CC	NS	PBIAS	CC	NS	PBIAS
TIGBSN1	**0.73/0.63**	**0.71/0.67**	**-18.87/-16.98**	0.60/0.58	0.65/0.63	11.19/10.85	0.53/0.51	**0.65/0.64**	**11.19/10.74**	0.53/0.51	0.65/0.64	-11.19/-10.74	0.46/0.44	**0.69/0.67**	**11.97/11.49**
TIGBSN2	0.52/0.42	0.61/0.58	3.1/2.79	0.62/0.6	0.62/0.6	-5.47/-5.25	0.51/0.48	0.47/0.45	0.73/0.7	0.62/0.59	0.47/0.45	-55.04/-52.84	0.6/0.57	**0.70/0.67**	**10.43/10.02**
TIGBSN3	**0.68/0.58**	**0.69/0.65**	**1.112**	**0.68/0.65**	**0.69/0.67**	**-4.17/-4.03**	0.57/0.55	0.35/0.33	19.77/19.11	0.53/0.52	0.72/0.7	-23.9/-23.11	0.12/0.11	0.32/0.3	14.87/14.38
TIGBSN4	**0.87/0.77**	**0.98/0.93**	**6.3/5.67**	**0.74/0.72**	**0.72/0.7**	**7.17/6.97**	0.42/0.4	0.24/0.23	23.3/22.65	**0.96/0.94**	**0.99/0.96**	**1.027950311**	0.61/0.59	**0.91/0.88**	**23.7/23.04**
TIGBSN5	0.52/0.42	0.61/0.58	-2.17/-1.95	0.59/0.54	0.8/0.74	6.37/5.84	0.63/0.57	0.32/0.29	1.27/1.16	0.57/0.52	0.53/0.49	1.090444231	0.48/0.44	0.43/0.39	1.090750436
TIGBSN6	0.53/0.43	0.62/0.59	-10.03/-9.03	**0.78/0.74**	**0.98/0.92**	**-7.57/-7.14**	0.43/0.4	0.12/0.11	25.4/23.95	0.53/0.5	0.6/0.57	-10.03/-9.46	0.35/0.33	0.49/0.46	10.93/10.31
TIGBSN7	**0.95/0.85**	**0.86/0.82**	**0.2/0.18**	**0.95/0.88**	**0.86/0.8**	**0.2/0.19**	0.89/0.83	0.26/0.25	3.33/3.1	**0.9/0.83**	**0.82/0.76**	**1.052631579**	0.47/0.44	**0.74/0.68**	**5.37/4.99**
TIGBSN8	0.5/0.4	0.75/0.72	-26.57/-23.91	0.48/0.44	0.7/0.64	-26.57/-24.44	0.48/0.44	**0.7/0.64**	**26.57/24.44**	0.48/0.44	0.7/0.64	-26.57/-24.44	0.48/0.44	**0.70/0.64**	**-26.57/-24.44**
TIGBSN9	0.42/0.32	0.6/0.57	-20.6/-18.54	0.42/0.39	0.6/0.57	-20.6/-19.36	0.43/0.4	**0.64/0.6**	**20.47/19.24**	0.48/0.45	0.53/0.49	-19.5/-18.33	0.48/0.45	0.53/0.49	-19.5/-18.33
TIGBSN10	**0.62/0.52**	**0.69/0.66**	**-23.9/-21.51**	0.43/0.41	0.63/0.6	-14.84/-14.25	0.43/0.41	**0.62/0.61**	**19.23/18.46**	0.43/0.41	0.38/0.36	-19.26/-18.49	0.17/0.16	**0.66/0.64**	**-24.02/-23.06**

ticed that the flow in these stations is governed by the snow melt, which is evident from high flows (regular peaks) in spring months (March−May) while low flows in dry months (May-October). Overall, this figure shows that individual precipitation product based streamflow outputs have significant variations in simulating the actual streamflow, particularly the peak flow in the TRB during this period. Except for MDL_{MSW} (where the peak flow and the base flow are over predicted), the base flow in all models was mostly over-predicted, while the peak flow was under-predicted during calibration and validation periods as indicated by the time series (Figure 4.5). However, the performance of all the models was relatively higher in capturing base flow, especially in the calibration period. This is most likely due to two main reasons; most precipitation products have failed to reproduce extreme events with higher accuracy, and the complexity of the branching system of the main Tigris River before the station locations which made the river routing process more difficult. APHRODITE based streamflow (i.e., MDL_{APH}) in both calibration and validation periods comparatively match well with the observed streamflow, where the model follows similar patterns of the peaks and the low flows for all stations (Figure 4.5).

As before, MDL_{APH} driven by APHRODITE precipitation data source performed relatively better than MDL_{CPC}, MDL_{MSW}, and MDL_{PER} in terms of CC, NSE, and PBIAS during both calibration and validation periods. Even though PERSIANN-CDR precipitation dataset under-predicted the stream flow in the TRB, it is performed satisfactorily in matching the actual stream flow at some stations (e.g., TIGBSN1 and TIGBSN7). CPC precipitation dataset did not perform well as stated before. These results are consistent with the findings of (Vu et al., 2012); (Yang et al., 2015). As expected, the performance of all individual models is slightly higher in calibration than validation period. This is quite likely due to the significant increase in irrigation and drinking water demands in the TRB for later years of simulations (i.e.,

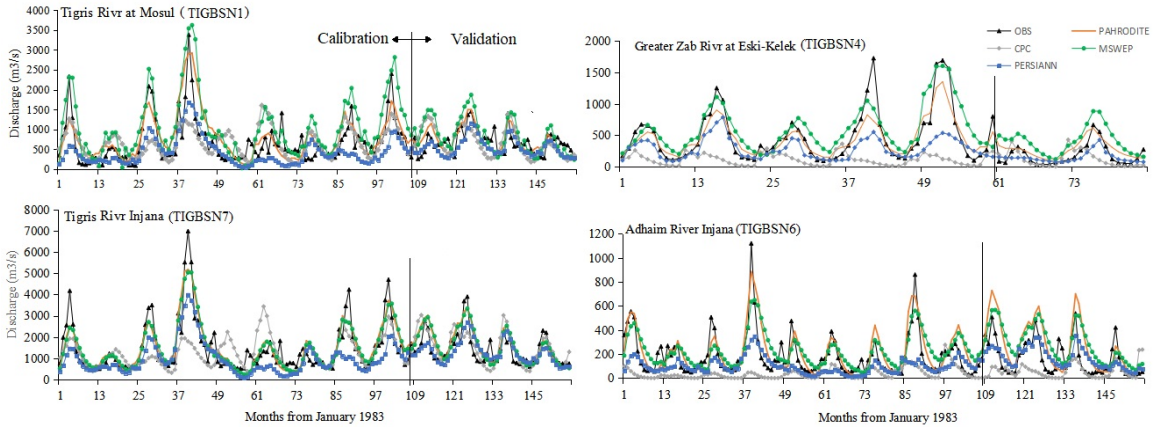

Figure 4.5: Simulated monthly streamflow for four gauging stations estimated from SWAT model with different PDS. TIGBSN4 and TIGBSN7 stations are located on the main Tigris River, while TIGBSN1 and TIGBSN6 stations are located on its tributaries.

during validation period) (Tigrek and Kibaroglu, 2011); (Issa et al., 2014).

4.6.4 Model Streamflow Predictive Uncertainties

Parameter uncertainty in hydrological model is likely to contribute randomness to modeled streamflow outputs (Abbaspour et al., 2015). Predictive uncertainties in modeled streamflow outputs are compared between the four PDS calibrated using the three approaches (CRPS, GRPS, and IRPS). The model is considered to perform well if more than 70% of the observed streamflow was captured by the simulation (i.e., p-factor >70%) and with smaller 95PPU uncertainty envelope (i.e., r−factor of about 1).

Simulation uncertainty represented by both the p- and r-factors was evaluated for each precipitation product calibrated using CRPS, GRPS, and IRPS approaches and presented in Figure 4.6. The values of these two factors are presented by using four groups of box plots. Each group represents a model calibrated using CRPS,

GRPS, and IPRS. Three pairs of boxes are presented in each group. For each pair, the first box plot represents calibration and the second box plot is for validation. For all three approaches, p-factor and r-factor values are higher during calibration than validation period. The p- and r- factors from IRPS and GRPS approaches scored higher values than the CRPS. The highest values for p- and r-factors are observed for MDL_{APH} and MDL_{MSW} (with a relative percentage increase of under 8% in both p- and r-factors for GRPS), which means that these two calibration approaches have less predictive uncertainties in simulating streamflow. The relative improvements in SWAT model simulations calibrated with GRPS over IRPS is likely due to the higher/lower curve number values used in SWAT model than the standard tabulated ranges. The higher accuracy in streamflow estimations for the case of GRPS came on the expense of the calibrated parameter ranges. This exercise of not using the standard tabulated parameter values was also mentioned by (Bitew et al., 2012), which could cause substantial errors to the simulated streamflow, if it is not closely monitored. All stations based on MDL_{APH} witnessed the lowest uncertainty, while MDL_{CPC} shows the highest predicted uncertainty, which makes this precipitation data sources least desirable for prediction streamflow data in TRB. Some gauge stations based on MDL_{MSW} and MDL_{PER} reached desirable uncertainties in calibration and validation periods.

Finally, a comparison between simulated streamflow using the CRPS and IRPS approaches and the actual streamflow is illustrated in Figures (4.7 and 4.8). In these two figures, predictive uncertainty is represented for a sample of two stations (TIGBSN2 and TIGBSN3) located in the highlands and lowlands of the TRB respectively. By comparing the 95PPU of models from CRPS and IRPS (left and right panels respectively), the IRPS shows less predictive uncertainty than the CRPS approach (i.e., better streamflow simulations). In addition, the uncertainty bandwidth was relatively

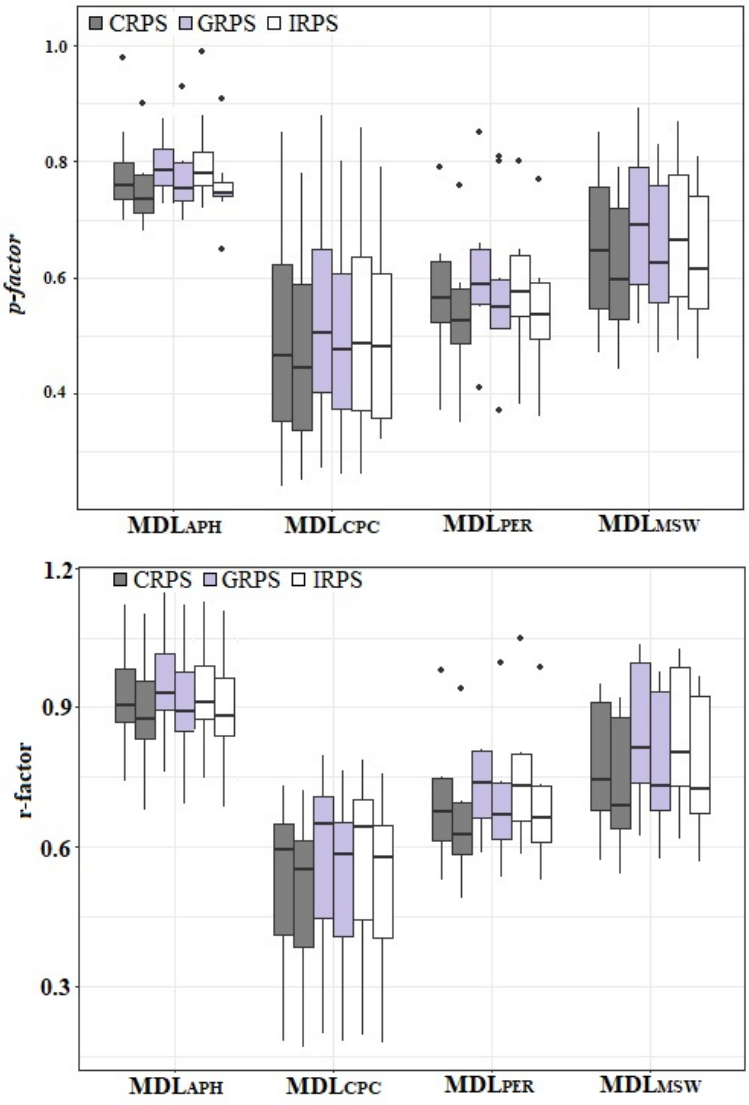

Figure 4.6: p- and r-factors from SWAT models (shown as groups) calibrated with CRPS, GRPS, and IRPS methods. Each group represents a model calibrated using three approaches. Three pairs of boxes in each group are presented with the first box being for calibration and the second box for validation in each pair.

narrower during low flow conditions than high flows. MDL_{APH} model (Figures 4.7a and 4.8a) witnessed consistently the lowest uncertainty compared to the other three data sources. The other three modeled streamflow outputs (MDL_{CPC}, MDL_{MSE}, and MDL_{PER}) were unable to capture the extreme streamflow accurately for the entire time series. However, MDL_{PER} showed reduced uncertainty at some stations when the IPRS calibration approach is used (compare Figures 4.7d and 4.8d). Overall, PERSIANN-CDR precipitation data a possible source for evaluating monthly streamflow in the TRB.

Different precipitation inputs generate distinct prediction uncertainties in modeling streamflow. The results are heterogeneous and it is not possible to generalize the outcomes obtained in one sub-catchment to another, i.e., the prediction uncertainty of each precipitation product is basin-specific. These variations of simulated streamflow uncertainties in response to different input precipitations could be attributed to the different interpolation techniques and merging algorithms that were implemented to compile these precipitation datasets (Tuo et al., 2016). Failing to capture extreme streamflow might be due to the relatively large number of iterations needed by SUFI-2, which is usually utilized in calibrating models (Strauch et al., 2012).

4.7 Conclusion

This study investigates the spatiotemporal variations of four precipitation data sources and analyzes their performance on simulating streamflow for the Tigris River Basin where the ground-based precipitation observations are scarce. Precipitation data sources consist of APHRODITE, CPC, MSWEP, and PERSIANN-CDR. The long-term precipitation estimates from these data sources are compared with the actual gauged precipitation data available for 33 stations for the study area. The

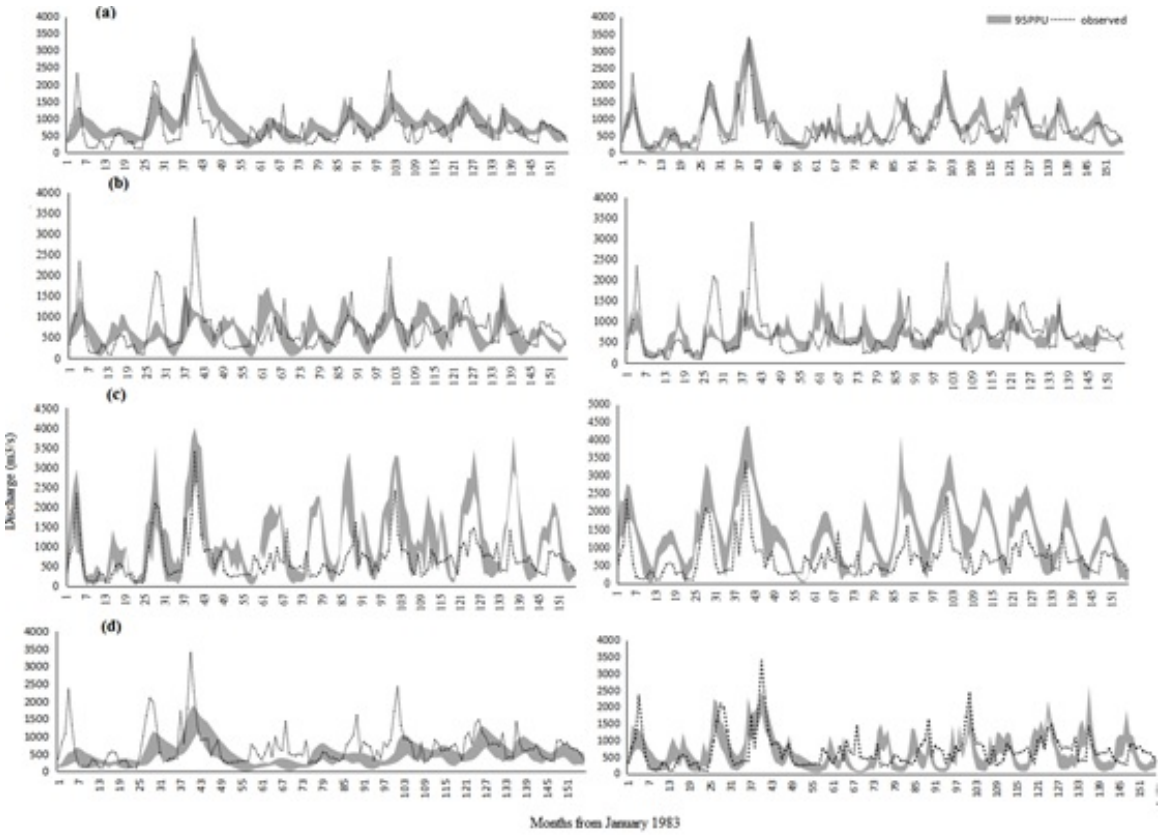

Figure 4.7: Illustration of 95PPU intervals obtained from SUFI-2 for CRPS and IRPS approaches. Model results are presented for TIGBSN2 streamflow station. The left side panel represents simulation results for CRPS calibration approach, while the right column is simulation results obtained based on IRPS approach. Rows are arranged as follows (a) APHRODITE, (b) CPC, (c) MSWEP, and (d) PERSIANN-CDR.

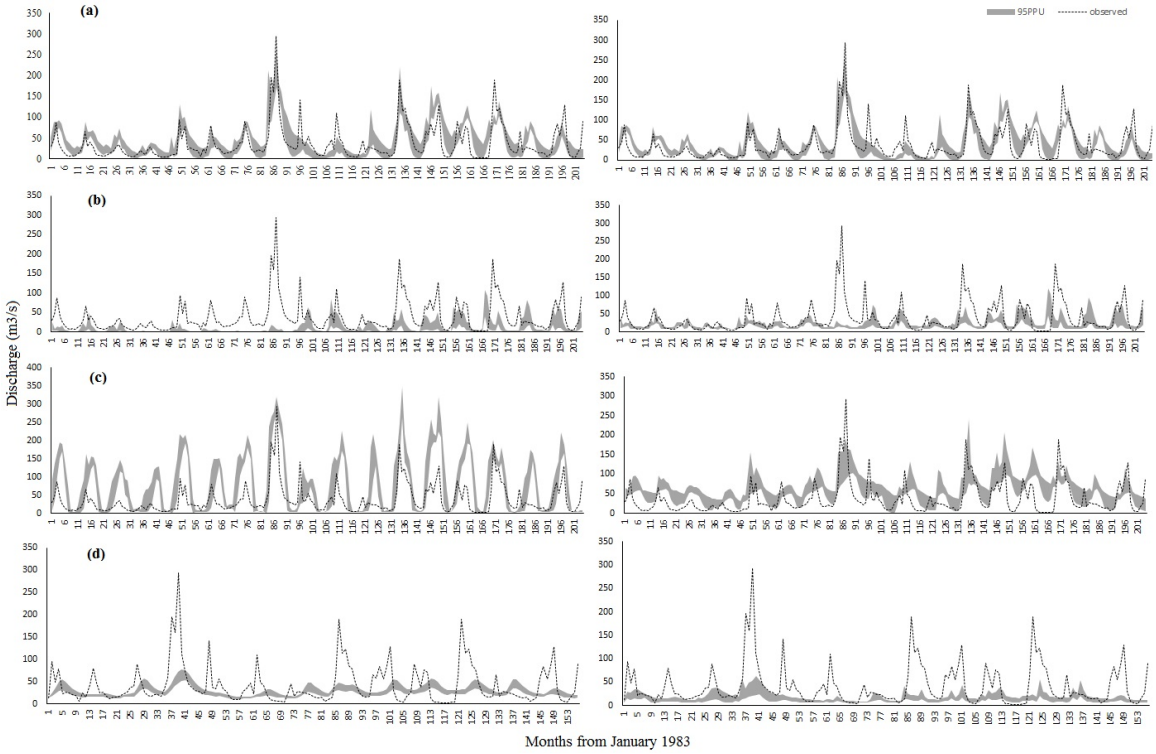

Figure 4.8: Illustration of 95% uncertainty intervals obtained from SUFI-2 for CRPS and IRPS approaches. Models result are presented for TIGBSN3 streamflow station. The left side column represents simulation results for CRPS approach, while the right column is simulation results obtained based on IRPS approach. Rows are arranged as follows (a) represents APHRODITE, (b) CPC, (c) MSWEP, and (d) PERSIANN-CDR.

following conclusions are drawn from this study:

a. All four precipitation data sources have produced different biases when evaluated against actual rain gauges. APHRODITE precipitation data showed the best acceptable spatiotemporal variations over Tigris River Basin. MSWEP data, on the other hand, overestimated the actual gauge precipitation data, while CPC underestimated the actual precipitation data. PERSIANN-CDR satellite-based precipitation data showed a satisfactory comparison with observed precipitation data.

b. Monthly streamflow estimated by SWAT model significantly improved using observed rainfall information in comparison to selected precipitation data sources because of the biases associated with each data source. Among the precipitation data sources, APHRODITE (interpolated from dense number of gauges per grid) exhibited the best skills in representing the streamflow, while PERSIAN-CDR (satellite data) showed satisfactory performance at few locations in the Tigris River Basin. Thus, it can be considered as a favorable product for Tigris River Basin in case of scarce precipitation records.

c. Predicted uncertainties in streamflow simulations vary when different parameter sets used in SWAT model. Therefore, multiple calibration approaches may be utilized to identify better model parameter sets. SWAT model calibrated individually with each precipitation data source showed the best calibration practice because it produced the least predictive uncertainties with realistic parameter range representations.

d. The streamflow estimated for Tigris River Basin using different forcing precipitations are heterogeneous and it is not straightforward to generalize the

outcomes obtained in one catchment to another, which also means the prediction uncertainty of each precipitation product is basin-specific (i.e., the findings are only applied for the Tigris River Basin).

Chapter 5

The State of Regional Surface and Groundwater Resources Assessment in Tigris and Euphrates River Basin Using Fully Coupled SWAT-MODFLOW Model

5.1 Abstract

Understanding the surface water and groundwater interactions in large river basins are important, nowadays, for decision makers to coup with the increasing risk of freshwater scarcity and to manage a sustainable water resources. Therefore, this study investigates regional surface and ground waters spatiotemporal interactions

for the Tigris and Euphrates River Basin (TERB, 900,000 km^2), located mostly in a semi-arid climate. These interactions were modeled using an integrated SWAT-MODFLOW hydrological model. The coupled SWAT-MODFLOW model outputs were calibrated against stream flow and groundwater levels during the period 1981-1997. The SWAT and MODFLOW models were first calibrated independently and then comprehensively (after coupling) using an integrated calibration approach implemented by expanding the use of SUFI-2 (a surface water calibration algorithmic) to account for the ground water component. For the step-wise calibration procedure followed, coupled model outputs were spatially validated against monthly stream flow, baseflow, and groundwater elevations collected at some locations with actual observations in the TERB. As an additional calibration approach, the total water storage anomalies obtained from the Gravity Recovery and Climate Experiment (GRACE) satellite data was compared to their corresponding simulations from the hydrological model during the period 2002-2013. The streamflow results simulated in coupled model showed better base flow representation than only using SWAT model with an overall of 15% increase in goodness of fit measures. Discharges between streams and aquifers are simulated on daily and monthly time steps at each streamflow grid point from MODFLOW. Groundwater discharge also displayed high spatial variability, with almost all locations showing loss from streamflow discharge to aquifers. Average annual groundwater discharge from streams is estimated to be -7,078,872 m^3y^{-1}, with a remarkable increase in groundwater discharge after January 1987. The infiltration rates from model showed higher rates northern parts of the watershed especially in permeable sedimentary (the foothills to alluvial sediments central and northeastern regions of watershed). The model findings can be useful in watershed management, and it can be extended to locate the potential locations of heavy nutrient mass fluxes, groundwater pumping from aquifers. .

5.2 Introduction

With the increase of water scarcity in many regions worldwide, the stress on water resources imposes negative impacts on the state of both surface water and groundwater systems (Lipper et al., 2007). Consequently, the decision makers need an adequate information on these two interacted resources to better manage a sustainable water resources (Rassam et al., 2013). Modeling the interactions of the surface and subsurface water is often challenging because of the nonlinear flow relationship between these two systems which can be further altered by irrigation activates, diversion of surface water, ground water pumping from aquifers (McCallum et al., 2013; Siebert et al., 2010). This requires developing more complex hydrodynamic algorithms to represent these hydrologic processes (Sulis et al., 2010). Therefore, several fully-integrated physical-based hydrological models were used to address these integrated interactions on different scales (e.g., regional and local) considering water and solute transport on surface and subsurface flows (Sophocleous et al., 1999; Sudicky et al., 2003). The two-dimensional surface water flow component which requires to solve the diffusion-wave and Manning's equations is often coupled with the subsurface flow component from Richard's and Darcy's equations (Galbiati et al., 2006; Harbaugh et al., 2000; Wible, 2014). The resulted integrated surface-groundwater model allows to represent the spatiotemporal changes in these components (Markstrom and Hay, 2009; Sophocleous et al., 1999).

In this context, macroscale hydrological models (e.g., global and regional) provide important tools to construct a comprehensive understanding of watershed hydrology for planning sustainable water resources (the focus of this study). More accurate estimators regarding hydrological processes are obtained by coupling many Land Surface Models (LSM's, Bierkens, 2015). These efforts provides a framework for

developing large scale water resources models, which helped simulating surface and lateral subsurface water flow for many river basins (Arnold et al. 1998, Liang et al., 1994). Macroscale hydrological models are used to simulate global blue water use and availability (MHM, Alcano et al. 1997; Shiklmanova, (1997); WBM, Vorosmarty et al. 1998), reservoir operation (Hanasaki et al., 2006), floodplain inundation (Yamazaki et al. 2011; Kauffledt et al., 2016), water scarcity based on availability and demand (Hanasaki et al., 2010; Pohkerl et al., 2011; Alcamo et al., 2010; Abbaspour et al. 2015), groundwater depletion (Wada et al., 2010; Pokhrel et al., 2011), and recently Carbon and Methane emissions (Petrescu et al., 2010).

Two popular models have been used extensively to study watershed hydrology which includes the Soil and water Assessment Tool (SWAT; Arnold et al, 1998), and the U.S. Geological Survey MODular Finite-difference FLOW model (MODFLOW; Harbaugh, 2005). SWAT has been used worldwide for assessing the impact of land management practices on water resources, the associated sediments and chemicals movements, and environmental conditions (Gassman et al. 2007). However, SWAT has limitations in predicting the groundwater table (Vazquez and Angel, 2005), which may be due to the lack of accurate spatial representation of heterogeneous soil properties affecting the groundwater flow and distribution within the soil system (Peterson and Hamlett, 1998; Spruill et al., 2000). Therefore, in many studies, the one-dimensional groundwater component in SWAT model is coupled with three dimensional fully distributed continuous groundwater component available in MODFLOW (Harbaugh, 2005). This coupled SWAT-MODFLOW model can improve the representation of hydrologic process specifically he base flow and groundwater.

With the fully coupled surface and groundwater model approach, more uncertainty is introduced to the resulted simulations which can greatly influence the model performance leading to misleading predictions when such uncertainties are not

addressed in the calibration process (Abbaspour et al., 2006; Yangetal et al., 2007a). In addition, the implementation of such sophisticated approach can be challenging for many stakeholders. However, the fully coupled approach allows for more accurate representation of mass and energies between the hydrological cycle components (Sun et al., 2012). For many existing regional ground and surface water models, satellite data (e.g., precipitation, temperature, soil moisture, etc.) have provided meaningful information, which continuously helped improving model predictions. One such data source explored for this purpose is Gravity Recovery and Climate Experiment (GRACE) satellite data, which provides additional information for calibrating SWAT-MODFLOW model in combinations of stream flow discharge data especially in regions with limited data. The final form of GRACE data represents the terrestrial water storage variations for global and watershed scales, which includes the mass variations for both at and below earth's surface (i.e., surface and ground water). During the calibration process, the uncertainties are provided a probabilistic range to account for several sources of errors in the coupled SWAT-MODFLOW model. We extended the use of the Sequential Uncertainty Fitting (SUFI) available in SWAT-CUP package to calculate parameters for SWAT-MODFLOW model. This is accomplished by introducing a comprehensive calibration method which includes adjusting both SWAT and MODFLOW parameters during the calibration process. This calibration approach reduces uncertainties in hydrological model parameters by solving nonlinear objective functions and removing interdependency of mode parameters. SUFI algorithm proves to be very robust in predicting the parameter uncertainty and the corresponding streamflow simulations, although it requires massive number of simulation runs (Abbaspour et al., 2004).

The stream-aquifer interactions and the related water management issues in the TERB, the largest river basin in the Middle East (Figure 5.1), are very complex

and of a long struggle between the riparian countries, Turkey, Iran, Iraq, and Syria (Jaradat, 2002). Aggressive water management polices have been implemented by countries located in the upstream of the TERB to meet the increasing irrigation and population water demands (Altinbilek 2004; Bozkurt and Sen, 2013). The effect of water stress is being manifested by the decline in mean annual stream flow observed at Kut station (southern TERB), where the flow reduced by abou 50 m^3s^{-1} between 1931-1973 and 1974-2004, given similarity in mean annual precipitation in these two periods (473.34 mm and 472.80 mm, respectively) (Ajaaj et al., 2017). Thus, it was suggested that the TERB is vulnerable to extreme drought under such management plans (Wilson, 2012; Issa et al. 2015). Consequently, more people in TERB (approximately 75%) rely on the ground water and because of that the region has lost large parts of their water storage due to the extensive pumping of the groundwater from the aquifer systems with the lack of precipitation (drier arid areas; Ajaaj et al., 2017). This water scarcity conditions triggered severe negative consequences on health, environment, and the ecosystem due to change in water quality and quantity in the TERB (Altinbilek D., 2004; Al-Ansari and Knutsson, 2011). Several other concerns include; low surface flow and groundwater depletion and reduction in water storage and quality (Issa et al. 2015; Wilson, 2012; Venn et al. 2013; Voss et al., 2013); degradation of agricultural lands (Jabbar and Zhou, 2012) and drying of wetlands and marshlands (Jones et al., 2008) southern parts of TERB; alteration of waterways due to low flow caused by rivers damming (Nilsson et al., 2005); and increasing salinization in agricultural lands (Wu et al., 2012).

To the best of our knowledge, this is the first study that investigates the integrated surface and subsurface water resources for the entire TERB including a comprehensive calibration method. However, there are several studies that investigated relatively smaller parts of the hydrological system in this watershed. The

earliest known numeric simulations within TERB is the model developed by Jones et al. (2008) to evaluate the impacts of the constructed engineering projects on the marshlands. The stream flow was simulated for the period 1964-1998 utilizing a fully continuous rainfall runoff SWAT model. An overall reduction in average monthly surface water flow and water storage was observed for the modeled watershed especially after 1973 (damming period). Bozkurt et al., (2013) used the output of different climate models to estimate the hydro-climatic effects of future climate change in TERB. Several emission scenarios of downscaled GCM's have been tested and revealed that, by the end of this century, a general potential increase in annual temperature is projected over the entire watershed domain, which may have an impact on the snow melting temperature leading to an early flooding. This study further suggested a remarkable decrease in winter precipitation on the northern section of the basin (mostly highlands) and an increase in the southern section. Very limited studies investigated the water resources in small parts of TERB located in Iraq. For example, Mohammed et al., (2012) estimated the runoff and sediment loads from the right bank of the Mosul dam valley.

The overall discussion provided in previous sections highlights the necessity of providing a comprehensive understanding of the water resources in the TERB. This study aims to address the following objectives; (1) to develop a full runoff hydrological model (SWAT) and groundwater model (MODFLOW) for the entire TERB, and creating a full linkage between these two models; (2) to calibrate and validate the integrated SWAT-MODFLOW model using two optimization algorithms which has been added to the past works, and their performance; (3) to apply the best calibrated and validated coupled SWAT-MODFLOW model to evaluate the surface and subsurface water resources in the TERB for the period 1981-1997; (4) to quantify the amount of runoff and groundwater budget in the river basin using the transient

coupled SWAT-MODFLOW model; and (5) to estimate the spatial and temporal variations of infiltration and evaporation losses from different surfaces in the watershed.

5.3 Methodology

5.3.1 Conceptual SWAT-MODFLOW model

The surface and subsurface water systems have been traditionally modeled as if they were separate identities due to complexity of hydrologic processes associated with hydrologic cycle that cannot be modeled accurately (Middelkoop et al., 2001). As the water resources planning and management become important, the development of either surface or subsurface hydrologic systems will affect each other's quality and quantity because of their interaction. These interactions can take many important forms such as water gain and loss between nearly all water bodies and aquifers, spatial distribution of recharge and evaporation for all watershed area, and solute and contaminants transport exchange between both ground and surface water systems (Alley et al., 1999). Many previous studies overlooked these surface-ground water interactions when setting up the hydrological models for many reasons such as the computational limitations. More importantly, the relationship that govern the hydrologic process are highly nonlinear, especially the connection between surface and subsurface water which requires complex hydrodynamics algorithms to simulate the water movement (Tague and Grant 2009; Allen et al., 2010; Winter et al., 1998).

In many previous studies, The unsaturated zone, where most of the interactions take place, is simulated as a soil column through which water flows independently and do not affect the underlying water table. This means that in these models

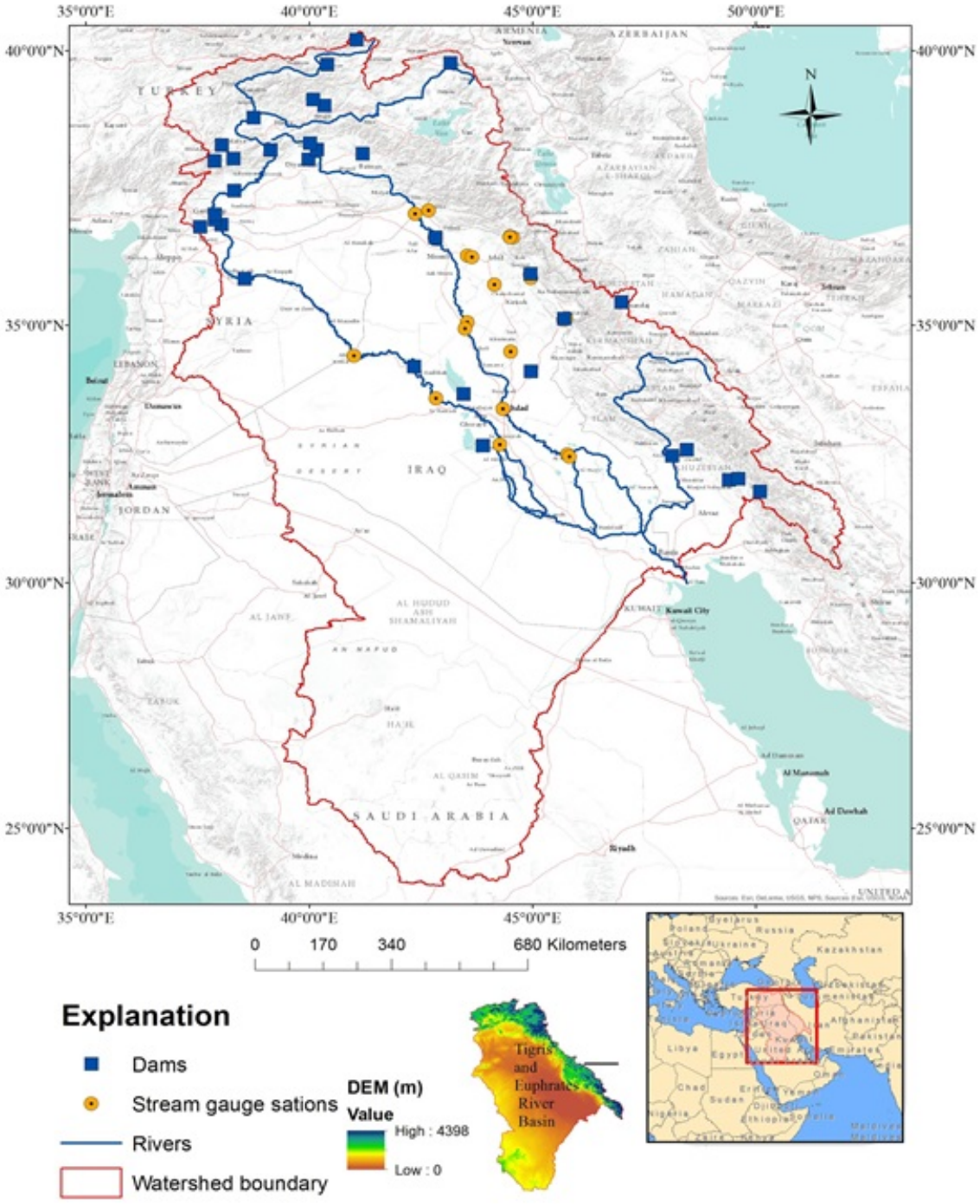

Figure 5.1: Location and general features of the Tigris and Euphrates river basin, Middle East.

there is no clear representation to the dynamic interaction of the surface and subsurface water flow. Furthermore, the effects of climate on these interactions and the resulted summer time flow in snow-melt driven streams have not been fully understood due to several compartmental model assumptions and limitations (Scibek et al.2007). Huntington and Niswonger (2012) pointed out the importance of considering the coupling manner as a key process for understanding summer time stream flow in snowy watersheds, which is the case of the study area considered in this work.

SWAT is a popular hydrologic and water quality model developed by the USDA Agricultural Research Service (USDA-ARS). SWAT is a long-term, lumped, continuous, watershed-scale simulation model that designed to assess the impact of different management practices on water, sediment, and agricultural chemical yields for subbasin scale (Arnold and Fohrer, 2005). SWAT divides the watershed into multiple sub basins which are further classified into unique combinations of land use, soil type, and slope known as Hydrologic Response Units (HRU's). SWAT performs its calculations for each HRU then integrates them to sub basins based on the percentage of each HRU in that sub basin (Wible et al., 2014). SWAT model emphasis on plant and crop growth, nutrient cycling, and sediment yields from urban, natural, and agricultural areas. SWAT also simulates snow pack processes using water mass balance equation implemented on HRU scale to calculated snow accumulation. Total precipitation is classified as solid or liquid based on a threshold of mean air temperature which determines snow accumulation and snow melt (ETIENNE et al., 2008; Zhang et al., 2008). The groundwater dominated system in SWAT model can sometimes fail to accurately represent the heterogeneous groundwater flow processes due to its lumped approach (Peterson and Hamlett, 1998; Spruill et al. 2000; Chu and Shirmohammadi, 2004).

MODFLOW is a watershed, three dimensional, saturated, finite difference

model (Hargangh et al., 2000). MODFLOW combines the mass balance equation with Darcy's law to solve for steady and transient groundwater flow conditions. Different packages were added to MODFLOW main solver to enhance its performance in solving drying and rewetting conditions. Some of main components for MDOFLOW are Infiltration, Evapotranspiration, Vadose zone percolation, and river groundwater interactions (Niswonger et al., 2006; Hargangh et al., 2000). The multi-layer and grid discretization approach for MODFLOW gives better representation of spatial variations for soil system. However, MODFLOW is unable to simulate overland flow, sheet erosion, channel erosion, plant and growth, nutrient cycling, and agricultural management (Wible et al., 2014).

By considering the drawbacks of SWAT and MODFLOW models, a coupled SWAT and MODFLOW models can provide a more comprehensive watershed simulation by modeling the surface and subsurface interactions (Galbiati et al., 2006). There are few studies that attempted to couple SWAT and MODFLOW models using different approaches (Kim et al., 2008). Table 5.1 summaries some of the studies that used different coupling techniques for SWAT and MODFLOW models and also some of their advantages ans disadvantages. These models were able to provide a better insight of the hydrologic process due to their ability to more realistically simulate feed back occur above and below surface. However, many of these studies force an equal spatial discretization for computational units (i.e. same HRU and cell sizes respectively in case of SWAT and MODFLOW; Chung et al., 2010). Our proposed modeling framework utilized the comprehensive SWAT-MODFLOW model developed by (Wible et al. 2014) where they outlined the full linkage procedure for the two model components and used the same spatial discretization for both SWAT and MODFLOW models. In this study, The capacity of the enhanced model compared to the original SWAT and MODFLOW models was demonstrated for two small

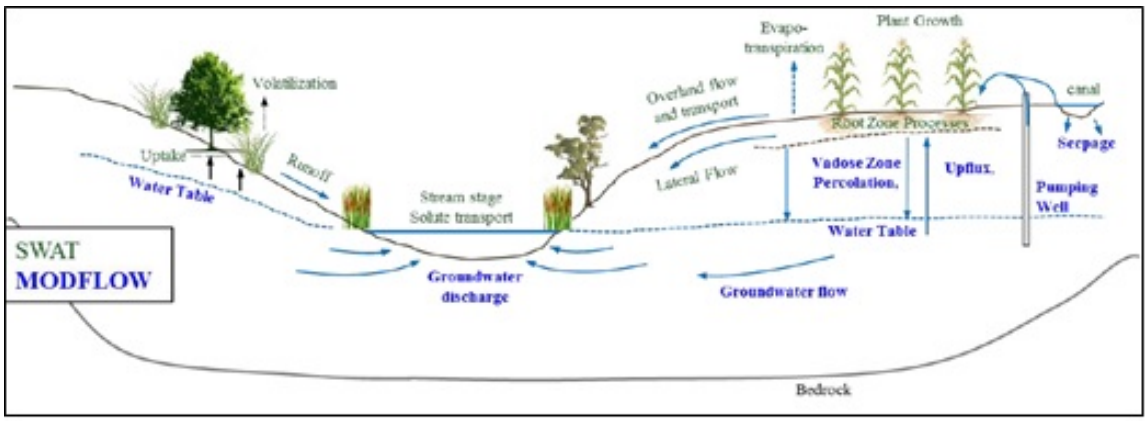

Figure 5.2: Coupled SWAT-MODFLOW watershed hydrologic modeling framework (Wible et al., 2014).

watersheds. Yet, this integrating coupling has not been tested nor calibrated for large scale watershed (Wible et al. 2014). Constructing the coupled model includes writing linking functions which facilitate passing fluxes calculated in each model to the other.

In our coupled model, the latest versions of SWAT 2012 (Arnold et al., 1998) and MODFLOW-NWT 2011 (Niswonger et al., 2011) were used. The MODFLOW-NWT uses Newton's solver that handles the drying and re-wetting grid cell options. SWAT-MODFLOW model allows each sub model to retain same strength, and adds new components resulting due to the linkage process (e.g. recharge, river and groundwater interactions, river stages, and many others). Unlike the previous coupling attempts in which results presented based on monthly scale, here SWAT-MODFLOW results are presented based on daily time scale which is more useful for most of water planning issues. The essential flow components considered by this model are shown in Figure 5.2. Wible et al., (2014) provides a complete description of SWAT-MODFLOW coupled model and its theory.

Table 5.1: Previous studies that investigated coupled SWAT-MODFLOW models using different techniques.

Reference	Description	Advantages	Disadvantages
Perkins and Sophocleous,1999	One of the earliest attempts to couple SWAT and MODFLOW models by adding a separate package to print SWAT parameters that are necessary for MODFLOW, and read statement in MODFLOW to read pass them, then adding third software for converting the inputs for MODFLOW	Specifying distributed hydrological conditions such as tributary flow, recharge, evaporation, and diversions from surface and groundwater rights for irrigation and other uses at watershed surface and soil profile.	1)Relies on use of third package. 2)Simulates only monthly stream flows. 3)The software was run and calibrated by the developer and it is not available for public.
Menking et al., 2003; 2004	This study considered using SWAT model of the Estancia basin, New Mexico to estimate watershed streamflow outputs which then were used as inputs for MODFLOW to calculate the hydrologic balance of the that lake.	Specifying distributed hydrological conditions such as tributary flow, recharge, evaporation at watershed surface and soil profile.	Was not really fully model coupling where SWAT outputs were taken to MODFLOW. Simulates only monthly stream flows. The software was run and calibrated only by the developer and it is not available for public.
Galbiati et al., 2006	SWAT was coupled with MODFLOW for including hydrologic, chemical, and nutrients simulations(MT3DMS) at to the Bonello coastal basin in Northern Italy.	Besides the points above, the chemical movement and nutrients simulation were included in the model.	The results were simulated for only monthly time scales. . The software was run and calibrated only by the developer and it is not available for public.
Harbaugh et al., 2010	An attempt for developing an integrated SWAT and MODFLOW models which was used for better representation of base flow for a watershed in South Korea.	Specifying distributed hydrological conditions such as tributary flow, recharge, evaporation, and diversions from surface and groundwater rights for irrigation and other uses at watershed surface and soil profile.	The results were simulated for only monthly time scales. The hydrologic response units (HRU's) were forced to form grids to fit the MODFLOW grids which reduces the computational efficiency of the lumped models. The software was run and calibrated only by the developer and it is not available for public.
Wible, 2014	Constructing fully coupled SWAT-MODFLOW model to enhance the capacity for modeling the watershed processes at daily time scale. The uncalibrated model North Fork of the Sprague River in the Upper Klamath basin, Oregon was underestimating the streamflow for the entire period of simulation.	1) Specifying distributed hydrological conditions such as tributary flow, recharge, evaporation, and diversions from surface and groundwater rights for irrigation and other uses at watershed surface and soil profile. The chemical movement and nutrients simulation were also included in the model. 3) The software is available for public.	1) The results were simulated for only monthly time scales. 2) The hydrologic response units (HRU's) were forced to form grids to fit the MODFLOW grids which reduces the computational efficiency of the lumped models. 3) The integrated SWAT-MODFLOW software was not calibrated by the developer.

5.4 Description of the Study Area and Data

The Tigris and Euphrates River Basin (TERB) encompasses a drainage area of around 900,000 km^2. Iraq, Turkey, Syria, and Iran among the main riparian countries that share the water resources of the two important rivers and their tributaries, and use it for multiple critical purposes such as hydroelectric power generation, irrigation, and domestic use (Kavvas et al., 2011). These two rivers originate in the highlands southern Turkey (upper part of TERB), flow through Syria (only Euphrates river), and enter the territory of Iraq in the north and the north east. The topography of the TERB is highly variable where the elevation ranges from few meters in the south (Mesopotamia fertile plain) to 4398 m above the sea level in the northeast (Mountains region). In Iraq, Tigris and Euphrates rivers flow separately onto a wide, flat, hot, and poorly drained plain. In the middle of their path they diverge hundreds of kilometer apart and join together near Qarmat Ali about 160 km above the Gulf, forming Shatt al Arab (Issa et al., 2014). The TERB is characterized by its transitional climate between Semi-humid at the northern part of the TERB (highlands) and semi-arid climate at the southern parts of the southern part of the TERB (low lands). The climate factors that commonly affect both the groundwater and the surface waters are the precipitation, maximum and minimum air and temperature data.

The Asian Precipitation-Highly-Resolved Observational Data Integration Towards Evaluation of water resources (APHRODITE Asia) product is found to be more representative to the study area based on a comparative study data sources (Ajaaj et al., 2017) used in the hydrological SWAT model. APHRODITE was used in SWAT model due to the scarce actual observed data in the study area resulted from political instability. The period of climatological precipitation records for APHRODITE is available for 1951-1997 period. The daily precipitation data is provided based on

0.25x0.25^o longitude and latitude and the grids with missing data are simply removed from the data sets. The long-term mean monthly precipitation for the same time period was found and represented in Figure 5.3. This figure shows that the rainy season usually starts in winter (October-April), while the rest of the year witnesses rainfall below average and approximately no rain during summer on most parts of the watershed. Most of winter precipitation on the highlands of the upper part of TERB (mountains) is mostly stored naturally as snow pack. Therefore, the flow of the two rivers is seasonal and dominantly relies on snow melt during spring season (Jones et al., 2008). The large spatiotemporal variations in air temperature of the watershed significantly controls the percentage of precipitation that turns into snow and the surface runoff which eventually determines amount of surface water flowing in the streams (Ajaaj et al., 2015).

The Gravity Recovery and Climate Experiment (GRACE) satellite mission, sponsored by NASA and its German counterpart DLR, measures spatiotemporal variations of Earth's gravity fields (Waher at al., 1998). The nominal product is expressed in a form of spherical harmonics coefficients at a monthly global scale (Tapley at al., 2004a). The time variations in these coefficients are directly related to mass changes in the Terrestrial Water Storage (TWS) for both land and oceans (Swenson and Milley, 2006; Ramillien et al., 2005). However, shortwaves add a noise component that needs to be removed from gravity field coefficients through a filtration process (smoothing; Swenson and Wahr, 2011). Several filtering approaches have been applied to the TWS to remove systematic errors due to scaling and truncation processes (e.g., Guassian filter, an anisotropic filter, optimal filters; Landerer et al., 2012). The resulting TWS variations given by GRACE data has been widely used to estimate the water storage variations on sub continental scale (Seo at al., 2006); large river basins (Xie et al., 2016); ground water storage variations (Alexenbder et al., 2012).

Over the last few decades, a rapid agricultural developments in the upper part of the TERB in undergo as widespread irrigation has introduced to the region. The increasing agricultural development is not newly introduced to the region, where general plan is implemented by main riparian countries which permits to irrigate more than 1,083,000,558,000 ha and utilizes up to 9,000,106 m^3 of water each year from the Tigris and Euphrates rivers, respectively (Beaumont, 1996). The water of Tigris and Euphrates rivers is mostly utilized in narrow belt along of the two rivers and their attributes until the two rivers enter the Mesopotamian Plain (alluvial formation), which extends over the South-East and Central Iraq. This makes 25% of the irrigated area of Iraq relies on surface water which emphasize the importance of using the groundwater to develop the other 75% of the total area.

5.5 Hydrogeological Setup of Study Area

In the study area, the lithology and the structure of the geological conditions determine the spatial distributions and the extent of the hydrogeological features (aquifers and aquitards) and their hydrological environment. The TERB is located at the center of alluvial depression extends from central Syria to the Arabian sea, known as (Mesopotamia and Jezira plains), which is characterized by low topography and cultivated feature, and contains the youngest sediment deposits in the area (Quaternary and Neogene). It is flanked by the older strata of Mio-Pliocene and Palaeozoic age, where from the west and the south west by a plateau called that gently inclined towards that depression and from the east and the north east by a series of ridges and depressions (Foothills plain) passing eventually to the mountains (Mountains plain). The western desert lies to the south west of the depression. The highest point of that formation lies at the far west of western desert, and from there, the slope decreases

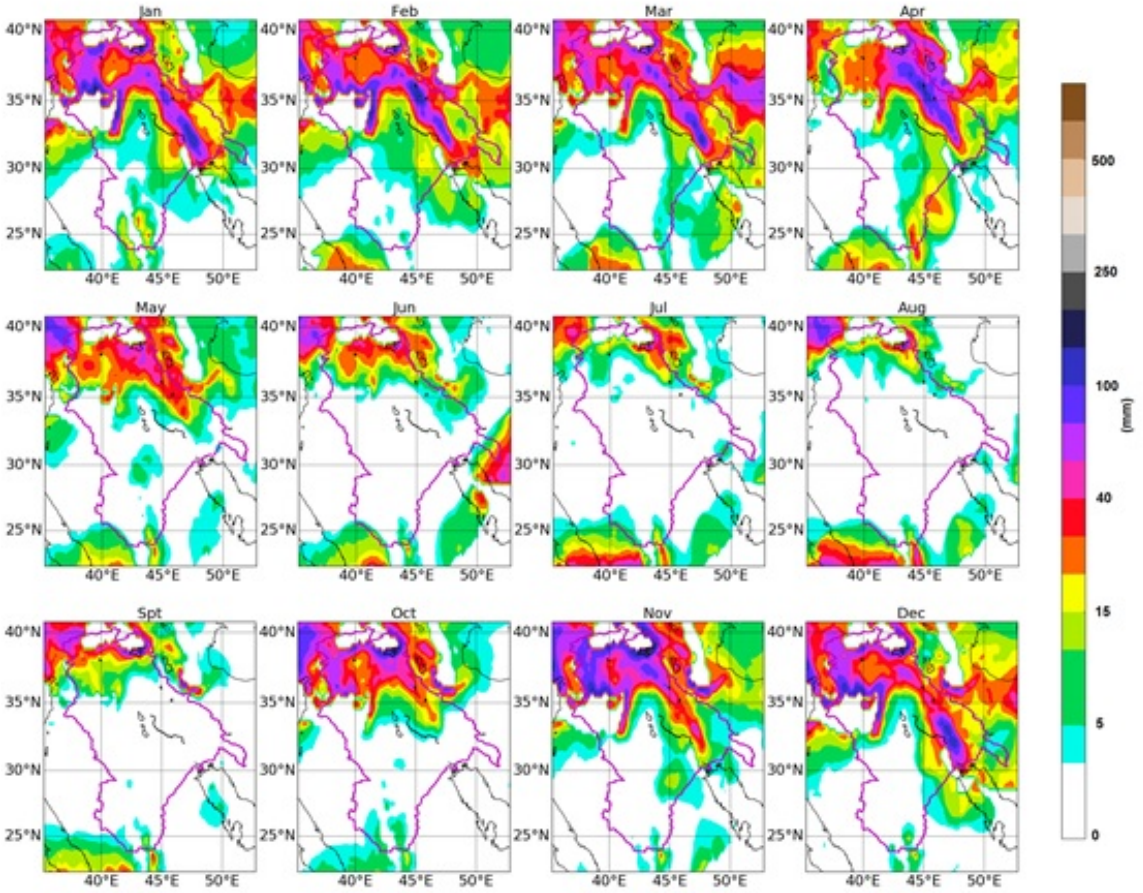

Figure 5.3: Long-term mean monthly precipitation over the study area for the period (1951-2007). The data sets are based on APHRODITE precipitation data for Asia.

gently towards Euphrates River (Figure 5.4).

The superficial geology of the TERB mainly includes ten aquifer systems used in evaluating the groundwater resources. The classification of the main aquifers is identified based on their relationship to geological formations and explained in Table 5.2. More details can be found in (Jassem et al., 2006). Based on that table, the geological units were further grouped into five hydrogeological units that share similar lithological characteristics and hydrological properties. The five hydrological zones used in this work include the Aquifer System of the Western and the Southern Desert, the Jezira Hydrogeological Region, including Sinjar region, the Aquifer System of the Mesopotamian Plain, including Baquba-Tikrit region, the Aquifer systems of alluvial fans, Mandali-Badra-Tib region, and the Aquifer system of the Foothills.

5.6 SWAT Model

The ArcSWAT 2012 interface is used to set up and parametrize the surface water model. Table 5.3 summarizes the data sets used to develop SWAT model which are freely available online. SWAT simulation requires delineation of stream network to rout the water flow, subbasin delineation to determine model parameters through calibration, and assembly of climate data needed to derive the model. The delineation of the watershed and the stream network were based on DEM (90 m resolution) with a threshold area of 4,218 km^2 which was used to discretize the watershed into 419 sub-basins. The sub-basins were further subdivided into 11,124 HRU's based on a unique combination of soil, land use, and slope. Water balance calculations are conducted for each HRU. The SWAT model represents the 17-year period from 1981 through 1997. The model begins simulations 5 years prior to 1981, where (1976-1980) was selected to warm up the model and adjust hydrologic conditions at the start of the

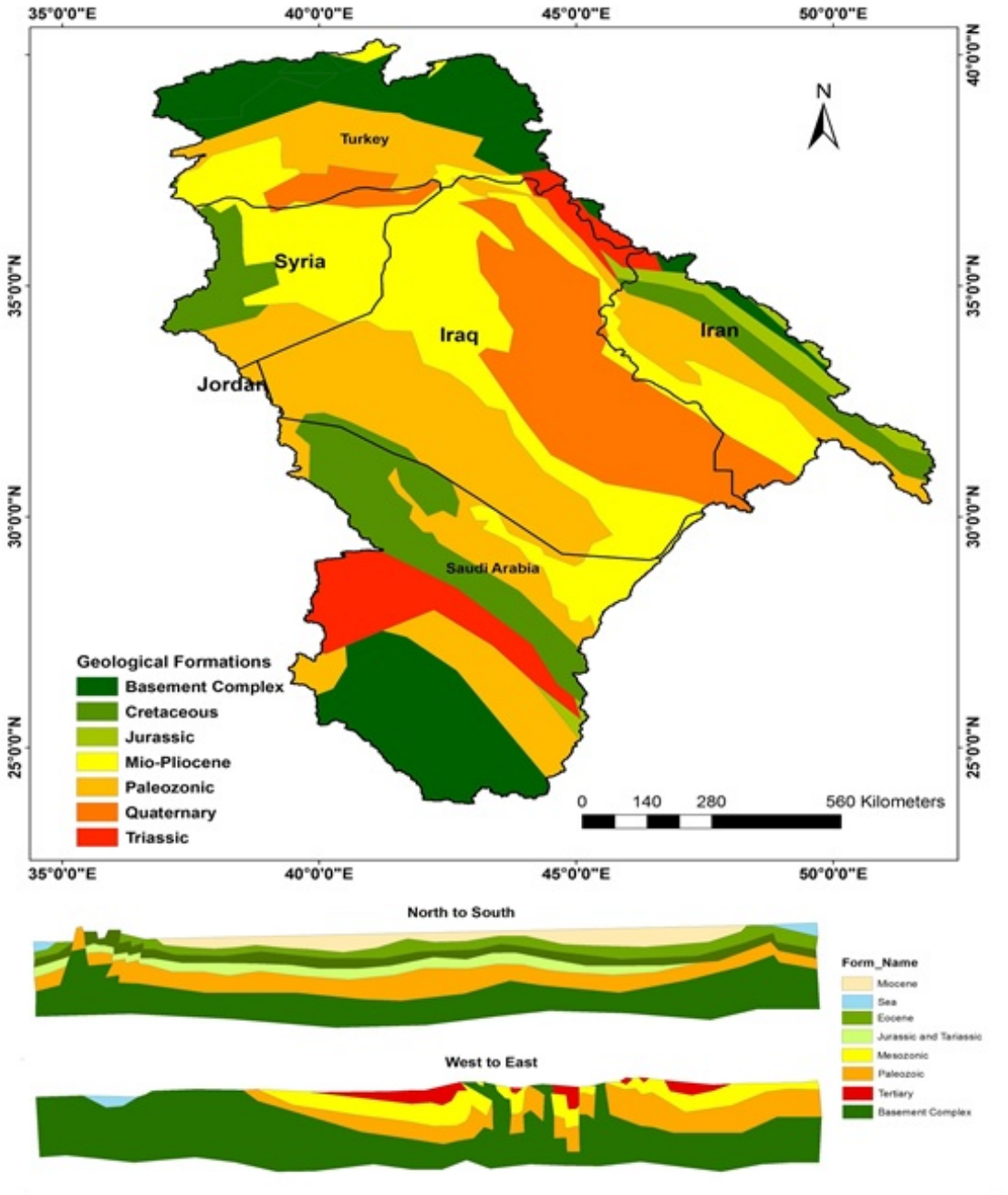

Figure 5.4: Surficial geological layers of the TERB and vertical stratigraphy for the study area.

Table 5.2: Geological setup in the TERB

No.	Aquifer	Sediments Type	Thickness (m)	Transmissive m^2/day	Storativity
1	Fractured Cretaceous-Tertiary limestone of Rutbah, Digma, Tayarat Akashat, and Ratga formations	Limestone with fine coarse grained sand and sandstone.	Few meters-450	50-250	10^4
2	Sandstone of the permocarboniferous Ga'ara and Bir El-Rah formations	Sandstone	200-700	100-250	10^4
3	Fractured limestone and sandstone of Triassic-Cretaceous age	Limestone and dolomites, inter-bedded with marl	180	200-600	–
4	Karstified and fractured limestone of Palaeocene-Eocene of the Southern Desert	Dolomite and Dolomite Limestone with beds of gypsum and anhydrite	200-400	–	–
5	Miocene sandstones and Pleistocene connglomerate of Nukhaib	Miocene sandstone	100-200	–	–
6	Sandstones of Miocene-Pliocene Dibdibba Formation	Permeable sandstones (partly pebbly) with beds of mud-stone, siltstone, and marl associated with secondary gypsum	30-260	–	$5x10^{-9}$ – 2.5×10^{-8}
7	Alluvial fan of Wadi Al-Batin	Comprises permeable gravels and coarse sand, alternating with marl	–	500-2500	–
8	The Fatha (Lower Fars) Formation	Interbedded organo detrital limestones with gypsum	100-400	>400	–
9	Quaternary sediments of Mesopotamian Plain	Silt and clay silt	2-200	200-300	–
10	Mukdadiya Formation and Injana Formation	Clay, sand and Gravel	200-550	100-5000	–

calibration and validation periods.

Table 5.3: Streamflow gauging stations located in TERB and used in this study.

No.	River Name	Station	Latitude N	Longitude E	Subbasin Area mk2	Data Availability From	To
1	Tigris River at Paish Khabur-Tusan	IRQT1	37°04'00"	42°23'00"	46,700	Jan−58	Spt−75
2	Khabur River at Zakho	IRQT2	37°08'00"	42°41'00"	3,500	Nov−58	Sep−89
3	Tigris River at Mosul	IRQT3	36°37571'	42°49'03"	54,900	Oct−17	Aug−97
4	Rawaduz River at Jidia	IRQT4	36°3 8'00"	44°34'00"	1,160	Feb−57	Sep−75
5	Balikia Rivr at Balikia	IRQTS	36°39'00"	44°30'00"	1,060	Apr−58	Mar−74
7	Gratr Zab River at Bkhm Dam-IMRP	IRQT7	36°38'29"	44°29'42"	2,500	Nov−31	Sep−17
8	Khazir River at Baquba	IRQT8	36°18'00"	43°33'00"	2,900	Feb−43	Jul−94
9	Gratr Zab River at ski Klk	IRQT9	36°16'00"	43°39'00"	20,500	Jan−32	Sep−90
10	Leser Zab River at Doka	IRQT10	35°57'14"	44°57'10"	–	Nov−31	Sep−17
11	Leser Zab River at Doka Village	IRQT11	35°53'00"	44°58'00"	11,700	Apr−52	Sep−75
12	Leser Zab River at A ku Kupri-Goma	IRQT12	35°45'411'	44°08'52"	–	Oct−32	May−87
13	Tigris River at Fatha	IRQT13	35°03'00"	43°33'00"	107,600	Mar−17	Sep−99
14	Tigris River at Biji	IRQT14	34°55'45"	43°29'35"	–	Apr−17	Mar−17
15	Adhaim River Ijaa	IRQ_T15	34°30'00'	44°31'00"	9,840	Oct−45	Sep−97
16	Diyala River at Drbdi-Khan	IRQ_T16	35°08'00"	45°45'00"	17,800	Nov−31	Sep−17
17	Diyala River at discharg sit	IRQT17	35°06'01"	45°42'02"	29,700	Jan−17	Sep−91
18	Tigris Rivr at Baghdad	IRQ_T18	33°24'34"	44°20'32"	134,000	Mar−17	May−17
19	Gharraf Canal	IRQ_T19	3231'55"	4547'25"	–	Dec−40	Mar−17
20	Tigris River dowstram of Kut Barrag	IRQ_T20	3229'00"	4550'00"	166,200	Oct−17	Nov−2005
21	Euphrats River at Husaybah	IRQ_E1	34°25'20"	41°00'38"	–	Nov−81	Spt−1997
22	Euphrats River at Hit	IRQ_E2	33°36'23"	42°50'14"	264,100	Oct−32	May−97
23	Euphrats River dowstram of Hidiya Barrag	IRQ_E3	32°43'01"	44°16'01"	274,100	Feb−30	Spt−99

The stream network was divided into 419 stream reaches, where a stream reach is considered as a length of a stream that is contained within a single SWAT model sub basin. All streams were delineated based on the topography of the study area. The reach defined in each sub basin does not necessary require that water flows in that reach. However, A stream naturally flows whenever there is a runoff or base flow contributes to the reach.

The availability of streamflow data is very limited for most locations in TERB. A total of 23 river discharge stations were found reliable to use in calibration and validation process (Figure 5.1). Table 5.3 lists a summary of the stream flow stations used for SWAT-MODEL calibration. Majority of river discharge stations are located on Tigris River and only two stations on Euphrates River. In case of missing monthly flow rate, the average flow rates of two forward and backward months was substituted

the missing moth. During the water years (1959-1997), the annual total stream flow varies from a maximum of about 6,988 m^3s^{-1} for the wettest water year in 1988 to a minimum of about 455.7 m^3s^{-1} for the driest year 1985 in Fatha station. For monthly total streamflow, the seasonality is strongly associated with the highest stream flow during February-April. After May, the decrease in precipitation causes surface runoff to decrease and that the base flow component becomes dominant from May to September.

Table 5.4: An overview of data used in this study

Data Type	Data Resolution	Source
Digital elevation model (DEM)	90 m	The Shuttle Radar Topography Mission (SRTM)
Digital soil type	500 m	Food and Agriculture Organization (FAO-UNESCO)
Land use and land cover (LULC)	250 m	
Climate data	0.25^o grids	Asian Precipitation - Highly-Resolved Observational Data Integration Towards Evaluation of water resources (APHRODITE)

5.7 MODFLOW Model

Gridded datasets of elevation, geology, and soils were used to discretize and parametrize MODFLOW model. Watershed boundary shapefile defined by SWAT model was used to set up the MODFLOW boundary where the cells outside the polygon were assigned as inactive boundary. Model grid sizes were set to a 250x250m over all the model domain. Hydrological units defined earlier were discretized vertically into 5 geological layers, and horizontally into 42,222 cells per layer, with a total of 18,706 active cells. The geological formations (included in Table 5.2) were

used to estimate the hydrogeological properties of each rock. In case of missing rock information, the values were estimated with the model calibration.

The land cover of TERB watershed mostly contains desert in the west and south west, and agriculture and vegetation land cover types in the north. The long-term land use changes in the TERB had three dramatical effects on the hydrological system. Turning the natural vegetation cover to agriculture or urban areas increases the total amount of runoff generated along the streams due to flush water in a short period (Sloop et al., 2009). It could also decrease the direct infiltration to the sub soil zone and the direction of the ground water movement.

5.8 SWAT-MODFLOW Model Calibration

The calibration of SWAT-MODFLOW was an iterative process, conducted by adjusting model parameters to obtain a reasonable fit between simulated flows and hydraulic heads with measured data. The adjustment of these parameters was repeated for each gauged subbasin at the outlet in the TERB. The simulation was conducted using monthly streamflow and changes in groundwater storage over the entire TERB. The streamflow was simulated during a 19-year historical period (1979-1997). The model was calibrated using multi-steps process. The SWAT model was first calibrated independently to match the monthly-observed streamflow for the 19-year period. The Sequential Uncertainty Fitting-2 (SUFI-2) built in SWAT-CUP package was employed in this step to adjust parameters and reduce uncertainties in simulated streamflow. The first three years of simulation was used as model warm up to establish initial flows in stream network. Initially a set of 26-parameters associated with solar radiation, snow, runoff, evaporation. etc., was selected as a default SWAT model parameter entries for sensitivity analysis. After preliminary analysis, 10 most

sensitive parameters were used for SWAT calibration.

In the second part of calibration, the groundwater component modeled by MODFLOW is separately calibrated using an automated parameter estimation supported under AQUAVEO-GMS package using PEST (PESt Estimate) parameter estimation tool. MODFLOW initial parameters were evaluated using steady state stress period. Long-term average recharge, hydraulic conductivity, and channel bed transmissivity were adjusted to match observed groundwater levels obtained from number of wells limited to two locations in the model.

For the third step in model calibration process, coupled SWAT-MODFLOW was run in an integrated mode, and the aquifer layer parameters were adjusted to match actual streamflow and groundwater levels. Due to limited groundwater observations for the watershed, MODFLOW predictions were validated in two methods. The first method includes changing the groundwater parameters and matching the variations in observed monthly low flows of streams during the period 1981-1997. In the second method, the total water storage variations from coupled SWAT-MODFLOW is assessed with GRACE satellite-based terrestrial total water storage variations (ΔTWS) during the period 2002-2013. The potential use of GRACE satellite product in calibrating regional MODFLOW models has been previously verified for other watersheds (Sun et al., 2012). The only constrain in using such data is the need for separating surface water storage component before validation. However, using an integrated surface and ground water hydrological model eliminates this limitation because of the ability of this coupled model to simulate total water storage variations, which allows to directly comparing with GRACE total water storage variations. The second method was associated with calibration for additional parameters refinement that affect timing of runoff and subsurface flow towards streams.

5.9 Validation of GRACE Data

In this study, we compare the GRACE total water storage variations to SWAT-MODFLOW model annual and monthly outputs during the period 2002-2013. The GRACE observations can be compared to the SWAT-MODFLOW using two methods including; (i) direct method, used in this study as it counts for all storage components; and (ii) indirect method. In semi-arid climate, the groundwater and soil moisture (ΔGWS) contribute the most part of the observed ΔTWS because the perennial surface waters are sparse (Sun et al., 2010). However, we counted for all components including surface water storage because of the wet areas in the northern parts of the watershed which are dominant by snow fall in rainy season. Table 5.5 summarizes the ΔTWS components translated to SWAT-MODFLOW water balance equation.

Table 5.5: The ΔTWS components represented in SWAT-MODFLOW water balance equation

Total water storage components ΔTWS	Modeled by
Over land flow (V_1)	SWAT
Lagged and lateral surface and subsurface flow (V_2+V_3)	SWAT
Vadose Zone storage (V_4)	SWAT
Snow equivalnet water storage (V_5)	SWAT
Soil moisture profile (V_6)	SWAT
Groundwater storage, shallow and deep aquifer (V_7)	MODFLOW

GRACE observation provides outputs at regional scales (i.e., over basin sized area) and represent gridded model anomalies. Therefore, hydrological model outputs should be converted to water depth anomalies and averaged over the entire basin to produce meaningful results that can be compared to GRACE data. Month to month variations in regional mean ΔTWS obtained from SWAT-MODFLOW anomaly were evaluated in this procedure and assessed against GRCE water storage anomalies.

5.10 Results

5.10.1 Calibration and Sensitivity Analysis

The ability of SWAT-MODFLOW model to simulate groundwater conditions is shown in Figure 5.5 by comparing simulated and observed groundwater mean monthly water levels for the calibrated wells. The results of steady state groundwater water calibration revealed that MODFLOW model could simulate water elevations reasonably well for the calibrated wells at two locations in the TERB, even though with the heteronomous in the watershed. The overall correlation coefficient (R^2) was 0.92 with groundwater level difference of 0.27m to -0.41m. The description of groundwater discrepancies maybe due to errors in representing model heterogeneities and model parametrization.

Hydraulic properties of the watershed and the consolidated rock units varies among HRU's. Table 5.6 summaries the final ranges of calibrated parameters for coupled SWAT-MODFLOW model averaged over all layers. The important components in the coupled model includes elevation, HRU data, basin area, spatial location, land cover type, and soil type. Based on the analysis of water balance, the distribution of parameters can be classified into four different regions (surface, soil, stream, and groundwater) as shown Table 5.6. In the surface region, the parameters affecting precipitation, infiltration, runoff, and change in surface storage were adjusted during calibration. The amount of surface runoff mainly depends on the SCS II curve number "R__CN2.mgt" which was initially calculated from the land use, land type, and land slope maps, then this value was further adjusted by a ration in the calibration. The snow parameters that control the snow melt temperatures were also important in the model calibration, where the optimized snow melt temperature "V__SFTMP.bsn" was estimated as -1.7^{o}C during winter months (rainy season).

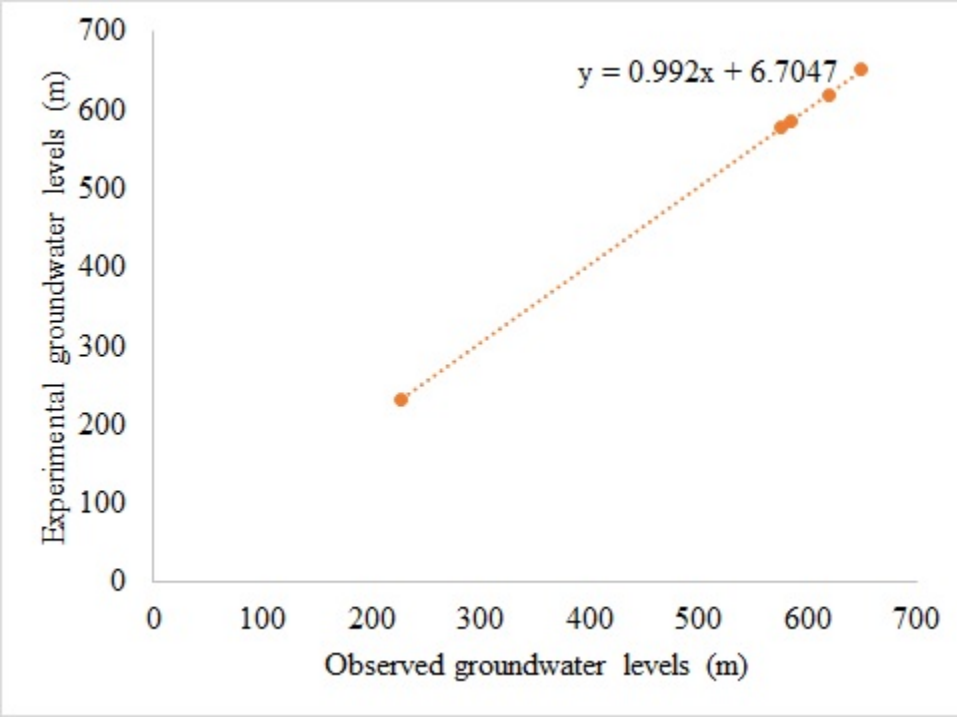

Figure 5.5: Relationship between simulated and observed mean monthly well groundwater levels in the TERB.

The available water in the soil zones is usually conceptualized as three reservoirs filing the same physical space but governed by different processes, including the capillary reservoir (water held by capillary forces), the groundwater reservoir (the soil moisture ranges from field capacity to saturation), and the preferential flow reservoir (the soil moisture exceeds the preferential flow threshold). In the capillary reservoir, the two most important soil parameters that define the available amount of water for runoff and evaporation are the Soil Available Water holding Capacity R__SOL_AWC(..).sol and the Soil Evaporation Compensation Factor "V__ESCO.bsn", respectively, which are defined initially based on land cover and adjusted in the calibration process. In the groundwater region, the hydraulic conductivity (HK) for the deep layers was varied from 3 to 10 md^{-1}, and the average zonal specific yield (SY) of the unconfined first layer ranges from 0.003 to 0.07.

Figure 5.6 compares between the total water storage anomalies (ΔTWS) simulated from coupled SWAT-MODFLOW model and obtained from GRACE satellite based data. The comparison indicated a good positive correlation with correlation coefficient (R^2) of 0.72 (Figure 5.6a). This result coincides with many studies evaluated the use of GRACE data in calibrating hydrological models (e.g., Lo et al., 2010; Moiwo et al., 2010). The extended long-term comparison of ΔTWS during 2002-2013 suggests that the pattern of GRACE data is well captured by the coupled SWAT-MODFLOW signal. However, SWAT-MODFLOW does not generated changes from dry to wet year, as the case between 2008 and 2009. Such behavior of hydrologic models is also observed by Sun et al., (2012) who applied the GRACE data to calibrate regional models. Ideally, the lack of a better representation of the hydrological model to GRACE data can be attributed to many factors. Firstly, the relatively coarse parameter structure for the models (SWAT-MODFLOW and GRACE data) restrict the degree of freedom for model fitting, which can be difficult for transient

Table 5.6: Final Calibrated model parameters used for TERB modeling; these parameters were obtained from available data and adjusted during model calibration. Parameters are divided in the five subcategories based on their geographical regions in the SWAT-MODFLOW model.

Vertical zone	Parameter Name [a]	Definition	Unit	Fitted Value	Min Value	Max Value
Surface zone	R__CN2.mgt	Initial SCS runoff curve number for moisture condition II	%	-0.195	-0.631	-0.183
	V__SFTMP.bsn	Snowfall emperature	^{0}C	3.700	3.405	3.786
	V__SMTMP.bsn	Snow melt base temperature	^{0}C	3.329	2.705	3.566
	V__TIMP.bsn	Snow pack temperature lag factor	–	0.466	0.444	0.486
	V__SLSUBBSN.hru	Average slope length	m	222.726	199.575	231.508
	R__HRU_SLP.hru	Average slope steepness	m/m	1.062	0.846	1.125
	V__OV_N.hru	Manning's n value for overland flow	–	0.170	0.156	0.200
	V__SURLAG.bsn	Surface runoff lag coefficient	–	104.251	94.796	120.009
Soil zone	R__SOL_AWC(..).sol	Available water capacity	mm H_2O/ mm soil	-0.383	-0.483	-0.247
	R__SOL_K(..).sol	Saturated hydraulic conductivity	mm/hr	1.624	1.018	2.071
	R__SOL_ALB(..).sol	Moist soil albedo	%	0.151	0.080	0.486
	R__SOL_BD(..).sol	Moist bulk density	gm/cm3	-0.425	-0.871	-0.361
	V__EPCO.bsn	Plant uptake compensaion factor	–	0.337	0.284	0.369
	V__ESCO.bsn	Soil evaporaion compensation factor	–	0.811	0.801	0.854
Streams	R__CH_K2.rte			0.743	0.694	0.747
Groundwater zone	V__HK	Horizonal hydraulic conductiviy	m/d	3.965	2.500	10.000
	V__HANI	Horizonal anistropy	–	1.600	1.120	1.750
	V__VKA	Vertical hydraulic conduciviy	m/d	1.731	1.100	2.500
	V__SS	Specific storage	m^{-1}	0.00007	0.00002	0.00050
	V__SY	Specific yield	%	0.137	0.050	0.200

[a] V__: means the default parameter is replaced by a given value, and R__ means the existing parameter value is multiplied by (1+the given value).

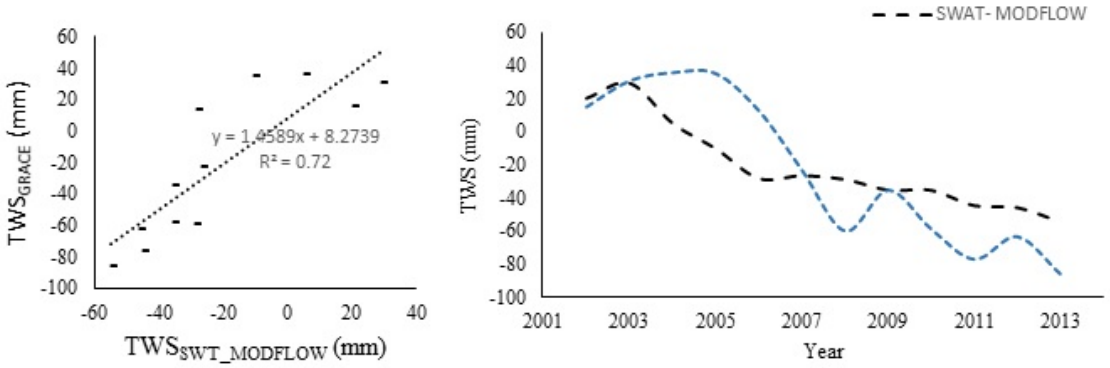

Figure 5.6: Basin mean of total water storage anomalies for the TERB (a) Correlation between mean annual TWS obtained from SWAT-MODFLOW and GRACE data. (b) Annual TWS obtained from SWAT-MODFLOW and GRACE data for the period 2003-2013.

simulations containing distributed models. The second important reason is perhaps due to the conceptual uncertainties contributed by different model inputs, lack of hydrogeological aquifers, not including all types of water data used for domestic and irrigation purposes, and the fixed boundaries for the model developed in this study.

5.10.2 Water Budgets and Fluxes

Surface and ground water fluxes and the resulting water budgets are discussed in terms of precipitation, evapotranspiration, runoff, and groundwater recharge for the TERB during the 1981-1997 years of simulation. The long-term mean monthly water budget components averaged for the entire watershed simulated in SWAT-MODEL are shown in Table 5.7. Mean annual precipitation in TERB ranges from 36.06 mm in March to just above 0.80mm in August. The higher magnitude of precipitation in the TERB is usually stored in as snow at the highlands, which contributes a major part of river flow after melting in spring season. The percentage of snow contribution to the runoff is counted for 55.00% during January in the TERB. Since large portion

of the watershed is located in semi-arid climate, the evapotranspiration causes the loss of a considerable percentage of the water budget from the river basin. Based on our analysis, higher evapotranspiration rates were noticed in the summer months (June-August). The simulated surface runoff from model (SURF Q) is not representative of the actual flow in stream network, rather it is the total runoff generated within the sub-basins without considering the channel losses and groundwater contributions. The mean monthly runoff ranges from 0.0 mm during summer to 2.26 mm during February. Further, SWAT-MODFLOW is also used to derive the groundwater components during each month of the simulation period. Results indicate the groundwater depletion was in the second half of the year starting from May, which might be resulted from the outflow from aquifer system during the dry season. The reduction in groundwater storage recovers during the first part of the winter months (i.e., November-December).

Table 5.7: Mean monthly water budgets averaged for all sub-basins in the TERB as simulated by SWAT-MODFLOW model during 1981−1997.

Month	RAIN (mm)	SNOW FALL (mm)	SURFQ (mm)	LATQ (mm)	WATER YIELD (mm)	ET (mm)	PET (mm)	GWSI (mm)
1	32.38	17.56	1.35	0.07	1.41	10.87	36.40	125.65
2	32.66	16.38	2.26	0.08	2.3	12.06	41.54	126.95
3	36.03	5.6	2.34	0.1	2.45	22.25	82.84	86.65
4	27.73	0.13	1.38	0.1	1.5	23.4	102.89	14.53
5	16.81	0	0.58	0.1	0.7	26.42	137.47	-17.12
6	4.44	0	0.03	0.07	0.11	28.51	184.74	-30.16
7	1.28	0	0	0.05	0.06	24.24	221.10	-40.50
8	0.81	0	0	0.04	0.04	7.52	212.43	-42.31
9	1.74	0	0	0.03	0.03	2.74	160.92	-34.78
10	16.1	0	0.12	0.03	0.15	6.56	108.89	-25.93
11	29.13	3.37	0.72	0.04	0.74	10.1	62.21	-17.14
12	33.81	14.53	1.15	0.06	1.22	10.06	40.76	-15.78
Total	232.92	57.57	9.93	0.77	10.71	184.73	1392.19	130.05

The spatial distribution of groundwater recharge over the domain of the watershed is an important input for MODFLOW model. Recharge for each HRU is

calculated in SWAT model and mapped to MODFLOW cells based on the percentage of HUR areas in each cell (Niswonger et al., 2014). The distribution of annual average recharge (mm) from SWAT model is shown in Figure 5.7. Five recharge zones were identified based on the recharge rates each zone receives including consolidated rocks, fractured rocks, alluvium, and mountain stream channels. The classification of the potential groundwater recharge rates was based on the developed stream network and geological formations presented in Figure 5.5, and it ranges from very low to very high in these zones, respectively. This figure indicates less recharge rates in the mountains located upper TERB, which is dominantly formed by consolidated rocks including dolomite and limestone, while higher recharge rates found at the lower parts of the TERB (i.e., the foothills), which mainly consist of permeable sedimentary.

5.10.3 Streamflow Simulation

The monthly streamflow simulated in coupled SWAT-MODFLOW is compared to the observed discharges at number of sub-basins for the period of 1981-1997, shown in Figure 5.8. The goodness of fit (GOF) measures of model efficiency including p- and r-factors, Nash-Sutcliff (NS), and Coefficient of determination (R^2) were evaluated for 10 stations located on Tigris River and 3 in Euphrates River. These GOF's metrics indicate that SWAT-MODFLOW model adequately simulates the observed hydrographs at monthly time scale (NS>0.5). The uncertainty of the model outputs was evaluated using two commonly statistical factors known as p- and r- factors. The p-factor represents the percentage of observation points bracketed by the prediction uncertainty band, and r-factor is the average thickness of the band divided by the standard deviation of the observed values showing the degree of uncertainty. Based on streamflow simulation analysis, the SWAT-MODFLOW generates acceptable un-

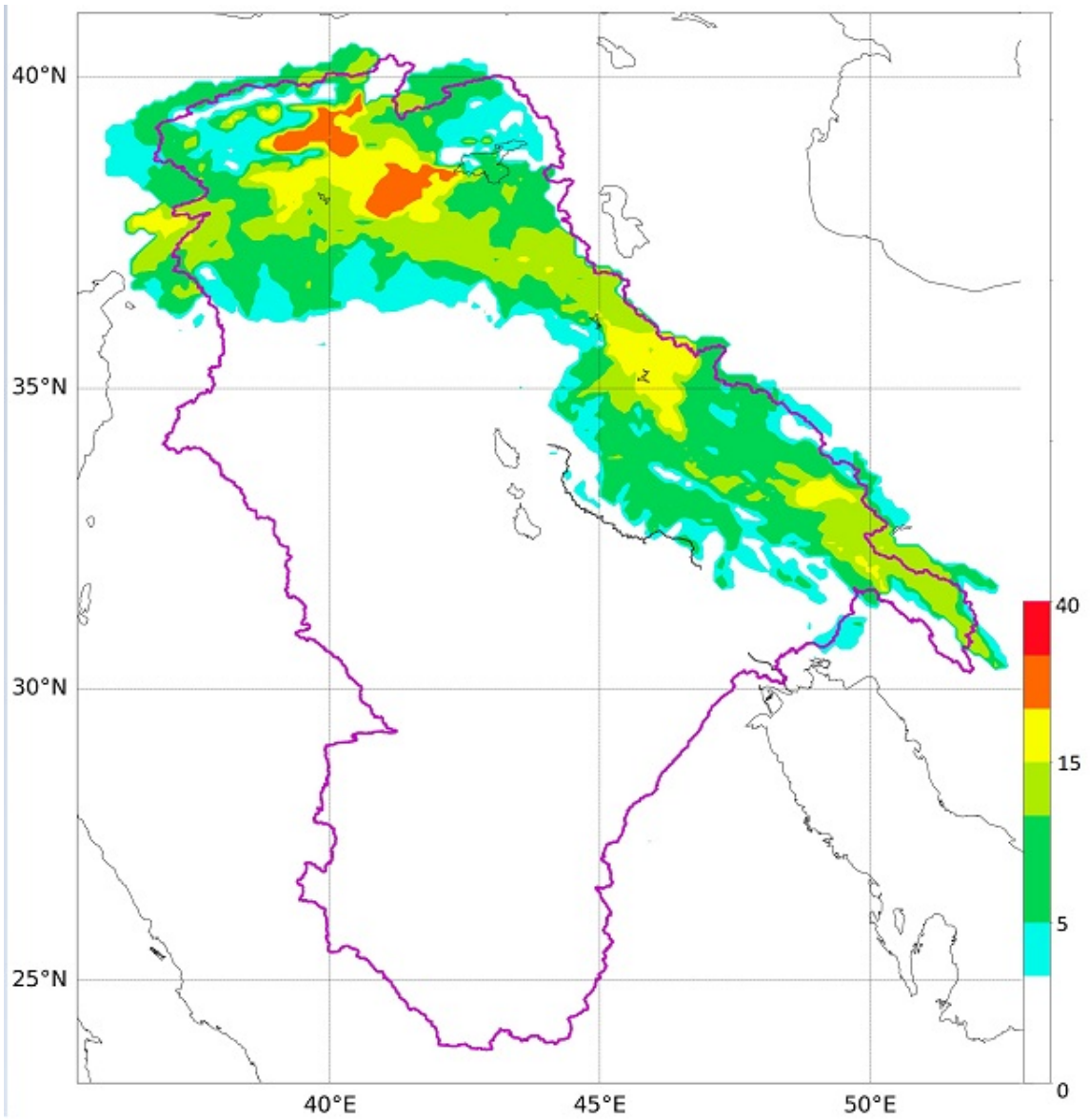

Figure 5.7: Long-term mean annual groundwater recharge (mm) for the TERB obtained from SWAT model for the period 1981-1997.

certainties with p-> 0.5 and r- around 1.0.

5.10.4 Simulation of Groundwater Discharge and Level

Groundwater recharge either comes from infiltration through the unsaturated zone or from seepage for tributary streams. After calibrating the coupled model with well observations, base flow, and GRACE satellite data in the selected domains, the simulated groundwater levels and discharges from transient flow simulation are presented in this section. The estimated groundwater discharge rates were exhibited for all stream reaches. These results are important because they demonstrate the spatiotemporal changes of surface and groundwater in the aquifer system. Figure 5.9 presents the average annual discharge (m^3d^{-1}) for each of the 419 reaches used in the model. As indicated in this figure, most of discharges were from rivers to aquifers, which indicates that for most aquifer systems water table elevation is less than water stages in most rivers. The highest annual flow rate loss from river segments occurred in lower reaches of the TERB -128,811 m^3y^{-1}, and lowest losses in upper part of the TERB with -969.00 m^3y^{-1}. This can be attributed the soil type of the shallow aquifers and the hydraulic conductivity at the interacted area near the stream beds used in MODFLOW model. It was also observed that the groundwater-surface interactions witness high special variations with in the watershed.

The average monthly groundwater discharge rates (m^3m^{-1}) for the entire river reaches in the TERB for the period 1981-1997 is shown in Figure 5.10. Monthly groundwater discharge results indicate a continuous gain for groundwater flow over the entire year. This figure also demonstrates that there is a remarkable groundwater flow increase during spring and summer months with the highest increase occurred in the month of May, whereas a decrease was noticed in winter months with the lowest

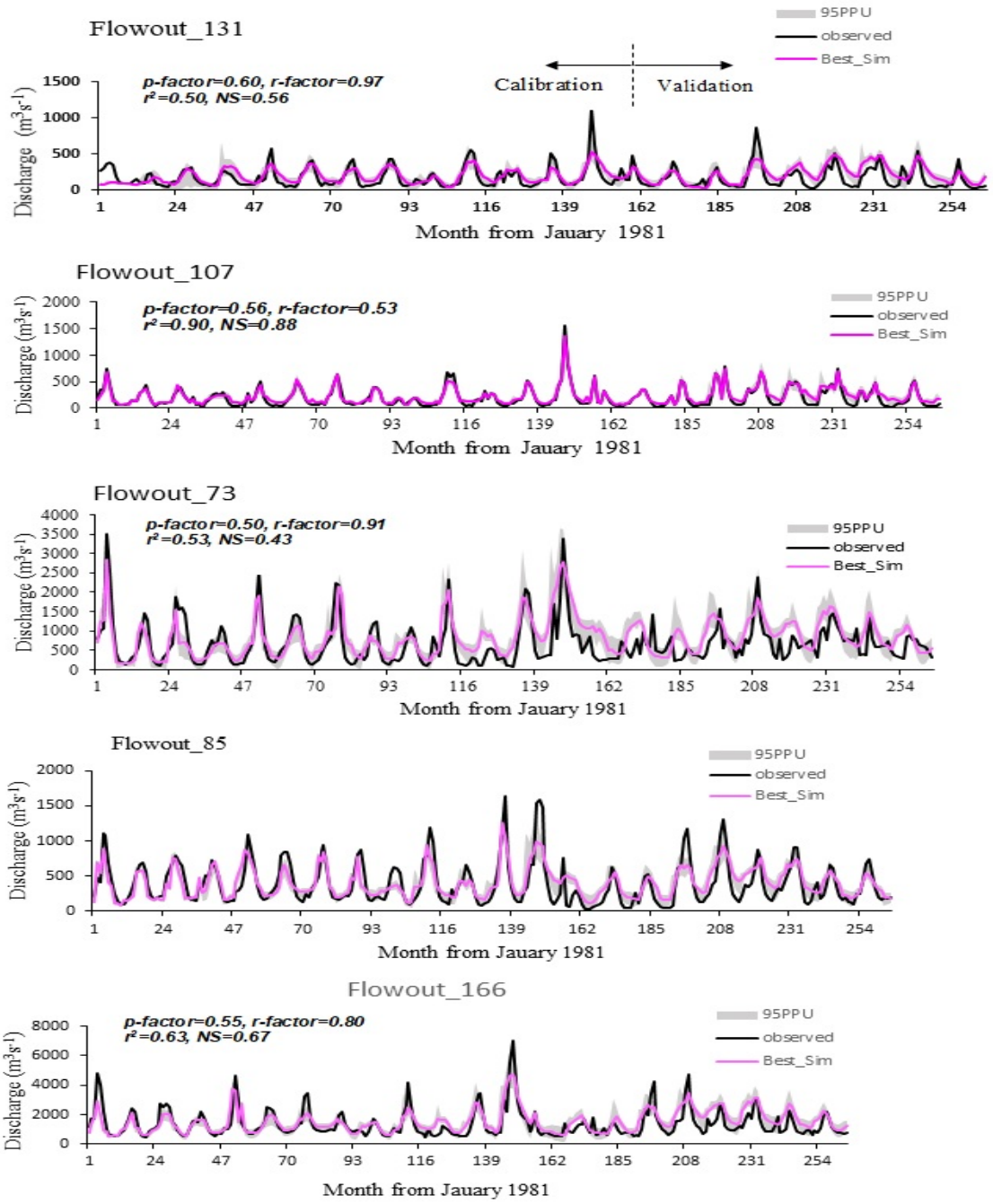

Figure 5.8: Hydrographs for selected stream gauge stations simulated from fully coupled SWAT-MODFLOW output showing the observed, the best simulation, and the 95% prediction uncertainty (95PPU) streamflow. At each station about two-third of the data was used for calibration and the remaining for validation.

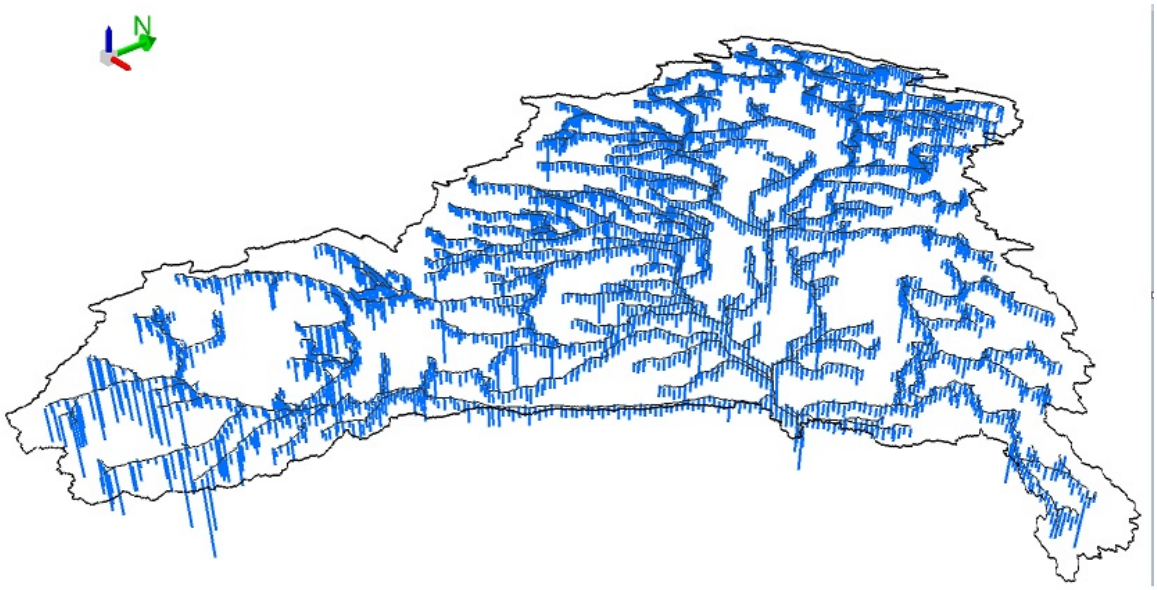

Figure 5.9: Long-term mean annual groundwater discharges (m^3y^{-1}) for the TERB obtained from SWAT-MODFLOW model for the period 1981-1997.

occurred in the month February. In addition, the spatial distribution over the months of each year from 1981 to 1997 is presented in Figure 5.10b. The groundwater discharge rates estimated to vary over the years with an average increase of groundwater movement in the year of 1988. These two figures suggest that sources of freshwater in the TERB are mostly attributed to the snow melt on the highlands which usually takes place in the spring months and gradually depletes in summer months. Because of that, the distribution of groundwater discharge varies quit constantly over the years during the entire period (Figure 5.10b).

The long-term mean annual basin average groundwater elevations for the simulation period (1981-1997) is shown in Figure 5.11. In general, the higher water table elevation (>2000 m) found in the upper parts of the TERB, and lower water level elevation close to few meters observed in southeast the TERB. Overall, the simulated groundwater elevations in SWAT-MODFLOW showed little higher than the actual

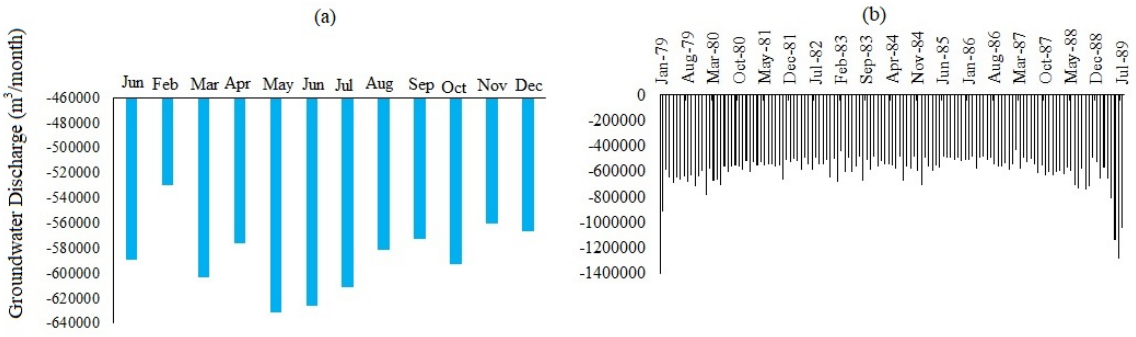

Figure 5.10: Monthly discharges between groundwater and streams (m^3/month) expressed as, (a) average of long-term mean monthly (b) mean monthly for the TERB in the period 1979-1997.

MODFLOW, which maybe due the different infiltration rates obtained from SWAT model. These findings align with the results of (Gannet et al., 2012; Bailey et al., 2016), where the SWAT model accounts for the spatiotemporal changes in precipitations patterns compared to the procedure used in traditional calibration MODFLOW approach which is independent of precipitation. The water table in the mountain areas were not well represented in the SWAT-MODEFLOW (mountain areas) due to the lack of the actual observations as well as lack of accurate representations of the boundary conditions.

5.11 Summary and Recommendations

The fully coupled SWAT-MODFLOW model was developed and validated against streamflow from a number of discharge stations, groundwater levels collected for two groups of wells in the north and south of the TERB, and total water storage anomalies derived from GRACE satellite data. The advantages of the coupled model is that it's ability to simulate spatiotemporal changes in hydrologic fluxes that occur between surface and subsurface systems, which profoundly impact the water and

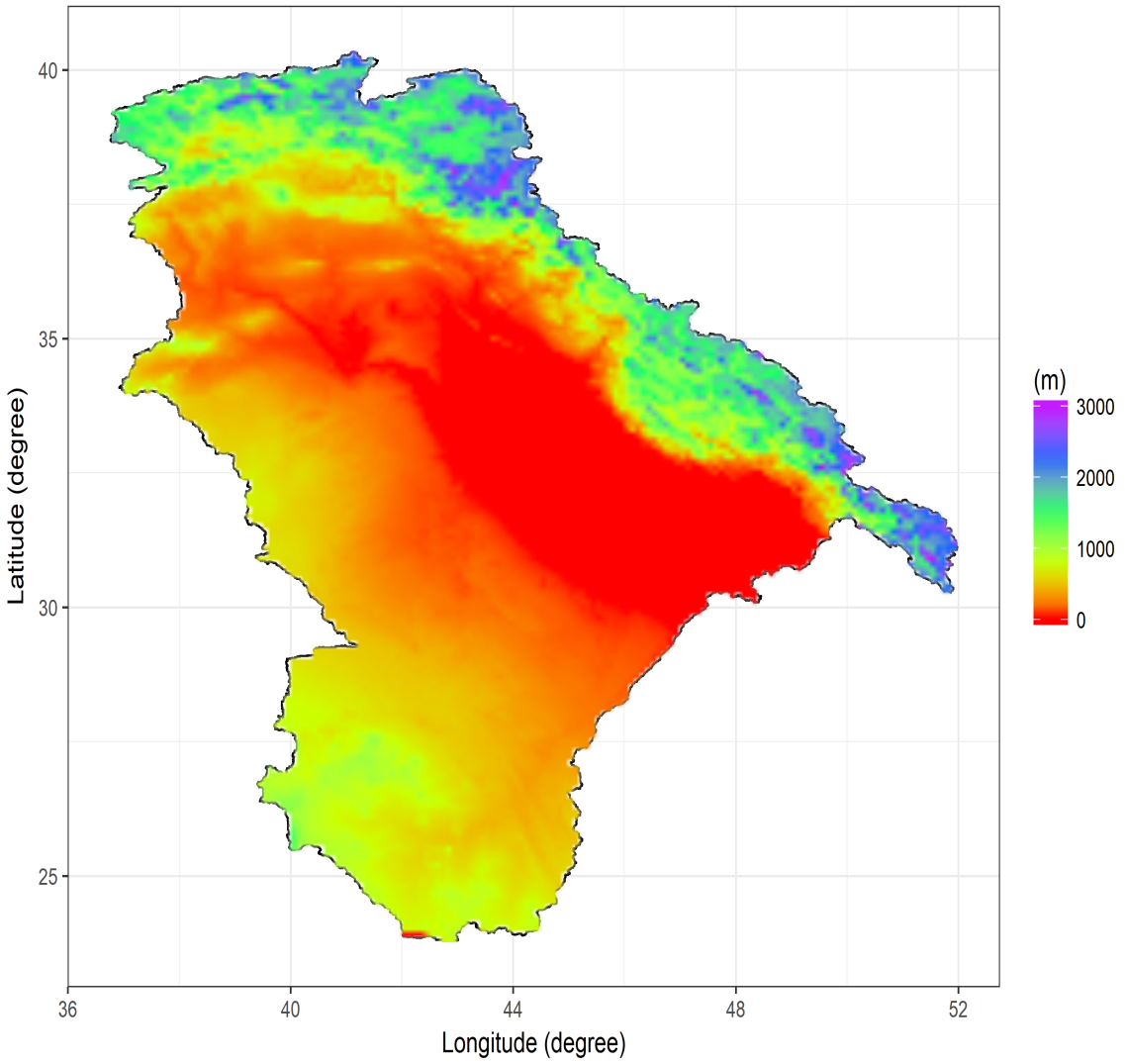

Figure 5.11: Long-term mean water table elevation for the entire study area simulated in SWAT-MODFLOW model for the period 1981-1997.

pollutants management in the watershed. The following findings can be summarized from this study:

a. The streamflow results simulated in coupled SWAT-MODFLOW model showed better base flow representation in comparison to SWAT model with an overall of 15% increase in goodness of fit measures.

b. Groundwater discharges are simulated on daily and monthly time steps at each streamflow cell. Groundwater discharge also displayed high spatial variability, with most of the locations showing loss from streamflow discharge to aquifers. Average annual groundwater discharge -7,078,872 m^3y^{-1}, with a remarkable increase in groundwater discharge after January 1987, which maybe due to construction of water storage infrastructure.

c. The infiltration rates from model showed higher rates in northern parts of the TERB especially in permeable sedimentary types spread across (the foothills to alluvial sediments towards central region of watershed).

d. Using satellite data to calibrate coupled SWAT-MODFLOW hydrological models seems encouraging where the total water storage from GRACE data and model are consistent where the coefficient of determination (R^2) is about 0.72.

The model findings can be extended in the future work to assess watershed management, and locate the potential hot spots of heavy nutrient mass fluxes, and investigate groundwater pumping from aquifers and its potential impact on water resources management.

Chapter 6

Conclusions and Recommendations

6.1 Research Summary and Conclusions

This dissertation has focused on developing methods for improving the spatial representations of rainfall to improve modeling framework in data scarce environment. Those methods have recently become feasible with the advancements of rainfall computations from different sources, soil moisture and ground water storages derived from satellite data. The proposed modeling framework was applied to a watershed located in semi-arid climate and lacking actual observations in space and time. This chapter sums the major outcomes from this dissertation and makes recommendations for the future work.

First objective-Trends in precipitation and air temperature: Changing land cover alters local to regional climate. For that, trends in annual and seasonal precipitation (air temperature) trends in 18 mega cities using multiple trend analysis methods were investigated for a selected top three mega cities from each of the six continents. Each city was further classified into urban and peri-urban areas according to their percentage of land cover imperviousness and the decadal change in air

temperature and precipitation as well as their possible relationship were evaluated.

The analysis developed in the first paper (**Chapter 2**) showed that the presence of serial correlation increase the possibly of observing significant trend in annual and seasonal air temperature than precipitation. The applications of Mann-Kendall technique with variance correction seemed to be more appropriate than classical and trend free pre-whitening. There were relatively higher trends in annual and seasonal air temperature than precipitation with a remarkable increase over urban areas than peri-urban areas. it was observed that urbanization (i.e., percentage of imperviousness surface) brings more warming to the majority of geographic locations considered in the analysis. This study is considered to be a part of the efforts to investigate the influence of urbanization on hydrological variables as well as climate extremes, which is important for allocating water resources for different urban sectors and to prevent over/under estimating urban pipe system designs.

Second objective-Precipitation bias correction: It is a common practice to use a single bias correction technique for correcting global coarse model outputs. For this paper, an approach of investigating bias correction technique of monthly precipitation that fits each rain-gauge station was proposed in the second paper (**Chapter 3**). This study indicates that multiple BCT's should be tested instead of applying a single BCT in a non-homogeneous climatic region. Further more, the scope of this study was implemented for data scarce area located in semi-arid climate, Iraq.

By comparing the five bias corrections methods, the quantile mapping and mean bias remove techniques performed well in comparison to multiplicative shift, standardized-reconstruction and linear regression approach. The quantile mapping technique performs well in comparison to the mean bias remove technique during wet season and associated months. This study profoundly suggests that instead of using a

single bias correction technique at different climatic regimes, multiple BCT's needs to be evaluated for identifying the appropriate methodology that suits local climatology.

Third objective-Hydrologic evaluation of precipitation data sources: The theme of evaluation from second paper has expanded in the third paper (**Chapter 4**) to compare four daily precipitation data sources and analyze their performance on simulating streamflow for Tigris River Basin which lacks ground-based precipitation data. The evaluated data sources were derived based on actual and satellite data consisted APHRODITE, CPC, MSWEP, and PERSIANN-CDR data sources. The precipitation data sources are evaluated against monthly streamflow at some subbasin locations simulated using SWAT model.

All four precipitation data sources have produced different biases when evaluated against actual rain gauges. Monthly streamflow estimated by SWAT model significantly improved using observed rainfall information in comparison to selected precipitation data sources because of the biases associated with each data source. From all data sources, APHRODITE (interpolated from dense number of gauges per grid) exhibited the best skills in representing the streamflow, while PERSIAN-CDR (satellite data) showed satisfactory performance at few locations in the Tigris River Basin. The streamflow estimated for Tigris River Basin using different forcing precipitations are highly heterogeneous.

Fourth objective-Surface and groundwater resources assessment: The verified daily precipitation data in the third paper (**Chapter 4**) was utilized to assess regional surface and subsurface interactions for Tigris and Euphrates River Basin, which is located in semi arid climate and lacking actual observed data, during the period 1981-1997. The model framework, developed in the fourth paper (**Chapter 5**), was designed using SWAT-MODFLOW and calibrated for discharge stations, groundwater levels collected for two groups of wells in the north and south of the TERB.

The SWAT-MODFLOW model was further calibrated against the total water storage anomalies which were derived from GRACE satellite data.

The streamflow results simulated in the coupled SWAT-MODFLOW model showed better base flow representation than only using SWAT model with an overall of 15% increase in goodness of fit measures. Groundwater discharges are simulated on daily and monthly time steps at each stream MODFLOW grid. Groundwater discharge also displayed high spatial variability, with almost all locations showing loss from streamflow discharge to aquifers. Average annual groundwater discharge - 7,078,872 m^3/year, with a remarkable increase in groundwater discharge after January 1987 (damming area). The infiltration rates from model showed higher rates northern parts of the watershed especially in permeable sedimentary (the foothills to alluvial sediments central region of watershed). The model findings can assess in watershed management, and it can be extended to locate the potential locations of heavy nutrient mass fluxes, groundwater pumping from aquifers.

The practical applications of this dissertation indicated that the use of the proposed modeling framework is capable of quantifying spatiotemporal hydroclimate variables on river basin scale, which ultimately can be used for improving watershed management and decisions making.

6.2 Recommendations for Future Work

The lack of the actual observed hydroclimate data such as well pumping data, water quality, and the water use by many sectors have made the job to understand the watershed management problems and monitor the most contaminated locations for remediations.more challenging. Therefore, examining multiple data sources has become a necessitated strategy in such watersheds. With the development of the

enhanced big data from remotely sensed concepts in the recent years, a promising research can be taken place to improve the spatiotemporal variations of surface and groundwater fluxes simulated from hydrological models on basin scales, which was the contribution in this dissertation. In future, this work can be extended to track the spatiotemporal changes of water quality on a catchment scale not only the flow and concentration of nutrients and pollutants moving with the stream water but also track their fate in subsurface system, incorporating the groundwater pumping from the aquifers. This allows to comprehensively understand the watershed management problems and monitor the locations of the most contaminated locations for remediations. Moreover, the improvement of groundwater contributions to the base flow components can be utilized in studying the unsaturated lateral flow component to improve streamflow quantity.

Appendices

Appendix A

Links for papers from Chapters 2 and 3

See the link below for Paper from Chapters 2:

https://link.springer.com/article/10.1007/s00477-015-1155-9

See the link below for Paper from Chapters 3:

https://link.springer.com/article/10.1007/s00704-017-2096-7

Bibliography

Abbaspour, K., Genuchten, M. v., Schulin, R., and Schläppi, E. (1997). A sequential uncertainty domain inverse procedure for estimating subsurface flow and transport parameters. *Water Resources Research*, 33(8):1879–1892.

Abbaspour, K., Johnson, C., and Van Genuchten, M. T. (2004). Estimating uncertain flow and transport parameters using a sequential uncertainty fitting procedure. *Vadose Zone Journal*, 3(4):1340–1352.

Abbaspour, K., Rouholahnejad, E., Vaghefi, S., Srinivasan, R., Yang, H., and Kløve, B. (2015). A continental-scale hydrology and water quality model for europe: Calibration and uncertainty of a high-resolution large-scale swat model. *Journal of Hydrology*, 524:733–752.

Abbaspour, K. C., Yang, J., Maximov, I., Siber, R., Bogner, K., Mieleitner, J., Zobrist, J., and Srinivasan, R. (2007). Modelling hydrology and water quality in the pre-alpine/alpine thur watershed using swat. *Journal of hydrology*, 333(2):413–430.

Acharya, N., Chattopadhyay, S., Mohanty, U., Dash, S., and Sahoo, L. (2013). On the bias correction of general circulation model output for indian summer monsoon. *Meteorological Applications*, 20(3):349–356.

Ajaaj, A. A., Mishra, A. K., and Khan, A. A. (2016). Comparison of bias correction techniques for gpcc rainfall data in semi-arid climate. *Stochastic environmental research and risk assessment*, 30(6):1659–1675.

Al-Suhili, R. H. and Khanbilvardi, R. (2014). Frequency analysis of the monthly rainfall data at sulaimania region, iraq. *American Journal of Engineering Research*, 3(5):212–222.

Alexander, L., Zhang, X., Peterson, T., Caesar, J., Gleason, B., Klein Tank, A., Haylock, M., Collins, D., Trewin, B., Rahimzadeh, F., et al. (2006). Global observed changes in daily climate extremes of temperature and precipitation. *Journal of Geophysical Research: Atmospheres*, 111(D5).

Alghazali, N. and Alawadi, D. A. H. (2014). Fitting statistical distributions of monthly rainfall for some iraqi stations. *Civil and Environmental Research*, 6(6):40–46.

Amisigo, B., Van de Giesen, N., Rogers, C., Andah, W., and Friesen, J. (2008). Monthly streamflow prediction in the volta basin of west africa: A siso narmax polynomial modelling. *Physics and Chemistry of the Earth, Parts A/B/C*, 33(1):141–150.

Andréassian, V., Le Moine, N., Perrin, C., Ramos, M.-H., Oudin, L., Mathevet, T., Lerat, J., and Berthet, L. (2012). All that glitters is not gold: the case of calibrating hydrological models. *Hydrological Processes*, 26(14):2206–2210.

Angel, S., Parent, J., Civco, D. L., Blei, A., and Potere, D. (2011). The dimensions of global urban expansion: Estimates and projections for all countries, 2000–2050. *Progress in Planning*, 75(2):53–107.

Argüeso, D., Di Luca, A., and Evans, J. P. (2016). Precipitation over urban areas in the western maritime continent using a convection-permitting model. *Climate dynamics*, 47(3-4):1143–1159.

Arnold, J., Allen, P., Muttiah, R., and Bernhardt, G. (1995). Automated base flow separation and recession analysis techniques. *Groundwater*, 33(6):1010–1018.

Arnold, J. G. and Fohrer, N. (2005). Swat2000: current capabilities and research opportunities in applied watershed modelling. *Hydrological processes*, 19(3):563–572.

Arnold, J. G., Moriasi, D. N., Gassman, P. W., Abbaspour, K. C., White, M. J., Srinivasan, R., Santhi, C., Harmel, R., Van Griensven, A., Van Liew, M. W., et al. (2012). Swat: Model use, calibration, and validation. *Transactions of the ASABE*, 55(4):1491–1508.

Arnold, J. G., Srinivasan, R., Muttiah, R. S., and Williams, J. R. (1998). Large area hydrologic modeling and assessment part i: model development. *JAWRA Journal of the American Water Resources Association*, 34(1):73–89.

Ashfaq, M., Bowling, L. C., Cherkauer, K., Pal, J. S., and Diffenbaugh, N. S. (2010). Influence of climate model biases and daily-scale temperature and precipitation events on hydrological impacts assessment: A case study of the united states. *Journal of Geophysical Research: Atmospheres (1984–2012)*, 115(D14).

Ashouri, H., Hsu, K.-L., Sorooshian, S., Braithwaite, D. K., Knapp, K. R., Cecil, L. D., Nelson, B. R., and Prat, O. P. (2015). Persiann-cdr: Daily precipitation climate data record from multisatellite observations for hydrological and climate studies. *Bulletin of the American Meteorological Society*, 96(1):69–83.

Bates, B. C. and Campbell, E. P. (2001). A markov chain monte carlo scheme for parameter estimation and inference in conceptual rainfall-runoff modeling. *Water resources research*, 37(4):937–947.

Beck, H. E., van Dijk, A. I., Levizzani, V., Schellekens, J., Miralles, D. G., Martens, B., and de Roo, A. (2017). Mswep: 3-hourly 0.25 global gridded precipitation (1979-2015) by merging gauge, satellite, and reanalysis data. *Hydrology and Earth System Sciences*, 21(1):589.

Becker, A., Finger, P., Meyer-Christoffer, A., Rudolf, B., Schamm, K., Schneider, U., and Ziese, M. (2013). A description of the global land-surface precipitation data products of the global precipitation climatology centre with sample applications including centennial (trend) analysis from 1901-present. *Earth System Science Data*, 5(1):71.

Behrangi, A., Khakbaz, B., Jaw, T. C., AghaKouchak, A., Hsu, K., and Sorooshian, S. (2011). Hydrologic evaluation of satellite precipitation products over a mid-size basin. *Journal of Hydrology*, 397(3):225–237.

Bentley, M. L., Ashley, W. S., and Stallins, J. A. (2010). Climatological radar delineation of urban convection for atlanta, georgia. *International Journal of Climatology*, 30(11):1589–1594.

Beven, K. J. (2011). *Rainfall-runoff modelling: the primer*. John Wiley & Sons.

Bitew, M. M., Gebremichael, M., Ghebremichael, L. T., and Bayissa, Y. A. (2012). Evaluation of high-resolution satellite rainfall products through streamflow simulation in a hydrological modeling of a small mountainous watershed in ethiopia. *Journal of Hydrometeorology*, 13(1):338–350.

Blasone, R.-S., Vrugt, J. A., Madsen, H., Rosbjerg, D., Robinson, B. A., and Zyvoloski, G. A. (2008). Generalized likelihood uncertainty estimation (glue) using adaptive markov chain monte carlo sampling. *Advances in Water Resources*, 31(4):630–648.

Boé, J., Terray, L., Habets, F., and Martin, E. (2007). Statistical and dynamical downscaling of the seine basin climate for hydro-meteorological studies. *International Journal of Climatology*, 27(12):1643–1655.

Bolvin, D. T., Adler, R. F., Huffman, G. J., Nelkin, E. J., and Poutiainen, J. P. (2009). Comparison of gpcp monthly and daily precipitation estimates with high-latitude gauge observations. *Journal of Applied Meteorology and Climatology*, 48(9):1843–1857.

Bozkurt, D. and Sen, O. L. (2011). Precipitation in the anatolian peninsula: sensitivity to increased ssts in the surrounding seas. *Climate dynamics*, 36(3-4):711–726.

Burian, S. J. and Shepherd, J. M. (2005). Effect of urbanization on the diurnal rainfall pattern in houston. *Hydrological Processes*, 19(5):1089–1103.

Changnon, S. A. and Westcott, N. E. (2002). Heavy rainstorms in chicago: Increasing frequency, altered impacts, and future implications. *JAWRA Journal of the American Water Resources Association*, 38(5):1467–1475.

Chen, M., Xie, P., Janowiak, J. E., and Arkin, P. A. (2002). Global land precipitation: A 50-yr monthly analysis based on gauge observations. *Journal of Hydrometeorology*, 3(3):249–266.

Chokngamwong, R. and Chiu, L. S. (2004). Comparisons of daily thailand rain gauge with gpcc and trmm satellite precipitation measurements. In *RMM INTERNATIONAL SCIENCE CONFERENCE*, volume 2.

Christensen, J. H., Hewitson, B., Busuioc, A., Chen, A., Gao, X., Held, R., Jones, R., Kolli, R. K., Kwon, W., Laprise, R., et al. (2007). Regional climate projections. In *Climate Change, 2007: The Physical Science Basis. Contribution of Working group I to the Fourth Assessment Report of the Intergovernmental Panel on Climate Change, University Press, Cambridge, Chapter 11*, pages 847–940.

Chu, T. and Shirmohammadi, A. (2004). Evaluation of the swat models hydrology component in the piedmont physiographic region of maryland. *Transactions of the ASAE*, 47(4):1057.

Crawford, S. L. (2006). Correlation and regression. *Circulation*, 114(19):2083–2088.

Di Luca, A., de Elía, R., and Laprise, R. (2015). Challenges in the quest for added value of regional climate dynamical downscaling. *Current Climate Change Reports*, 1(1):10–21.

Diem, J. E. and Mote, T. L. (2005). Interepochal changes in summer precipitation in the southeastern united states: evidence of possible urban effects near atlanta, georgia. *Journal of Applied Meteorology*, 44(5):717–730.

Dile, Y. T. and Srinivasan, R. (2014). Evaluation of cfsr climate data for hydrologic prediction in data-scarce watersheds: an application in the blue nile river basin. *JAWRA Journal of the American Water Resources Association*, 50(5):1226–1241.

Dixon, P. G. and Mote, T. L. (2003). Patterns and causes of atlanta's urban heat island–initiated precipitation. *Journal of Applied Meteorology*, 42(9):1273–1284.

Dosio, A. and Paruolo, P. (2011). Bias correction of the ensembles high-resolution climate change projections for use by impact models: evaluation on the present climate. *Journal of Geophysical Research: Atmospheres*, 116(D16).

Drápela, K., Drápelová, I., et al. (2011). Application of mann-kendall test and the sen's slope estimates for trend detection in deposition data from bílỳ kříž (beskydy mts., the czech republic) 1997-2010. *Beskydy*, 4(2):133–146.

Duda, R. O., Hart, P. E., and Stork, D. G. (2012). *Pattern classification*. John Wiley & Sons.

Earls, J. and Dixon, B. (2008). A comparison of swat model-predicted potential evapotranspiration using real and modeled meteorological data. *Vadose Zone Journal*, 7(2):570–580.

Faramarzi, M., Abbaspour, K. C., Schulin, R., and Yang, H. (2009). Modelling blue and green water resources availability in iran. *Hydrological Processes*, 23(3):486–501.

Faurès, J.-M., Goodrich, D., Woolhiser, D. A., and Sorooshian, S. (1995). Impact of small-scale spatial rainfall variability on runoff modeling. *Journal of Hydrology*, 173(1-4):309–326.

Fowler, H. J., Blenkinsop, S., and Tebaldi, C. (2007). Linking climate change modelling to impacts studies: recent advances in downscaling techniques for hydrological modelling. *International journal of climatology*, 27(12):1547–1578.

Franz, K. J., Butcher, P., and Ajami, N. K. (2010). Addressing snow model uncertainty for hydrologic prediction. *Advances in Water Resources*, 33(8):820–832.

Frenken, K. et al. (2009). Irrigation in the middle east region in figures aquastat survey-2008. *Water Reports*, (34).

Fujibe, F. (2009). Detection of urban warming in recent temperature trends in japan. *International Journal of Climatology*, 29(12):1811–1822.

Fuka, D. R., Walter, M. T., MacAlister, C., Degaetano, A. T., Steenhuis, T. S., and Easton, Z. M. (2014). Using the climate forecast system reanalysis as weather input data for watershed models. *Hydrological Processes*, 28(22):5613–5623.

Funk, C., Nicholson, S. E., Landsfeld, M., Klotter, D., Peterson, P., and Harrison, L. (2015). The centennial trends greater horn of africa precipitation dataset. *Scientific data*, 2:150050.

Galbiati, L., Bouraoui, F., Elorza, F., and Bidoglio, G. (2006). Modeling diffuse pollution loading into a mediterranean lagoon: development and application of an integrated surface–subsurface model tool. *Ecological Modelling*, 193(1):4–18.

Gallagher, M. R. and Doherty, J. (2007). Parameter interdependence and uncertainty induced by lumping in a hydrologic model. *Water Resources Research*, 43(5).

Ganeshan, M., Murtugudde, R., and Imhoff, M. L. (2013). A multi-city analysis of the uhi-influence on warm season rainfall. *Urban Climate*, 6:1–23.

Gassman, P. W., Reyes, M. R., Green, C. H., and Arnold, J. G. (2007). The soil and water assessment tool: historical development, applications, and future research directions. *Transactions of the ASABE*, 50(4):1211–1250.

Gudmundsson, L., Bremnes, J., Haugen, J., and Engen-Skaugen, T. (2012). Downscaling rcm precipitation to the station scale using statistical transformations–a comparison of methods. *Hydrology and Earth System Sciences*, 16(9):3383–3390.

Gupta, H. V., Sorooshian, S., and Yapo, P. O. (1999). Status of automatic calibration for hydrologic models: Comparison with multilevel expert calibration. *Journal of Hydrologic Engineering*, 4(2):135–143.

Haan, C. T. (2002). *Statistical methods in hydrology*. The Iowa State University Press.

Hamed, K. H. and Rao, A. R. (1998). A modified mann-kendall trend test for autocorrelated data. *Journal of Hydrology*, 204(1-4):182–196.

Han, L., Xu, Y., Pan, G., Deng, X., Hu, C., Xu, H., and Shi, H. (2015). Changing properties of precipitation extremes in the urban areas, yangtze river delta, china, during 1957–2013. *Natural Hazards*, 79(1):437–454.

Harbaugh, A. W., Banta, E. R., Hill, M. C., and McDonald, M. G. (2000). Modflow-2000, the u. s. geological survey modular ground-water model-user guide to modularization concepts and the ground-water flow process. *Open-file Report. U. S. Geological Survey*, (92):134.

Hijmans, R. J., Cameron, S. E., Parra, J. L., Jones, P. G., and Jarvis, A. (2005). Very high resolution interpolated climate surfaces for global land areas. *International journal of climatology*, 25(15):1965–1978.

Hu, C., Xu, Y., Han, L., Yang, L., and Xu, G. (2016). Long-term trends in daily precipitation over the yangtze river delta region during 1960–2012, eastern china. *Theoretical and applied climatology*, 125(1-2):131–147.

Hu, Y. and Jia, G. (2010). Influence of land use change on urban heat island derived from multi-sensor data. *International Journal of Climatology*, 30(9):1382–1395.

Huffman, G. J., Adler, R. F., Bolvin, D. T., and Gu, G. (2009). Improving the global precipitation record: Gpcp version 2.1. *Geophysical Research Letters*, 36(17).

Ines, A. V. and Hansen, J. W. (2006). Bias correction of daily gcm rainfall for crop simulation studies. *Agricultural and forest meteorology*, 138(1):44–53.

Inoue, T. and Kimura, F. (2007). Numerical experiments on fair-weather clouds forming over the urban area in northern tokyo. *SOLA*, 3:125–128.

Issa, I. E., Al-Ansari, N., Sherwany, G., and Knutsson, S. (2014). Expected future of water resources within tigris–euphrates rivers basin, iraq. *Journal of Water Resource and Protection*, 6(5):421–432.

Jassim, S. Z. and Goff, J. C. (2006). *Geology of Iraq*. DOLIN, sro, distributed by Geological Society of London.

Jeong, D., St-Hilaire, A., Ouarda, T., and Gachon, P. (2012). Comparison of transfer functions in statistical downscaling models for daily temperature and precipitation over canada. *Stochastic environmental research and risk assessment*, 26(5):633–653.

Jiang, S., Ren, L., Hong, Y., Yong, B., Yang, X., Yuan, F., and Ma, M. (2012). Comprehensive evaluation of multi-satellite precipitation products with a dense rain gauge network and optimally merging their simulated hydrological flows using the bayesian model averaging method. *Journal of Hydrology*, 452:213–225.

Johnson, F. and Sharma, A. (2011). Accounting for interannual variability: A comparison of options for water resources climate change impact assessments. *Water Resources Research*, 47(4).

Jones, C., Sultan, M., Yan, E., Milewski, A., Hussein, M., Al-Dousari, A., Al-Kaisy, S., and Becker, R. (2008). Hydrologic impacts of engineering projects on the tigris–euphrates system and its marshlands. *Journal of Hydrology*, 353(1):59–75.

Karabulut, M., Gürbüz, M., and Korkmaz, H. (2008). Precipitation and temperature trend analyses in samsun. *Journal International Environmental Application & Science*, 3(5):399–408.

Karmeshu, N. (2012). Trend detection in annual temperature & precipitation using the mann kendall test–a case study to assess climate change on select states in the northeastern united states.

Kaufmann, R. K., Seto, K. C., Schneider, A., Liu, Z., Zhou, L., and Wang, W. (2007). Climate response to rapid urban growth: evidence of a human-induced precipitation deficit. *Journal of Climate*, 20(10):2299–2306.

Keggenhoff, I., Elizbarashvili, M., Amiri-Farahani, A., and King, L. (2014). Trends in daily temperature and precipitation extremes over georgia, 1971–2010. *Weather and Climate Extremes*, 4:75–85.

Kendall, M. (1975). Rank correlation methods. griffin & co, london. Technical report, ISBN 0-85264-199-0.

Kephe, P. N., Petja, B. M., and Kabanda, T. A. (2016). Spatial and inter-seasonal behaviour of rainfall in the soutpansberg region of south africa as attributed to the changing climate. *Theoretical and applied climatology*, 126(1-2):233–245.

Kharin, V. V. and Zwiers, F. W. (2002). Climate predictions with multimodel ensembles. *Journal of Climate*, 15(7):793–799.

Kharol, S. K., Kaskaoutis, D., Sharma, A. R., and Singh, R. P. (2013). Long-term (1951–2007) rainfall trends around six indian cities: current state, meteorological, and urban dynamics. *Advances in Meteorology*, 2013.

Kibaroğlu, A. (2002). *Building a regime for the waters of the Euphrates-Tigris river basin*, volume 7. Martinus Nijhoff Publishers.

Krishnamurti, T. N., Kishtawal, C., Zhang, Z., LaRow, T., Bachiochi, D., Williford, E., Gadgil, S., and Surendran, S. (2000). Multimodel ensemble forecasts for weather and seasonal climate. *Journal of Climate*, 13(23):4196–4216.

Kug, J.-S. and Ahn, M.-S. (2013). Impact of urbanization on recent temperature and precipitation trends in the korean peninsula. *Asia-Pacific Journal of Atmospheric Sciences*, 49(2):151–159.

Kumar, S., Merwade, V., Kam, J., and Thurner, K. (2009). Streamflow trends in indiana: effects of long term persistence, precipitation and subsurface drains. *Journal of Hydrology*, 374(1):171–183.

Kundzewicz, Z. W., Mata, L. J., Arnell, N., Doll, P., Kabat, P., Jimenez, B., Miller, K., Oki, T., Zekai, S., and Shiklomanov, I. (2007). Freshwater resources and their management.

Kusaka, H., Nawata, K., Suzuki-Parker, A., Takane, Y., and Furuhashi, N. (2014). Mechanism of precipitation increase with urbanization in tokyo as revealed by ensemble climate simulations. *Journal of Applied Meteorology and Climatology*, 53(4):824–839.

Latham, J., Cumani, R., Rosati, I., and Bloise, M. (2014). Global land cover share (glc-share) database beta-release version 1.0-2014. *FAO: Rome, Italy*.

Legates, D. R. and McCabe, G. J. (1999). Evaluating the use of goodness-of-fit measures in hydrologic and hydroclimatic model validation. *Water resources research*, 35(1):233–241.

Li, C., Sinha, E., Horton, D. E., Diffenbaugh, N. S., and Michalak, A. M. (2014). Joint bias correction of temperature and precipitation in climate model simulations. *Journal of Geophysical Research: Atmospheres*, 119(23).

Li, H., Sheffield, J., and Wood, E. F. (2010). Bias correction of monthly precipitation and temperature fields from intergovernmental panel on climate change ar4 models using equidistant quantile matching. *Journal of Geophysical Research: Atmospheres*, 115(D10).

Li, H., Zhang, Y., Chiew, F. H., and Xu, S. (2009). Predicting runoff in ungauged catchments by using xinanjiang model with modis leaf area index. *Journal of Hydrology*, 370(1):155–162.

Lipper, L., Raney, T., et al. (2007). The state of food and agriculture, 2007: paying farmers for environmental services. rome. *Food & Agricultural Org.*

Liu, S., Chen, M., and Zhuang, Q. (2014). Aerosol effects on global land surface energy fluxes during 2003–2010. *Geophysical Research Letters*, 41(22):7875–7881.

Lu, D. and Weng, Q. (2006). Use of impervious surface in urban land-use classification. *Remote Sensing of Environment*, 102(1):146–160.

Luo, Y., Liu, S., Fu, S., Liu, J., Wang, G., and Zhou, G. (2008). Trends of precipitation in beijiang river basin, guangdong province, china. *Hydrological Processes*, 22(13):2377–2386.

Ly, S., Charles, C., and Degré, A. (2013). Different methods for spatial interpolation of rainfall data for operational hydrology and hydrological modeling at watershed scale. a review. *Biotechnologie, Agronomie, Société et Environnement*, 17(2):392.

Malinowski, J. C. (2002). Iraq: A geography.

Mann, H. B. (1945). Nonparametric tests against trend. *Econometrica: Journal of the Econometric Society*, pages 245–259.

Maraun, D., Wetterhall, F., Ireson, A., Chandler, R., Kendon, E., Widmann, M., Brienen, S., Rust, H., Sauter, T., Themeßl, M., et al. (2010). Precipitation downscaling under climate change: Recent developments to bridge the gap between dynamical models and the end user. *Reviews of Geophysics*, 48(3).

Marghany, M., Hasab, H. A., Mansor, S., and Shariff, A. R. B. M. (2016). Developing hydrological model for water quality in iraq marshes zone using landsat-tm. In *IOP Conference Series: Earth and Environmental Science*, volume 37, page 012073. IOP Publishing.

Markstrom, S. L. and Hay, L. E. (2009). Integrated watershed scale response to climate change for selected basins across the united states. *Water Resources Impact*, 11(2):8–10.

Maurer, E. P. and Hidalgo, H. G. (2008). Utility of daily vs. monthly large-scale climate data: an intercomparison of two statistical downscaling methods.

McCallum, A. M., Andersen, M. S., Giambastiani, B., Kelly, B. F., and Ian Acworth, R. (2013). River–aquifer interactions in a semi-arid environment stressed by groundwater abstraction. *Hydrological Processes*, 27(7):1072–1085.

Miao, C., Ashouri, H., Hsu, K.-L., Sorooshian, S., and Duan, Q. (2015). Evaluation of the persiann-cdr daily rainfall estimates in capturing the behavior of extreme precipitation events over china. *Journal of Hydrometeorology*, 16(3):1387–1396.

Mishra, A. and Singh, V. P. (2009). Analysis of drought severity-area-frequency curves using a general circulation model and scenario uncertainty. *Journal of Geophysical Research: Atmospheres*, 114(D6).

Mishra, A. K. and Coulibaly, P. (2009). Developments in hydrometric network design: A review. *Reviews of Geophysics*, 47(2).

Mishra, A. K., Ines, A. V., Singh, V. P., and Hansen, J. W. (2013). Extraction of information content from stochastic disaggregation and bias corrected downscaled precipitation variables for crop simulation. *Stochastic environmental research and risk assessment*, 27(2):449–457.

Mishra, A. K. and Singh, V. P. (2010). Changes in extreme precipitation in texas. *Journal of Geophysical Research: Atmospheres*, 115(D14).

Mishra, A. K., Singh, V. P., and Özger, M. (2011). Seasonal streamflow extremes in texas river basins: Uncertainty, trends, and teleconnections. *Journal of Geophysical Research: Atmospheres*, 116(D8).

Moriasi, D. N., Arnold, J. G., Van Liew, M. W., Bingner, R. L., Harmel, R. D., and Veith, T. L. (2007). Model evaluation guidelines for systematic quantification of accuracy in watershed simulations. *Transactions of the ASABE*, 50(3):885–900.

Nash, J. E. and Sutcliffe, J. V. (1970). River flow forecasting through conceptual models part ia discussion of principles. *Journal of hydrology*, 10(3):282–290.

Nicholson, S. E., Some, B., McCollum, J., Nelkin, E., Klotter, D., Berte, Y., Diallo, B., Gaye, I., Kpabeba, G., Ndiaye, O., et al. (2003). Validation of trmm and other rainfall estimates with a high-density gauge dataset for west africa. part ii: Validation of trmm rainfall products. *Journal of Applied Meteorology*, 42(10):1355–1368.

Niyogi, D., Alapaty, K., Raman, S., and Chen, F. (2009). Development and evaluation of a coupled photosynthesis-based gas exchange evapotranspiration model (gem) for mesoscale weather forecasting applications. *Journal of Applied Meteorology and Climatology*, 48(2):349–368.

O'Gorman, P. A. and Schneider, T. (2009). The physical basis for increases in precipitation extremes in simulations of 21st-century climate change. *Proceedings of the National Academy of Sciences*, 106(35):14773–14777.

Pan, J. and van den Dool, H. (1998). Extended-range probability forecasts based on dynamical model output. *Weather and Forecasting*, 13(4):983–996.

Piani, C., Haerter, J., and Coppola, E. (2010a). Statistical bias correction for daily precipitation in regional climate models over europe. *Theoretical and Applied Climatology*, 99(1-2):187–192.

Piani, C., Weedon, G., Best, M., Gomes, S., Viterbo, P., Hagemann, S., and Haerter, J. (2010b). Statistical bias correction of global simulated daily precipitation and temperature for the application of hydrological models. *Journal of Hydrology*, 395(3):199–215.

Pingale, S. M., Khare, D., Jat, M. K., and Adamowski, J. (2014). Spatial and temporal trends of mean and extreme rainfall and temperature for the 33 urban centers of the arid and semi-arid state of rajasthan, india. *Atmospheric Research*, 138:73–90.

Prakash, S., Mahesh, C., and Gairola, R. M. (2011). Large-scale precipitation estimation using kalpana-1 ir measurements and its validation using gpcp and gpcc data. *Theoretical and applied climatology*, 106(3-4):283–293.

Prudhomme, C., Reynard, N., and Crooks, S. (2002). Downscaling of global climate models for flood frequency analysis: where are we now? *Hydrological processes*, 16(6):1137–1150.

Rajsekhar, D., Singh, V. P., and Mishra, A. K. (2015). Integrated drought causality, hazard, and vulnerability assessment for future socioeconomic scenarios: An information theory perspective. *Journal of Geophysical Research: Atmospheres*, 120(13):6346–6378.

Rassam, D. W., Peeters, L., Pickett, T., Jolly, I., and Holz, L. (2013). Accounting for surface–groundwater interactions and their uncertainty in river and groundwater models: A case study in the namoi river, australia. *Environmental modelling & software*, 50:108–119.

Raziei, T., Bordi, I., Pereira, L., and Sutera, A. (2010). Space-time variability of hydrological drought and wetness in iran using ncep/ncar and gpcc datasets. *Hydrology and Earth System Sciences*, 14(10):1919.

Raziei, T., Bordi, I., and Pereira, L. S. (2011). An application of gpcc and ncep/ncar datasets for drought variability analysis in iran. *Water resources management*, 25(4):1075–1086.

Rodda, J. C. (1995a). Guessing or assessing the world's water resources? *Water and Environment Journal*, 9(4):360–368.

Rodda, J. C. (1995b). Whither world water? *JAWRA Journal of the American Water Resources Association*, 31(1):1–7.

Rojas, R., Feyen, L., Dosio, A., and Bavera, D. (2011). Improving pan-european hydrological simulation of extreme events through statistical bias correction of rcm-driven climate simulations. *Hydrology and Earth System Sciences*, 15(8):2599.

Rosenzweig, C., Solecki, W. D., Hammer, S. A., and Mehrotra, S. (2011). *Climate change and cities: First assessment report of the urban climate change research network*. Cambridge University Press.

Rostamian, R., Jaleh, A., Afyuni, M., Mousavi, S. F., Heidarpour, M., Jalalian, A., and Abbaspour, K. C. (2008). Application of a swat model for estimating runoff and sediment in two mountainous basins in central iran. *Hydrological Sciences Journal*, 53(5):977–988.

Saleh, D. K. (2010). Stream gage descriptions and streamflow statistics for sites in the tigris river and euphrates river basins, iraq. Technical report, US Geological Survey.

Santhi, C., Arnold, J. G., Williams, J. R., Dugas, W. A., Srinivasan, R., and Hauck, L. M. (2001). Validation of the swat model on a large rwer basin with point and nonpoint sources. *JAWRA Journal of the American Water Resources Association*, 37(5):1169–1188.

Schneider, U., Becker, A., Finger, P., Meyer-Christoffer, A., Ziese, M., and Rudolf, B. (2014). Gpcc's new land surface precipitation climatology based on quality-controlled in situ data and its role in quantifying the global water cycle. *Theoretical and Applied Climatology*, 115(1-2):15–40.

Schneider, U., Fuchs, T., Meyer-Christoffer, A., and Rudolf, B. (2008). Global precipitation analysis products of the gpcc. *Global Precipitation Climatology Centre (GPCC), DWD, Internet Publikation*, 112.

Schuol, J. and Abbaspour, K. (2006). Calibration and uncertainty issues of a hydrological model (swat) applied to west africa. *Advances in geosciences*, 9:137–143.

Seto, K. C., Fragkias, M., Güneralp, B., and Reilly, M. K. (2011). A meta-analysis of global urban land expansion. *PloS one*, 6(8):e23777.

Sexton, A. M. (2007). *Evaluation of SWAT model applicability for waterbody impairment identification and TMDL analysis*. University of Maryland, College Park.

Shahid, S., Wang, X.-J., Harun, S. B., Shamsudin, S. B., Ismail, T., and Minhans, A. (2016). Climate variability and changes in the major cities of bangladesh: observations, possible impacts and adaptation. *Regional environmental change*, 16(2):459–471.

Shahin, M. (2007). *Water resources and hydrometeorology of the Arab region*, volume 59. Springer Science & Business Media.

Shao, Q. and Li, M. (2013). An improved statistical analogue downscaling procedure for seasonal precipitation forecast. *Stochastic environmental research and risk assessment*, 27(4):819–830.

Sharma, C. S., Panda, S. N., Pradhan, R. P., Singh, A., and Kawamura, A. (2016). Precipitation and temperature changes in eastern india by multiple trend detection methods. *Atmospheric Research*, 180:211–225.

Shepherd, J. M. (2006). Evidence of urban-induced precipitation variability in arid climate regimes. *Journal of Arid Environments*, 67(4):607–628.

Shepherd, J. M., Pierce, H., and Negri, A. J. (2002). Rainfall modification by major urban areas: Observations from spaceborne rain radar on the trmm satellite. *Journal of Applied Meteorology*, 41(7):689–701.

Sidike, A., Chen, X., Liu, T., Durdiev, K., and Huang, Y. (2016). Investigating alternative climate data sources for hydrological simulations in the upstream of the amu darya river. *Water*, 8(10):441.

Siebert, S., Burke, J., Faures, J.-M., Frenken, K., Hoogeveen, J., Döll, P., and Portmann, F. T. (2010). Groundwater use for irrigation–a global inventory. *Hydrology and Earth System Sciences*, 14(10):1863–1880.

Singh, J., Knapp, H. V., Arnold, J., and Demissie, M. (2005). Hydrological modeling of the iroquois river watershed using hspf and swat. *JAWRA Journal of the American Water Resources Association*, 41(2):343–360.

Song, X., Zhang, J., AghaKouchak, A., Roy, S. S., Xuan, Y., Wang, G., He, R., Wang, X., and Liu, C. (2014). Rapid urbanization and changes in spatiotemporal characteristics of precipitation in beijing metropolitan area. *Journal of Geophysical Research: Atmospheres*, 119(19).

Sophocleous, M., Koelliker, J., Govindaraju, R., Birdie, T., Ramireddygari, S., and Perkins, S. (1999). Integrated numerical modeling for basin-wide water management: The case of the rattlesnake creek basin in south-central kansas. *Journal of Hydrology*, 214(1):179–196.

Sorooshian, S., Hsu, K.-L., Gao, X., Gupta, H. V., Imam, B., and Braithwaite, D. (2000). Evaluation of persiann system satellite–based estimates of tropical rainfall. *Bulletin of the American Meteorological Society*, 81(9):2035–2046.

Strauch, M., Bernhofer, C., Koide, S., Volk, M., Lorz, C., and Makeschin, F. (2012). Using precipitation data ensemble for uncertainty analysis in swat streamflow simulation. *Journal of Hydrology*, 414:413–424.

Sudicky, E. A., Vanderkwaak, J. E., Jones, J. P., Keizer, J. P., Mclaren, R. G., and Matanga, G. B. (2003). Fully-integrated modelling of surface and subsurface water flow and solute transport: Model overview and application. In *Developments in Water Science*, volume 50, pages 313–318. Elsevier.

Sulis, M., Meyerhoff, S. B., Paniconi, C., Maxwell, R. M., Putti, M., and Kollet, S. J. (2010). A comparison of two physics-based numerical models for simulating surface water–groundwater interactions. *Advances in Water Resources*, 33(4):456–467.

Sun, Q., Kong, D., Miao, C., Duan, Q., Yang, T., Ye, A., Di, Z., and Gong, W. (2014). Variations in global temperature and precipitation for the period of 1948 to 2010. *Environmental monitoring and assessment*, 186(9):5663–5679.

Sunyer, M., Madsen, H., and Ang, P. (2012). A comparison of different regional climate models and statistical downscaling methods for extreme rainfall estimation under climate change. *Atmospheric Research*, 103:119–128.

Taesombat, W. and Sriwongsitanon, N. (2009). Areal rainfall estimation using spatial interpolation techniques. *Science Asia*, 35(3):268–275.

Tanarhte, M., Hadjinicolaou, P., and Lelieveld, J. (2012). Intercomparison of temperature and precipitation data sets based on observations in the mediterranean and the middle east. *Journal of Geophysical Research: Atmospheres*, 117(D12).

Tateishi, R., Uriyangqai, B., Al-Bilbisi, H., Ghar, M. A., Tsend-Ayush, J., Kobayashi, T., Kasimu, A., Hoan, N. T., Shalaby, A., Alsaaideh, B., et al. (2011). Production of global land cover data–glcnmo. *International Journal of Digital Earth*, 4(1):22–49.

Tayanc, M. and Toros, H. (1997). Urbanization effects on regional climate change in the case of four large cities of turkey. *Climatic Change*, 35(4):501–524.

Teutschbein, C. and Seibert, J. (2012). Bias correction of regional climate model simulations for hydrological climate-change impact studies: Review and evaluation of different methods. *Journal of Hydrology*, 456:12–29.

Thiemig, V., Rojas, R., Zambrano-Bigiarini, M., and De Roo, A. (2013). Hydrological evaluation of satellite-based rainfall estimates over the volta and baro-akobo basin. *Journal of Hydrology*, 499:324–338.

Tigrek, S. and Kibaroglu, A. (2011). Strategic role of water resources for turkey. In *Turkey's Water Policy*, pages 27–42. Springer.

Trenberth, K. E. and Caron, J. M. (2000). The southern oscillation revisited: Sea level pressures, surface temperatures, and precipitation. *Journal of Climate*, 13(24):4358–4365.

Tuo, Y., Duan, Z., Disse, M., and Chiogna, G. (2016). Evaluation of precipitation input for swat modeling in alpine catchment: A case study in the adige river basin (italy). *Science of the Total Environment*, 573:66–82.

Van Griensven, A., Meixner, T., Grunwald, S., Bishop, T., Diluzio, M., and Srinivasan, R. (2006). A global sensitivity analysis tool for the parameters of multivariable catchment models. *Journal of hydrology*, 324(1):10–23.

Velpuri, N. and Senay, G. (2013). Analysis of long-term trends (1950–2009) in precipitation, runoff and runoff coefficient in major urban watersheds in the united states. *Environmental Research Letters*, 8(2):024020.

Voss, K. A., Famiglietti, J. S., Lo, M., Linage, C., Rodell, M., and Swenson, S. C. (2013). Groundwater depletion in the middle east from grace with implications for transboundary water management in the tigris-euphrates-western iran region. *Water resources research*, 49(2):904–914.

Vrugt, J. A. and Bouten, W. (2002). Validity of first-order approximations to describe parameter uncertainty in soil hydrologic models. *Soil Science Society of America Journal*, 66(6):1740–1751.

Vu, M., Raghavan, S. V., and Liong, S. Y. (2012). Swat use of gridded observations for simulating runoff-a vietnam river basin study. *Hydrology and Earth System Sciences*, 16(8):2801.

Wang, X. and Melesse, A. (2005). Evaluation of the swat models snowmelt hydrology in a northwestern minnesota watershed. *Transactions of the ASAE*, 48(4):1359–1376.

Wible, T. (2014). *Enhanced watershed modeling and data analysis with a fully coupled hydrologic model and cloud-based flow analysis*. PhD thesis, Colorado State University.

Willmott, C. J., Ackleson, S. G., Davis, R. E., Feddema, J. J., Klink, K. M., Legates, D. R., O'donnell, J., and Rowe, C. M. (1985). Statistics for the evaluation and comparison of models. *Journal of Geophysical Research: Oceans*, 90(C5):8995–9005.

Wilson, R. (2012). Water-shortage crisis escalating in the tigris-euphrates basin. *Strategic Analysis Paper Date 28 August 2012*.

Wood, A. W., Leung, L. R., Sridhar, V., and Lettenmaier, D. (2004). Hydrologic implications of dynamical and statistical approaches to downscaling climate model outputs. *Climatic change*, 62(1):189–216.

Wood, A. W., Maurer, E. P., Kumar, A., and Lettenmaier, D. P. (2002). Long-range experimental hydrologic forecasting for the eastern united states. *Journal of Geophysical Research: Atmospheres*, 107(D20).

Xie, P. and Arkin, P. A. (1997). Global precipitation: A 17-year monthly analysis based on gauge observations, satellite estimates, and numerical model outputs. *Bulletin of the American Meteorological Society*, 78(11):2539–2558.

Xie, P., Chen, M., Yang, S., Yatagai, A., Hayasaka, T., Fukushima, Y., and Liu, C. (2007). A gauge-based analysis of daily precipitation over east asia. *Journal of Hydrometeorology*, 8(3):607–626.

Xue, X., Hong, Y., Limaye, A. S., Gourley, J. J., Huffman, G. J., Khan, S. I., Dorji, C., and Chen, S. (2013). Statistical and hydrological evaluation of trmm-based multi-satellite precipitation analysis over the wangchu basin of bhutan: Are the latest satellite precipitation products 3b42v7 ready for use in ungauged basins? *Journal of Hydrology*, 499:91–99.

Yang, D., Shi, X., and Marsh, P. (2015). Variability and extreme of mackenzie river daily discharge during 1973–2011. *Quaternary International*, 380:159–168.

Yang, J., Reichert, P., and Abbaspour, K. C. (2007a). Bayesian uncertainty analysis in distributed hydrologic modeling: A case study in the thur river basin (switzerland). *Water resources research*, 43(10).

Yang, J., Reichert, P., Abbaspour, K. C., and Yang, H. (2007b). Hydrological modelling of the chaohe basin in china: Statistical model formulation and bayesian inference. *Journal of Hydrology*, 340(3):167–182.

Yatagai, A., Kamiguchi, K., Arakawa, O., Hamada, A., Yasutomi, N., and Kitoh, A. (2012). Aphrodite: Constructing a long-term daily gridded precipitation dataset for asia based on a dense network of rain gauges. *Bulletin of the American Meteorological Society*, 93(9):1401–1415.

Yue, S., Pilon, P., Phinney, B., and Cavadias, G. (2002). The influence of autocorrelation on the ability to detect trend in hydrological series. *Hydrological processes*, 16(9):1807–1829.

Zhu, Q., Xuan, W., Liu, L., and Xu, Y.-P. (2016). Evaluation and hydrological application of precipitation estimates derived from persiann-cdr, trmm 3b42v7, and ncep-cfsr over humid regions in china. *Hydrological Processes*, 30(17):3061–3083.